Delft University of Technology (TU Delft)

Graduation Project (SET3901)

Electrical Engineering, Mathematics and Computer Science Faculty

Master of Science (MSc) Sustainable Energy Technology (SET)

Segmented Gurney Flaps for Enhanced Wind Turbine Wake Recovery:

Design, Field tests and Simulations

Author	Student number
N.S. (Nirav Subhash) Dangi	5450616

Thesis committee member	Affiliation	Thesis role
Prof. Dr. S.J. (Simon) Watson	TU Delft	Chair
Dr. Ir. Paco López-Dekker	TU Delft	Committee member
Dr. Ir. W.A.A.M. (Wim) Bierbooms	TU Delft	Supervisor
Dr. Ir. W. (Wei) Yu	TU Delft	Supervisor
Dr. Ir. K. (Koen) Boorsma	TNO	Supervisor
Ir. E.T.G. (Edwin) Bot	TNO	Supervisor

Project duration: November, 2022 to May, 2023

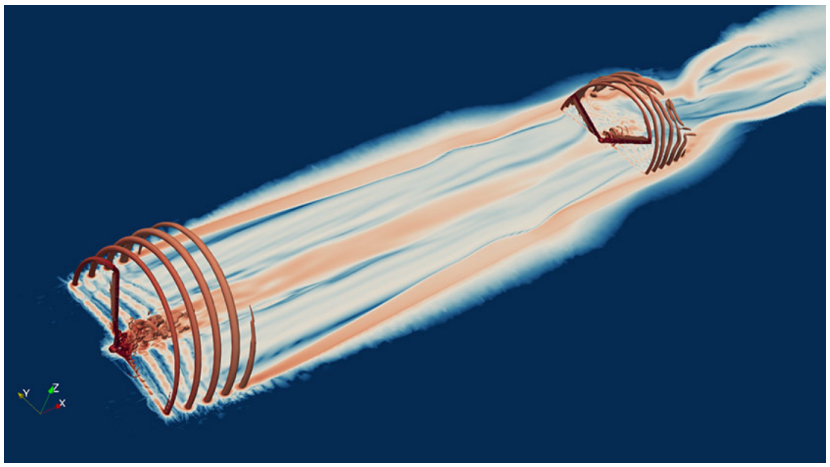

Visualization of the tip-vortex structure and turbine wake interaction flow field in uniform inflow [1]

TU Delft Delft University of Technology

TNO innovation for life

To my Supervisors, Family and Friends

Delft University of Technology
Delft, Netherlands, May 2023
Nirav Subhash Dangi

Abstract

The wind turbine wake is a downstream region of kinetic energy and velocity deficit, higher turbulence and has a complex helical vortex structure. The wind turbine wake's stability depends mainly on the ambient turbulence and the wind turbine tip speed ratio. Researchers have developed several wake control techniques to mitigate this issue, such as static axial induction control by torque or pitch control, dynamic axial induction control by pitch control and actuating flaps or other actively controlled add- on devices. Some gaps are present in these methods, in terms of applicability of these techniques in terms of full scale validation and practicality to have the devices as add on to existing blades.

To address these research gaps, this study focuses on designing and evaluating segmented Gurney flaps (in line with the ECN (now TNO Wind Energy) patent [2] by Edwin Bot and Arne Van Garrel) for wind turbine blades to enhance the wake recovery by inducing turbulence in the wake to excite the tip vortices. 4 Gurney flaps were attached in the tip region of each blade of a GE 3.8 MW research wind turbine. Field tests were conducted in this study for the wind turbine wake (using a scanning LiDAR to scan a sector up to $5.5D$ downstream at different altitudes; with a scan time of ≈ 3 minutes) and performance analysis (using 10 minute averaged measurement data). Free vortex wake simulations were conducted to validate the faster wake breakdown by the change in lift distribution upon addition of segmented Gurney flaps. Simulations using dynamic blade element momentum theory with $IEC - NTM$ inflow conditions from cut in to cut out wind speed were conducted to assess the structural impacts on the retrofitted wind turbine.

The field tests' wake analysis was quantified with different wind speed, turbulence intensity, wind shear, wind direction conditions. Post processing of LiDAR data involved filtering, creating bin averaged data set, using Gaussian process regression and retrieve the required wind component. The results show a consistent increase in wake recovery, generally at all downstream distances. The retrofitted configuration results are associated with a higher standard error because of a shorter testing period (due to increased noise levels) than the baseline configuration. The wake simulations indicate a earlier wake break down position, by $\approx 2D$.

The simulations indicate AEP increase for the retrofitted wind turbine to be roughly +0.2% (+50 MWh), at the expense of increased blade and tower structural loads. The wind speed weighted damage equivalent blade flapwise bending moment was found to increase by +2% to +4%; with peaks observed in partial load region of the wind turbine, associated with the operating angle of attack in this region.

The work conducted in this thesis features the following:

1. Dangi N.S., Boorsma K., Bot E.T.G., Bierbooms W.A.A.M., Yu W. (2023). "Design and Evaluation of Gurney Flaps as Turbulators for Wind Turbine Blades." Presentation at Wind Energy Science Conference (WESC). 23-26 May. Glasgow, United Kingdom.

2. Dangi N.S., Boorsma K., Bot E.T.G., Bierbooms W.A.A.M., Yu W. (2023). "Segmented Gurney Flaps for Enhanced Wind Turbine Wake Recovery." Wind Energy Science (WES). *Manuscript to be submitted for publication.*

Contents

Nomenclature

Abbreviations

AEP	Annual energy production
AL	Actuator line
AR	Aspect ratio
BEM	Blade element momentum
CFD	Computational fluid dynamics
CFL	Courant–Friedrichs–Lewy
ECN	Energy research Centre of the Netherlands
FAST	Fatigue, Aerodynamics, Stress, and Turbulence
FBM	Flapwise bending moment
FOAM	Field Operation And Manipulation
FT	Field tests
FVW	Free- vortex wake
GFRP	Glass fiber reinforced plastic/ polymers
GPR	Gaussian process regression
HAWT	Horizontal axis wind turbine
IEC	International Electrotechnical Commission
LCOE	Levelised cost of energy
LE	Leading edge
LES	Large eddy simulation
LiDAR	Light Detection and Ranging or Laser imaging, detection, and ranging
LLT	Lifting line technique
LoS	Line of sight
LSE	Least square error
MAP	Maximum A Posteriori
MPPT	Maximum power point tracking
NEU	Neutral
NTM	Normal turbulence model
OLAF	cOnvecting LAgrangian Filament

RI	Richardson number	
SOWFA	Simulator fOr Wind Farm Applications	
STAB	Stable	
TE	Trailing edge	
TI	Turbulence intensity	
TIADE	Turbine Improvements for Additional Energy	
TNO	Netherlands Organisation for Applied Scientific Research	
UNS	Unstable	
VSTAB	Very stable	
VUNS	Very unstable	
WD	Wind direction	
WGF	With Gurney flaps	
WOGF	Without Gurney flaps	
WS	Wind speed	

Dimensionless

a	Axial induction factor	[−]
C	Courant number	[−]
c_d	Drag coefficient	[−]
η	Efficiency	[−]
$r_{gearbox}$	Gearbox ratio	[−]
c_l	Lift coefficient	[−]
r_m	Mixing ratio	[−]
C_p	Power coefficient	[−]
Re	Reynolds number	[−]
St	Strouhal number	[−]
λ	Tip speed ratio	[−]
C_t	Torque coefficient	[−]
κ	Von- Kármán constant	[−]
m	Wöhler exponent	[−]

Symbols

ρ	Air density	kg/m^3
c	Airfoil chord	m
z	Altitude	m
α, ψ, θ, γ	Angle	deg (°)
CNR	Carrier to Noise ratio	dB
Γ	Circulation	m^2/s

D	Drag	N
P_{el}	Electrical power	W
U_∞ , V_∞	Free-stream wind velocity	m/s
f	Frequency	Hz
u_*	Friction velocity	m/s
R_g	Gas constant	$Jmol^{-1}K^{-1}$
I	Inertia	m^4
ν	Kinematic viscocity	m^2/s
L	Lift	N
f_ϵ	Loading as body force	N/m
L_{M-O}	Monin- Obukhov length	m
θ	Potential temperature	K
P	Power	W
p	Pressure	Pa
V_r	Radial velocity	m/s
R	Radius	m
RH	Relative humidity	%
Ω	Rotational speed	rad/s
c_p	Specific heat capacity	$Jkg^{-1}K^{-1}$
SH	Specific humidity	%
K	Stiffness	Nm^2
σ_{stress}	Stress	N/m^2
z_0	Surface roughness	m
t	Time	s
T	Torque	Nm
θ_v	Virtual potential temperature	K
ω	Vorticity	$1/s$
λ_{wave}	Wavelength	m
ζ	Wake age	s
U_r	Wind velocity at wind turbine rotor	m/s
u, v, w	Wind components	m/s
E	Young's modulus	N/m^2

List of Figures

List of Tables

Chapter 1

Introduction

The wake of a wind turbine is a region of three-dimensional turbulent flow characterized by a deficit of kinetic energy and velocity and a complex helical vortex structure. The wake of a single rotor blade consists of a continuous sheet of trailed vorticity due to the gradient in bound circulation along the blade span, which rolls up, generating two concentrated vortices at the tip and the root region. The wind turbine wake's stability depends mainly on the ambient turbulence and the wind turbine tip speed ratio. With low ambient turbulence and low tip speed ratio (rated and above rated wind speed conditions) the wind turbine wake is extremely stable. The wind turbine wake leads to the decreased energy production of the downstream turbines. These effects are much more critical on bigger wind farms, where multiple turbines are grouped together and their different wake effects are combined. It can even be 20% for a farm of 140 turbines with a spacing of 5 rotor diameters. It is known that wake alleviation can be achieved by introducing spatial and temporal variation to the stable tip vortex.

This thesis evaluates segmented Gurney flaps for achieving the spatial and temporal variation to the tip vortex; for enhanced wake recovery to achieve higher power output in a wind farm setting. The hypothesis behind the approach is in line with the concept of turbulators, introduced in ECN (now TNO Wind Energy) patent [2]. The hypothesis behind the use of segmented Gurney flaps is to alter the lift distribution along the blade span (at tip); achieve a jagged lift and circulation distribution which causes additional stronger vortices shed from the edges of Gurney flaps to perturb the stable tip vortex. This use of segmented Gurney flaps is hypothesised to cause a spatial disturbance to the tip vortex. Additionally, a temporal variation is hypothesised to be achieved from the inherent rotation of the wind turbine blade which alters the inflow conditions during the rotation as the large rotor is exposed to the wind speed and turbulence shear. Apart from these two effects, a higher drag from the Gurney flap is hypothesised to potentially increase turbulence in the wake which could contribute to the faster wake mixing. This thesis aims to realise the following objectives:

1. Setting up and conducting Scanning LiDAR measurements in the wake (up to a distance of 5.5 times the rotor diameter downstream) for a 3.8 MW research wind turbine with and without these segmented Gurney flaps. The segmented Gurney flaps (4 on each blade) are retrofitted to the 3.8 MW research wind turbine.

2. Analysing wake recovery of both configurations; quantified with different wind speed, turbulence intensity, wind shear, wind direction conditions, that is, varied atmospheric stability conditions.

3. Analysing aerodynamic and structural performance of retrofitted wind turbine in comparison to baseline wind turbine, by use of 10-minute statistical measurement data.

4. Performing simulations to formulate guidelines for implementing Gurney flaps on wind turbine blade and correspond them to field test results.

The work conducted in this thesis is part of the TIADE (Turbine Improvements for Additional Energy). A consortium of TNO (Netherlands Organisation for Applied Scientific Research), GE Renewable Energy and LM Wind Power are collaborating on the TIADE project to develop technologies and design methods for more efficient operation of next-generation wind turbine rotors, wind farms with large rotor wakes and demonstrate them in the field. TIADE has been co-financed with Topsector Energiesubsidie from the Dutch Ministry of Economic Affairs under grant no. TEHE119018.

Structure: Chapter 2 provides background information on wind turbine wakes. Chapter 3 discuses current wind turbine wake control strategies with their advantages and disadvantages. A literature specific to Gurney flaps and their potential towards enhanced wake recovery is provided as well. In Chapter 4 the theory behind the simulation approach considered and used in this study is explained. Following that, the set up and methodology utilised for the field tests and data processing is explained in Chapter 5. The set up and validation of simulations is provided in Chapter 6. The field tests' results and analysis are provided in Chapter 7 and the simulations' result and analysis are provided in Chapter 8. Finally, conclusions and recommendations are provided in Chapter 9.

Chapter 2

Wind Turbine Wakes

Contents

A wind turbine is a device for generating electricity by extracting kinetic energy from the wind. By removing some of its kinetic energy, the wind must slow down, but only that mass of air that passes through the rotor disc is affected [3]. This effect follows from the fact that energy can neither be created nor destroyed. This downstream region is called the wind turbine wake. A simple visualization of the energy-extracting stream tube of a Horizontal axis wind turbine is shown in Figure 2.1 below:

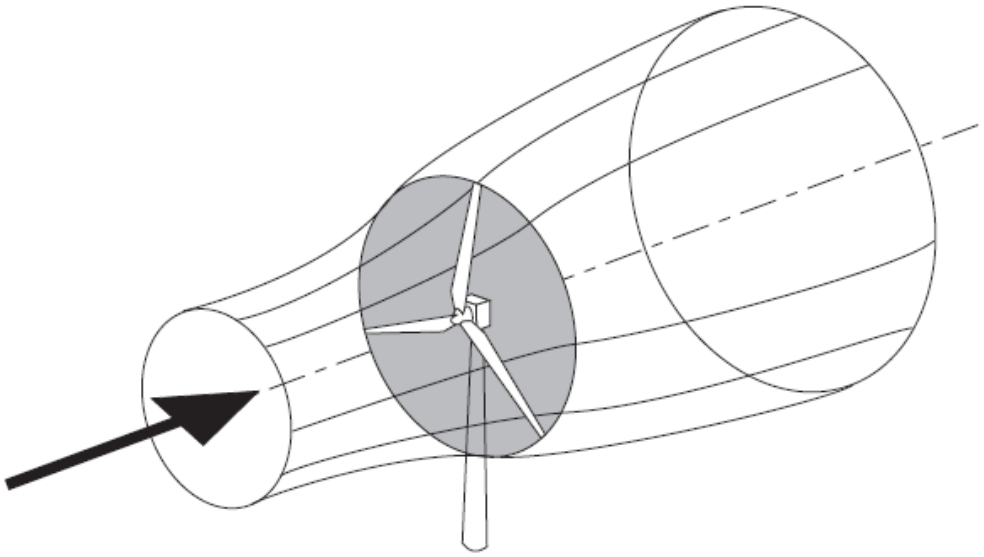

Figure 2.1: The Energy Extracting Stream-tube of a Horizontal Axis Wind Turbine [3]

Figure 2.1 shows an expanding stream tube. As stated, there is a drop in wind speed in the downstream region, which causes the expansion of the stream-tube because the mass flow rate must be the same everywhere. For in-depth knowledge about the working principle of wind turbines, the reader is referred to [3, 4]. This thesis focuses on the Horizontal axis wind turbine (HAWT), and from now on, it is referred to as wind turbine, in the report.

2.1 Background

The wake of a wind turbine is a downstream region of three-dimensional turbulent flow characterized by a deficit of kinetic energy and velocity, a higher turbulence level, and a complex helical vortex structure. The wake of a single rotor blade consists of a continuous sheet of trailed vorticity due to the gradient in bound circulation along the blade span, which rolls up, generating two concentrated vortices at the tip and the root region. The force field at the rotor accelerates the flow imposing a rotary motion to the wake, which is counter-rotating with the rotor. The vorticity created at the blade boundary layer is also released into the wake, in a portion of the flow that co-rotates with the blade due to viscosity. A visual representation of a wind farm in different wake conditions is shown in Figure 2.2 below.

(a) Full-wake conditions seen in the photo taken from Horns Rev wind farm (Courtesy: Vattenfall. Photographer is Christian Steiness)

(b) Partial-wake conditions seen in the photo taken from Horns Rev 2 wind farm (figure taken from [5])

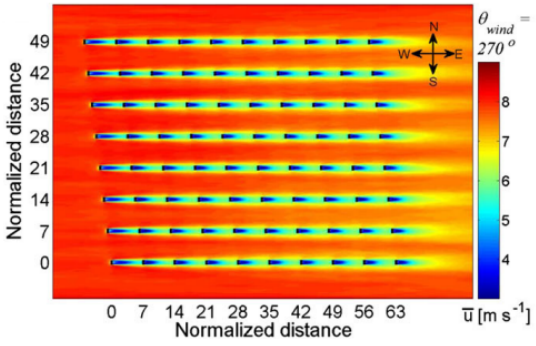

(c) Contour plot of the simulated time-averaged stream-wise velocity component at Horns Rev wind farm on a horizontal plane at hub level for incoming wind directions of 270° (full-wake conditions) (figure taken from [6]) (Distances are normalized by the turbine rotor diameter d = 80 m)

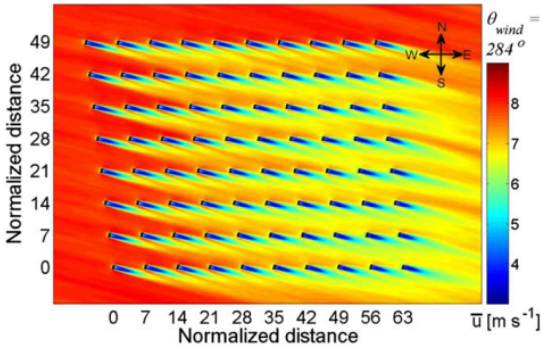

(d) Contour plot of the simulated time-averaged stream-wise velocity component at Horns Rev wind farm on a horizontal plane at hub level for incoming wind directions of 284° (partial-wake conditions) (figure taken from [6]) (Distances are normalized by the turbine rotor diameter d = 80 m)

Figure 2.2: Illustration of wind turbine wakes (Real and Simulated) ([5, 6, 7])

In Figure 2.2a and Figure 2.2b, the turbulent flow in the downstream region is visualised. In Figure 2.2c and Figure 2.2d, the wind velocity deficit is seen from the color bars, which show the reduced velocity in the regions downstream of a wind turbine.

2.2 Wind turbine Wake Breakdown

This section provides a more in-depth overview of a single wind turbine wake. Firstly, a general overview of the wind turbine wake breakdown process is provided. With that overview, the phenomenon present in a wind turbine wake is explained. Secondly, visualisations are provided which show the wind turbine wake breakdown at different conditions of free-stream wind speed. The stability of tip vortices, in particular, at above rated wind speeds (up to cut out wind speed) is seen from these visualisations.

2.2.1 General Overview

In the wind turbine wake, a division can be made into the regions of near wake, intermediate wake, and far wake [8, 9].

The near wake is taken as the area just behind the rotor, where the properties of the wind turbine rotor can be discriminated, so approximately up to one rotor diameter downstream [8]. Here, the presence of the wind turbine rotor is apparent by the number of blades, blade aerodynamics, including stalled flow, 3-D effects, and the tip and root-vortex helices, which are trailed at the two extremities

of each blade, and can show unstable behavior. The tip-vortex filaments define a helical structure due to the combination of the rotational motion of the blade, the free-stream wind flow, and the velocity field induced by the vortex system itself.

The far wake is the region beyond the near wake, where the focus is put on the influence of wind turbines in wind farm situations, so modelling the actual wind turbine geometry is less important. In the far-wake region, the influence of the blade flow is no longer visible: this is the region where the wake-generated turbulence and the external atmospheric turbulence have contributed to the breakdown and diffusion of the tip-vortex spiral and most of the turbulence mixing happens, while the wake undergoes a re-energising process.

Between these two regions, a third zone can be distinguished, the intermediate wake [9]. This is the region where the turbulent mixing begins to prevail on the organized vortical structures, where the tip-vortex spirals may start to interact mutually and become unstable. These regions are illustrated in Figure 2.3.

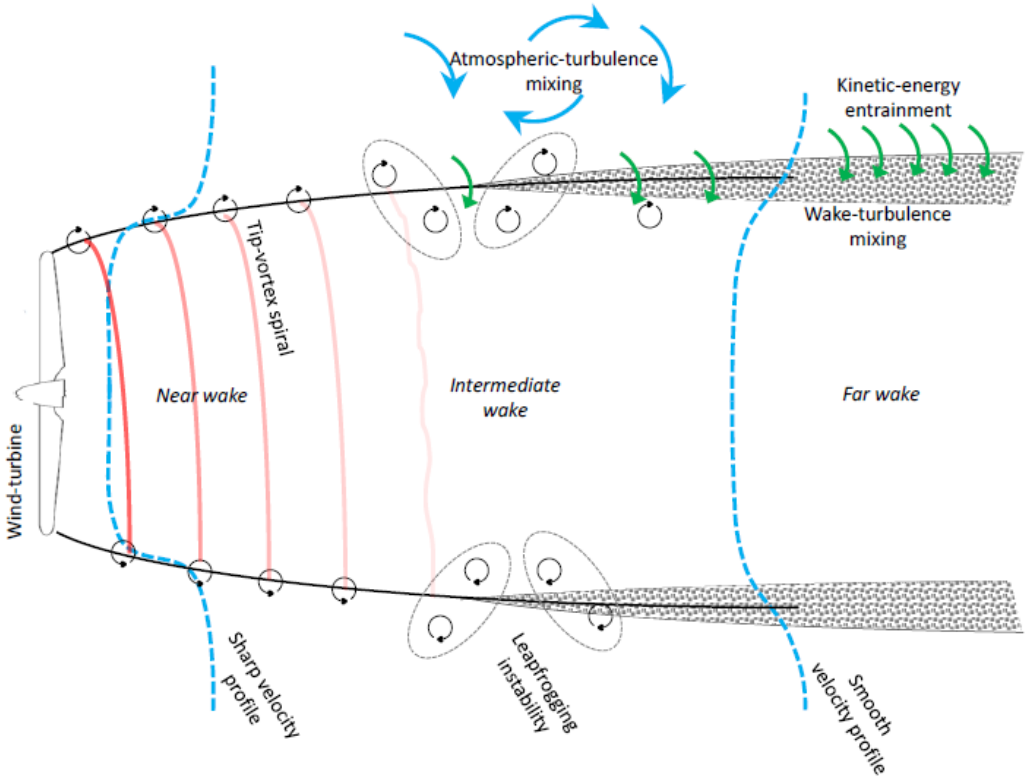

Figure 2.3: Schematic of a wind-turbine wake with tip-vortex leapfrogging instability [9]

With Figure 2.3 the process of wind turbine wake breakdown is visualized. The instability and breakdown of the helical system of vortices in the near wake affects the development of the turbulence in the far wake, where the mixing process between the inner and the outer flow regions occurs [9]. Several authors have investigated the stability properties of the wake's system of vortex filaments [10, 11, 12, 13]. The most evident forms of wake instability are the so-called leapfrogging and meandering. The latter is an unsteady behavior of the wake, in which the whole wake is seen to oscillate randomly with a low-frequency motion ([14, 15]). The former consists of a pairwise interaction among two or more consecutive tip-vortex filaments, which engage in a roll-up process around each other until their coherence is disrupted and they break down into small-scale turbulent fluctuations.

The role of atmospheric turbulence in ensuring a fast breakdown of the tip vortices to ensure a quicker wind turbine wake recovery is worth noting (Also refer [13]). The atmospheric turbulence is very low in offshore wind farms [16, 17], in comparison to onshore wind farms. This states the importance of using techniques that can induce turbulence in the wind turbine wake, especially in

offshore wind farms.

With the wind turbine wake breakdown process discussed, Figure 2.4 below shows the vertical profiles of velocity (normalised with free-stream velocity) in the wind turbine wake. These profiles are generated by use of 4 different high-fidelity simulation codes, by the authors of [18].

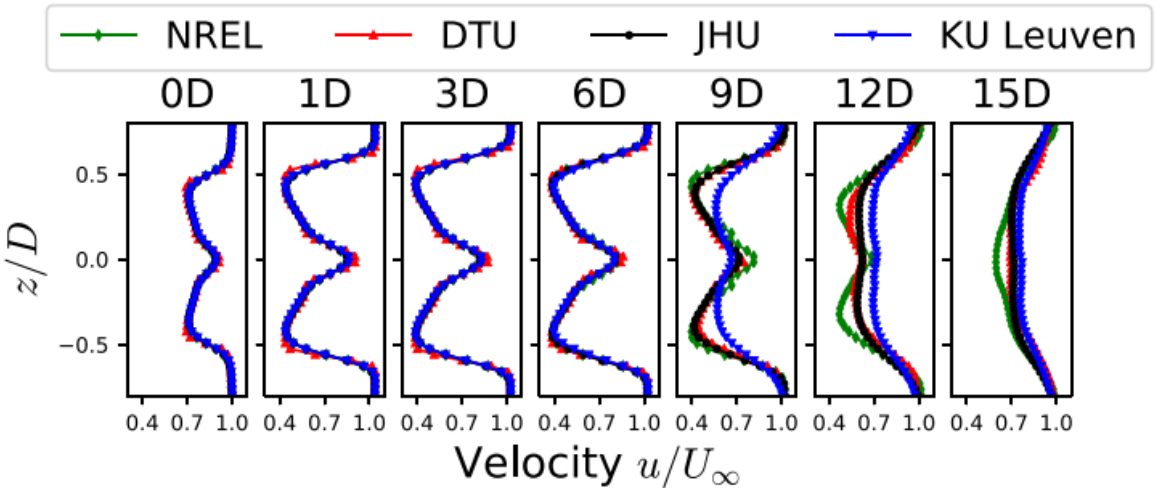

Figure 2.4: Vertical profiles of stream-wise mean velocity (normalised by free-stream velocity) at different downstream distances [18]

In Figure 2.4, the top x-axis represents the downstream position (normalised by wind turbine rotor diameter) and the y-axis represents the altitude (normalised by the wind turbine rotor diameter). The velocity profiles seen in Figure 2.4 are for the NREL 5MW reference wind turbine [19]. It is evident that in further downstream distances the wind turbine wake recovers more and more, that is, the velocity in the wake start to reach the free-stream velocity. It is worth noting that even at the downstream distance of 15D, the wind turbine has not fully recovered (also refer [20]), while most of the wind farms incorporate a 5 to 7 rotor diameter distance between two wind turbines [21]. Thus, the need for enhanced wake recovery is clear, to ensure more optimal wind farm performance.

2.2.2 Effect of Tip-speed Ratio

The wind turbine wake breakdown is affected by the tip-speed ratio of the wind turbine (Refer Equation 3.4). As can be seen, the tip-speed ratio is varied by either changing the rotational speed of the wind turbine or having a different free-stream wind speed. A visualisation of the wind turbine wake breakdown for different tip-speed ratios (by means of varying free-stream conditions in high-fidelity simulations) is provided in Figure 2.5, extracted from [13].

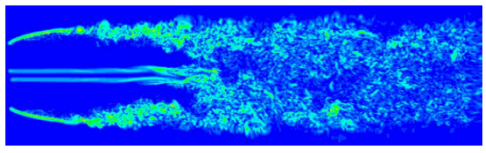

(a) $\lambda = 11.78$ and $U_\infty = 6$

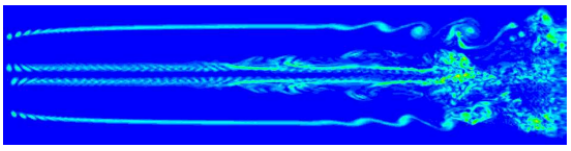

(b) $\lambda = 7.07$ and $U_\infty = 10$

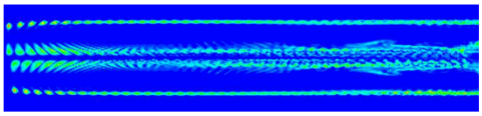

(c) $\lambda = 5.05$ and $U_\infty = 14$

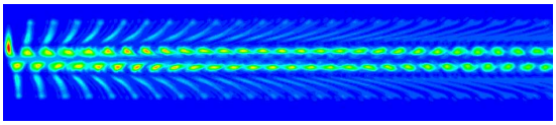

(d) $\lambda = 3.21$ and $U_\infty = 22$

Figure 2.5: Illustration of wind turbine wake by means of vorticity contours (Wind turbine rotor is at left) [13]

Figure 2.5 provides the wake breakdown of the Tjæreborg wind turbine (rotor radius- $30.56m$) which has a optimal tip-speed ratio of 7.07, as is the case in Figure 2.5b. At this tip-speed ratio the tip vortices were observed to undergo a Kelvin–Helmholtz instability approximately 5 rotor diameters downstream. The root vortices became unstable at an earlier point (about 3 rotor diameters downstream) due to their proximity, and further downstream the root and tip vortices interact, which causes the wake to become fully turbulent. In the case of Figure 2.5a it was observed that the bound vorticity was not shed off in individual vortex tubes, as in the other 3 cases. At the lower tip-speed ratios in the case of Figure 2.5c and Figure 2.5d, the instability of tip vortices was not apparent, due to the generally higher stability of the tip vortices, when the tip-speed ratio and thus also the thrust is low.

Now, a three-dimensional visualisation of the wind turbine wake breakdown (for the wind turbine and different tip-speed ratios, as in Figure 2.5) is provided in Figure 2.6, extracted from [13].

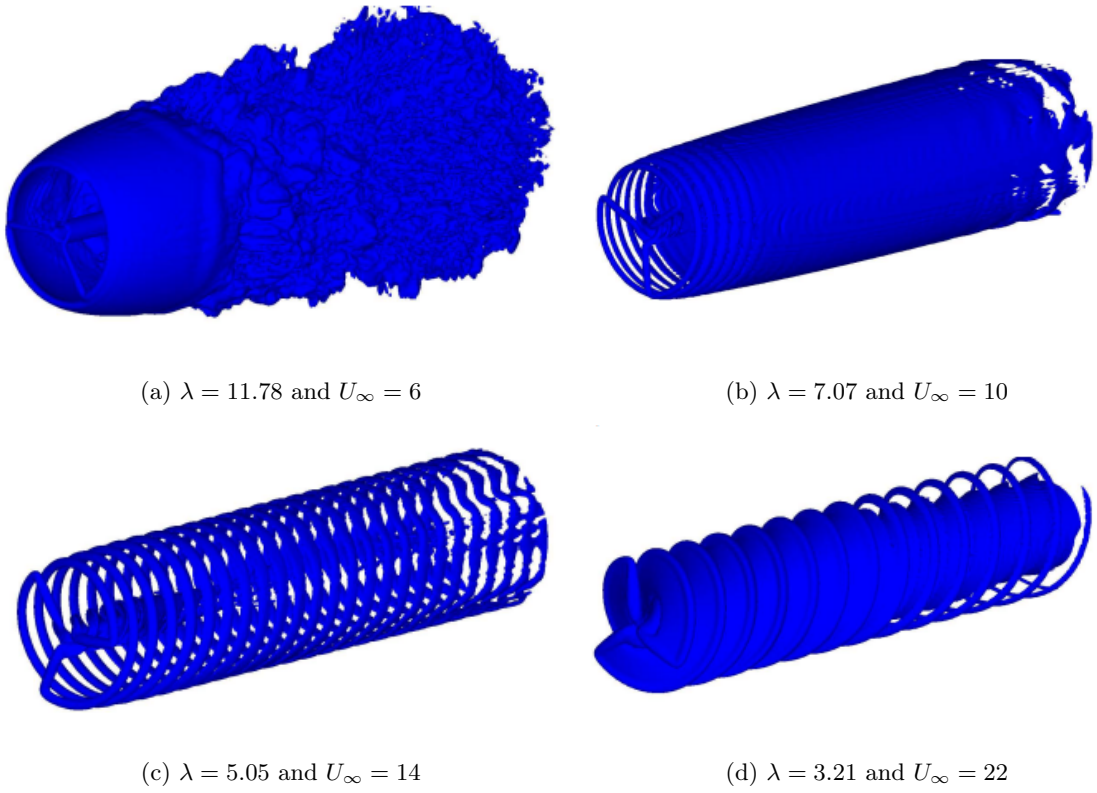

(a) $\lambda = 11.78$ and $U_\infty = 6$

(b) $\lambda = 7.07$ and $U_\infty = 10$

(c) $\lambda = 5.05$ and $U_\infty = 14$

(d) $\lambda = 3.21$ and $U_\infty = 22$

Figure 2.6: Illustration of wind turbine wake by means of iso-surface plots of vorticity [13]

From Figure 2.6 it becomes evident that, at the lowest tip-speed ratio (Figure 2.6d) the wind turbine wake has a clear and stable screw surface geometry. For the cases as in Figure 2.6b and Figure 2.6c, a good impression of the helical structure of the distance tip vortices is made. Lastly, at the highest tip-speed ratio (Figure 2.6a), the complete breakdown of tip vortices into small scale turbulence is shown.

In this subsection, a visualisation of the wind turbine wake, specially, the behaviour of tip vortices is shown in the case of same rotational speed but different free-stream wind speed. It is worth noting that the visualisation provided in Figure 2.5 and Figure 2.6 are for uniform inflow conditions and not an atmospheric turbulent inflow. The cases of lower than optimal tip-speed ratios are comparable to the real-life scenario where the wind turbine operates in free-stream conditions of above rated wind speed. This is because, at above rated wind speed (up to cut out wind speed), the wind turbine no longer increases its rotational speed but the blades are pitched in order to cap the power (For in-depth overview of the control regions, the reader is referred to Chapter 8 of [3]). Thus, once again, the importance of inducing turbulence at these conditions in order to stimulate breaking of the stable tip vortices for a quicker wake recovery is clarified.

2.3 Effects of Wind Turbine Wakes

The wind turbine wake, a region affected by lower wind speed and higher turbulence, negatively affects the wind turbine's performance and structural integrity. The wind turbine wake leads to decreased energy production of downstream turbines. These effects are much more critical on bigger wind farms, where multiple turbines are grouped together and their different wake effects are combined. It can even be 20% for a farm of 140 turbines with a spacing of 5 rotor diameters [22]. An increase in the turbulence of the wind potentially increases the dynamic mechanical loading on downwind turbines [23]. Wind turbine wakes introduce more significant wind shear in addition to the higher turbulence intensity, leading to higher mechanical loads. The wind turbine wakes produce added turbulence intensity from $6-8\%$ up to $20-25\%$ [24], with different coherence of turbulence. With these damaging effects on the wind turbine components, wind turbine wakes lead to downstream wind turbines' lifetime reduction, power production reduction, and more frequent maintenance due to the higher structural loading, leading to an increase in the levelized cost of energy (LCOE).

2.4 Summary

In this chapter, background information necessary for understanding the working principle of wind turbines, the wind turbine wake and its break down was discussed. The role of atmospheric turbulence for a quicker wake recovery was clarified. The stability of tip vortices and their interaction was clarified by means of visualisation of vorticity contours and iso-surface, at different uniform inflow conditions in high-fidelity simulations. The extremely stable structure of the tip vortices during low tip speed ratio conditions was discussed as well. The adverse effects of wind turbine wakes, especially in large wind farms, was clarified. With this background information, the objective was to help the reader realise the importance of techniques to mitigate the wind turbine wakes, that is, implement concepts to ensure quicker wake recovery which will be beneficial for downstream wind turbines. The next chapter explains some current techniques for mitigating wind turbine wakes.

Chapter 3

Wind Turbine Wake Control Techniques

Contents

The previous chapter provided an overview of the wind turbine wakes. The adverse effects of wind turbines wakes were mentioned. The reduction of power output in downstream turbines is evident from the wind turbine wakes. Thus, wake management and control techniques are a crucial research topic. The conventional control scheme for a wind farm is known as greedy control and uses maximum power point tracking; in which every wind turbine is independent and agnostic of other wind turbines. Each wind turbine uses inputs from several sensors to determine the wind direction and the wind turbine's current operational state, in particular rotor speed, in a control algorithm that determines the best control to maximize power production unless the operator overrides it [25]. Thus, this approach disregards the effect of one wind turbine on other wind turbines.

Therefore, this type of control will not always lead to an optimal power production of the wind farm because of the wake effects faced by the downstream wind turbines. Researchers have proposed and studied several wake control strategies, to decrease the power loss of downstream wind turbines by steering (deflecting the wind turbine wake away from another downstream turbine) or weakening the upstream wakes (faster wind turbine wake recovery by inducing increased wake mixing or by pitching to lower angles of attack to cause change in thrust coefficient). Some of these techniques which focus on the latter, that is, decreasing the strength of the wind turbine wake, are discussed in the coming sections of this chapter. Some more details on wake control techniques and a review of those can also be found in [25, 26, 27, 28, 29].

3.1 Static Axial Induction Control by Pitch Control

Pitch control is a technique in which the wind turbine blade pitch angle is modified either individually for each blade or collectively for all blades. With this technique, the induction factor of the wind turbine can be varied, which leads to different power and thrust production for the wind turbine. The induction is the change in wind speed caused by the presence of the (rotating) rotor (which may be represented by an actuator disc). The axial induction is the change in wind speed in the direction of the axis of rotation of the rotor, for a horizontal axis wind turbine. When the rotor is aligned with the wind, this is the change of the wind speed in the wind direction; in this simple case of no yaw misalignment, the change in wind speed is actually a reduction in wind speed, because the thrust force causes the wind to slow down . The axial induction factor is the change in wind speed normalised by the undisturbed wind speed. There is also tangential induction, which is the change in wind speed in the direction of rotation of the blade. Here, only the axial induction factor is mentioned because of its importance towards the pitch control technique. The axial induction factor of a wind turbine is formulated as:

$$a = \frac{U_\infty - U_r}{U_\infty} \tag{3.1}$$

Here, U_∞ is the free-stream wind speed and U_r is the wind speed at the wind turbine rotor disc. Upon a simple analysis of a wind turbine represented as an idealised actuator disc [3, 4], a relation between the axial induction factor and the power coefficient (Cp) and thrust coefficient (C_t) of the wind turbine can be obtained as:

$$C_p = 4a(1-a)^2 \tag{3.2}$$

$$C_t = 4a(1-a) \tag{3.3}$$

The change in pitch angle can affect the tip speed ratio of the wind turbine. This change is attributed to the different relative angles of wind created and the corresponding change to the rotational speed of the wind turbine. Some details about the same can be understood from Chapter 3 of [4].This change in tip speed ratio leads to a change in the axial induction factor of the wind turbine. The tip speed ratio of a wind turbine is formulated as:

$$\lambda = \frac{\Omega R}{U_\infty} \tag{3.4}$$

Here, Ω is the rotational speed of the wind turbine rotor and R is the radius of the wind turbine rotor. An example visualisation of the relation between these parameters is shown in Figure 3.1. At the design point, the optimal operation of the wind turbine is ensured. Upon changing the pitch angles and the corresponding changes in the tip speed ratio, induction factor, power coefficient and thrust coefficient the wind turbine will operate at the corresponding non-optimal point.

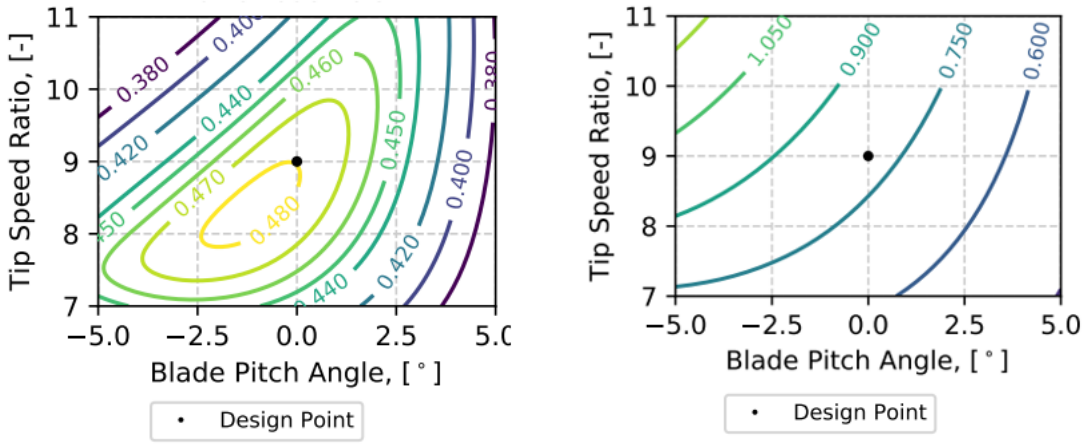

(a) Power coefficient (C_p)

(b) Thrust coefficient (C_t)

Figure 3.1: Example of Steady-state blade element momentum aerodynamic power and thrust coefficient surfaces as a function of wind turbine blade pitch and tip-speed ratio ([30])

Figure 3.1 is an example visualisation of the parameters of the IEA 15MW reference wind turbine [30]. The changing power coefficient and thrust coefficient are evident by the coloured contour lines. As described above, when the turbine operates at the corresponding non-optimal point, the idea of the pitch control technique is to extract less energy from the wind for the upstream wind turbine and thus have more energy (less wind speed deficit) in the upstream wind turbine wake. Then the downstream wind turbine can generate more power, and the idea is to have this higher power more than the loss suffered by the upstream wind turbine.

Researchers have used this concept of using pitch angle to axial induction control to either deflect the upstream wind turbine's wake or to mitigate the wake losses or a combination of both [31, 32, 33, 34]. In [32] , the authors conducted large-eddy simulations of a two-turbine arrangement (in full-wake conditions), consisting of the Vestas 2 MW V80 wind turbine. The study focused on assessing the effectiveness of pitch control technique to mitigate wake loss and also look at how the ambient turbulence intensity affected the results. Results showed enhanced wake recovery associated with pitching to stall (negative pitch offsets), as opposed to pitching to feather (positive pitch offsets), which delayed wake recovery. The increased wake recovery resulted in a noticeable increase ($\approx 2.8\%$) in the power of the two-turbine configuration, only in conditions characterized by low turbulence intensity ($< 4.5\%$) in the incoming flow. The negative pitch offsets resulted in an increased thrust coefficient of the wind turbine, which caused increased shear on the edge of the wind turbine wake. This led to higher turbine-induced turbulence as well as turbulent momentum flux for negative pitch offsets, resulting in faster wake recovery. However, it was seen that the effects of increased turbulent momentum flux and wake recovery due to pitching became insignificant at a higher ambient turbulence intensity of $\approx 6\%$. Consequently, the technique of pitch down-regulation resulted in a decrease in power for the combination compared to the baseline.

3.2 Static Axial Induction Control by Torque Control

Torque control is a technique which in concept is similar to pitch control, that is, to reduce the induction factor of the upstream wind turbine to have more energy available in the wind turbine wake, thus, more power generation potential for the downstream wind turbine.

$$T = \frac{1}{2}\pi\rho R^5 \frac{C_{p,max}}{\lambda^3_{optimal}} \frac{\Omega^2_G \eta_{gearbox}}{r^3_{gearbox}} \tag{3.5}$$

Here, Ω_G is the generator rotational speed, $\eta_{gearbox}$ is the gearbox efficiency and $r_{gearbox}$ is the gearbox ratio. The $\lambda_{optimal}$ is the optimal tip-speed ratio, which leads to the maximum power coefficient $C_{p,max}$. There has been research about mitigating wake loss by using torque control to vary the induction factor of the wind turbine, for example in [35, 36]. In a high fidelity simulation study in [35], the authors conducted a study for the effectiveness of the torque control strategy to mitigate wake losses. The study was conducted on 2 in-line NREL 5MW wind turbines [19]. They found that increasing the torque on the first wind turbine caused the downstream wind turbine to have a higher inflow velocity and power production. However, considering the turbines as a pair, the second turbine's power was not enough to cope with the first turbine's power loss and resulted in a total power production drop. They also conclude that the potential for increased wind farm energy production by this technique of altering axial induction factor is depended on particular atmospheric conditions, wind farm configuration and wind turbine characteristics. In some instances the added kinetic energy in the wind turbine wake is lost to wake meandering and expansion before it reached the downstream wind turbine.

In the experimental study of [36], the authors found that the power production of 2 in-line wind turbines was almost even for tip-speed ratios ranging between 4.5 and 6.5. The torque control strategy was concluded not be an effective strategy. There is not much research into using torque control for a cluster of wind turbines, which could be due to its low potential as evident from current research.

3.3 Dynamic Axial Induction Control by Pitch Control

The techniques discussed in section 3.1 and section 3.2 involve using a static method of axial induction control, that is, to have the induction factor reduced (set) to a pre-determined values. This section explains a dynamic induction control technique, in which the induction control is varied continuously. The main reason for a switch towards this type of technique is that the static induction control leads to minor to non existent power production gains for the wind farm [37].

After being first introduced as a concept, in a patent [38], the concept of dynamic induction control was utilised in a simulation study by [39]. Using large-eddy simulations, the authors investigated optimal control of wind-farm boundary layers, considering the individual wind turbines as flow actuators, whose energy extraction can be dynamically regulated in time so as to optimally influence the flow field and the vertical energy transport. The dynamic wind turbine control optimisation was done by conjugate-gradient optimization method in combination with adjoint large-eddy simulations. Owing to the high computational expense of this control optimisation and also the resulting loads on the wind turbine due to such a dynamic variation, the authors in [37] introduced a novel concept, called Helix approach, using dynamic individual pitch control. This concept was developed by the idea of sinusoidal control signals [40] to reduce computational expense and make the control strategy practical.

The Helix approach is a periodic dynamic induction control technique, with the periodic sinusoidal input signal. Smoother pitch input signals were obtained which reduced the fatigue loads on the wind turbine and almost comparable power gain as to unrestrained control signals. Experiment and aero-elastic simulations were conducted with this method, as described in [41]. The results proved the effectiveness of this approach and the evidence of it out-performing the static induction control techniques. Another study, in [42], used high fidelity simulations; Large eddy simulation [43] using Actuator line modelling [44]. The authors state the power production increase by use of dynamic induction control came at a significant expense of structural fatigue loading on the wind turbine. However, the wind turbines were not full scaled ones, thus, the authors conclude about need of verification of this increase in fatigue loading for full scale wind turbines.

Following this Helix approach, the work in [45], implemented multi-sinusoidal and higher harmonics' signals, rather than the fixed amplitude and frequency sinusoidal signal in the original Helix approach. The work assessed the potential of faster wake recovery using the multi-sinusoidal input signals. Using the free-vortex wake model, the results indicated a considerable earlier breakdown of the tip vortices, thus fast wake recovery. It was found that in comparison to the original control signal

in the Helix approach, the use of multi-sine pitch input signals stimulate earlier wake breakdown by 1.5 times the rotor diameter. However, there were some recommendations towards use of higher fidelity methods in order to tackle the limitations of the free-vortex wake model. The recommendations also include about a detailed load, fatigue analysis to understand the structural impact of the multi-sine signals.

3.4 Add On Devices

The above sections of this chapter explained some wind turbine control orientated techniques to mitigate wind turbine wake loss or to enhance wind turbine wake mixing. This section discusses some concepts to mitigate wind turbine wake loss by means of add on devices to a wind turbine blade or utilise smart rotor concepts for upcoming wind turbine rotor blades.

3.4.1 Gurney Flaps

The Gurney flap is a simple small tab (height usually lower than 2% of the airfoil chord) added to the trailing edge of the high-pressure side of an airfoil. They are oriented perpendicular to the free-stream at the trailing edge of an airfoil or wing which can increase the lift considerably with only a small drag penalty (refer Figure 3.2b). The Gurney flap itself is named after the race car driver Dan Gurney, who, in 1971, discovered the significant gain in down force when applying the device on the rear spoilers. Following that, Liebeck [46] made a widespread introduction of the Gurney flaps. Since then, they have been extensively used on aircrafts and rotor-crafts as a high-lift device.

Apart from Gurney flaps, there are also different types of flaps (refer Figure 3.2a), one of them, a plain flap.

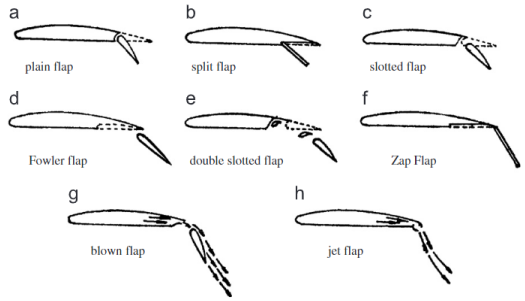

(a) Some types of flaps

(b) Gurney flap

Figure 3.2: A visualisation of the Gurney flaps in comparison to the different types of flaps [47]

There has been research on plain flaps for wind turbines [48, 49, 50], and as a part of smart rotor concepts for upcoming wind turbine rotors [51, 52, 53]. The conclusions from [48] state a considerably earlier breakdown of the excited system, which proves the concept of using plain flaps to excite instabilities in the vortex system. The study in [50] evaluated the potential of load reduction by use of an active flap (plain) system and did find load reduction in the order of magnitude of 3% are feasible for several main components. Although the use of plain flaps in some of these studies is proposed as an add-on to wind turbines, the active flap is made feasible by means of certain pneumatic systems. For also a static plain flap, the implementation on existing wind turbine rotor blades could be challenging. Thus, manufacturing feasibility for the use of plain flaps as static or active devices, could be a bottleneck for the implementation.

With that said, the focus is now shifted to Gurney flaps which can be easier to add-on to existing wind turbine rotor blades, due to their simple configuration. The Gurney flaps do act as a high-lift device but also change the downstream wake development (Refer Figure 3.3), which also depends on the height of the Gurney flap (Figure 3.4).

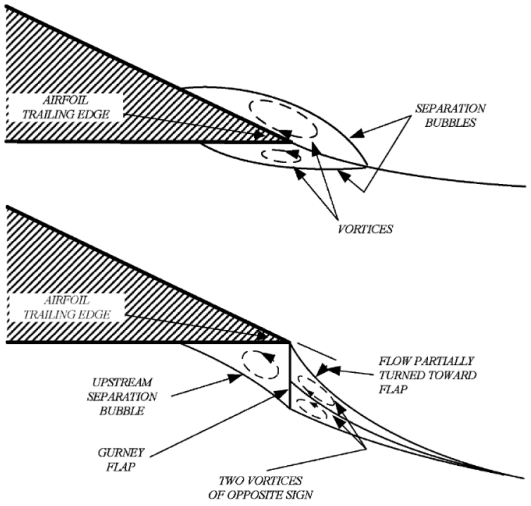

Figure 3.3: Flow patterns without and with the Gurney flap depicted by Liebeck [46]

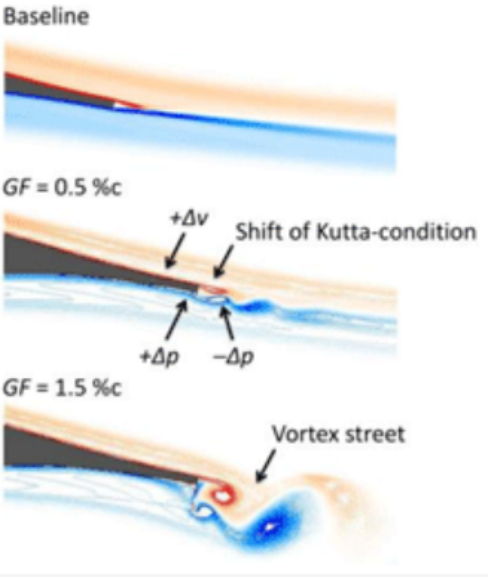

Figure 3.4: CFD simulation of the HQ17 airfoil at $Re = 1x10^6$ at different heights of Gurney flaps [47, 54]

In [55], Gurney flaps were evaluated on different flow regimes on an airfoil. It was found that with the application of Gurney flaps, a long wake downstream of the flap containing a pair of counter-rotating vortices is formed. This can delay or eliminate the flow separation near the trailing edge on the upper surface, increasing the total suction, leading to an increased circulation with an enhanced lift. It was stated that the velocity in the wake is increased by the presence of Gurney flaps. They observed that without the Gurney flaps, the airfoil wake is thin and it does not contain vortices and with a 6% chord Gurney flap, the wake becomes thick and sheds regularly like a Von Kármán vortex street (Refer Figure 3.5) where in the vortex seemed to change its sign and location with time.

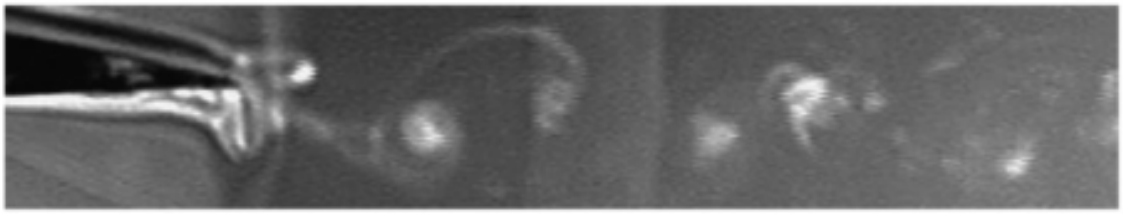

Figure 3.5: Dye visualization of the wake for the 6% chord Gurney flap [55]

The Kármán vortex street can be found in both uniform flow and turbulent flow, explaining the increased lift with Gurney flaps. At the same time, the low-pressure region aft of the trailing edge induces additional drag, especially if vortex shedding is initiated in the form of a Kármán vortex street [47]. Hence, the lift increase is accompanied by a certain drag penalty that affects the lift-to-drag (L/D) ratio accordingly. This discussion provided a background information about the Gurney flap. Since Gurney flaps form a core part of this thesis, the performance and enhanced wake recovery potential upon use of Gurney flaps is explained further below.

3.4.1.1 Aerodynamic and Structural Performance Potential

The performance enhancement of the retrofitted wind turbine with Gurney flaps will be influenced by the change in the airfoil polars (apart from other 3-D boundary layer effects). For the analysis of the potential performance enhancement, a Computational Fluid Dynamics (CFD) study was conducted to generate and analyse the airfoil polars. This CFD study, among other parameters, gave insights mainly towards the changes in the lift coefficient, drag coefficient and the lift to drag ratio parameters. However, due to confidentiality, the analysis of the airfoil on the 3.8 MW research wind turbine

used in this study is not discussed. Instead, a literature study is conducted to illustrate the potential improvements and downgrades of a retro-fitted wind turbine with Gurney flaps. The literature study here is focused by utilising previous research.

The authors of [56] conducted an experimental investigation to analyse the effect of turbulent flow on an airfoil with a Gurney flap. They conducted wind tunnel experiments on DTU-LN221 airfoil under different turbulence intensities. The turbulence levels used for the experiments were 0.2%, 10.5% and 19.0%. The authors also tested different heights and widths of the Gurney flaps, total of 9 configurations, concluding that different widths have limited impact on the performance while height of the Gurney flap plays an important role.

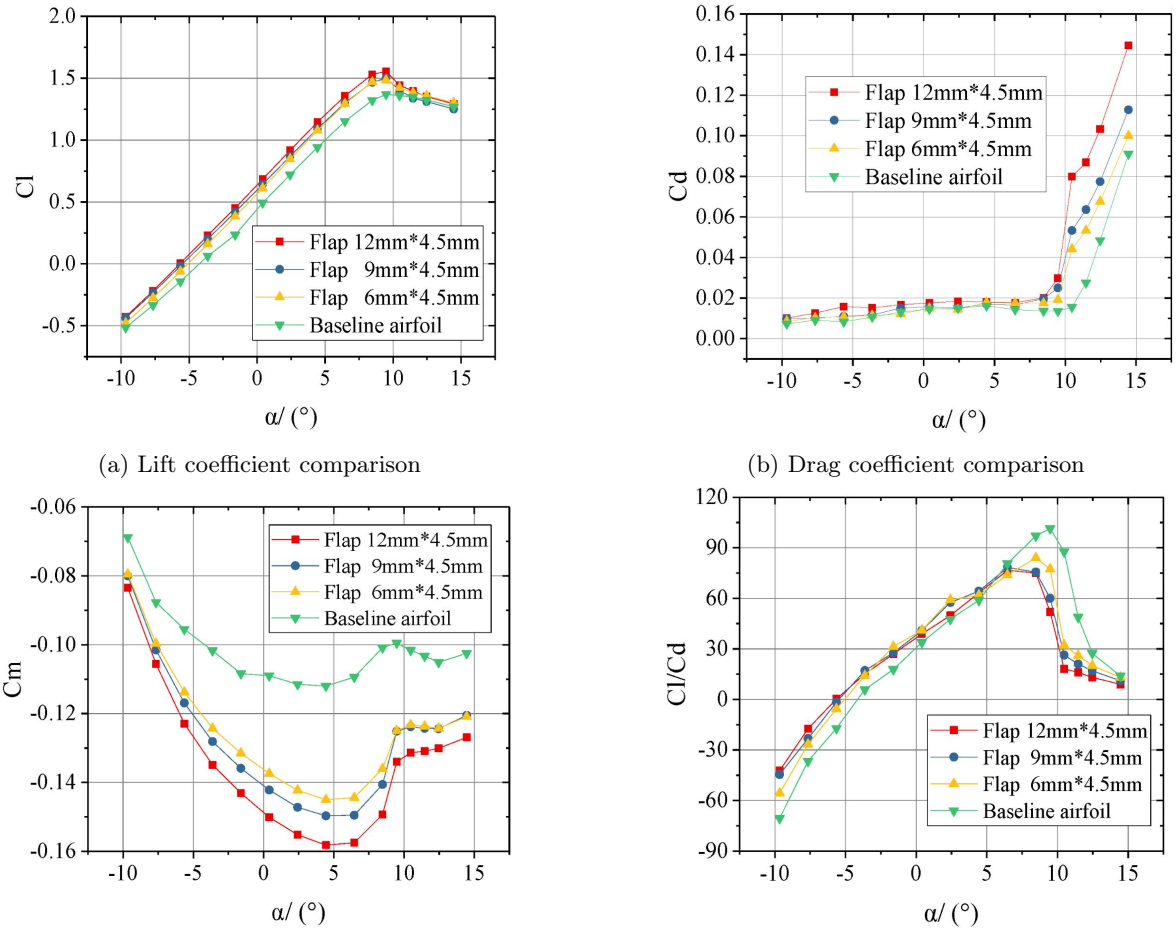

(a) Lift coefficient comparison

(b) Drag coefficient comparison

(c) Pitching moment comparison

(d) Lift coefficient to drag coefficient ratio comparison

Figure 3.6: Performance of different heights of Gurney flaps in uniform inflow conditions [56]

They conducted experiments at a Reynolds number in the range of 0.8 $x10^6$ and angle of attack ranging from $-9.6°$ to $14.4°$, for the low turbulence inflow conditions. The different aerodynamic characteristics of the Gurney flap equipped airfoil and baseline airfoil are shown in Figure 3.6. In the very low turbulence conditions, they found increase in lift coefficient before the stall angle and limited effect above stall angles, as also clear from plenty of existing research. From Figure 3.6a, it was found that when the flap height changes to $6mm$ (1% *chord*), $9mm$ (1.5% *chord*) and $12mm$ (2% *chord*), the maximum lift coefficients were increased by 8.47%, 9.56% and 13.50% at 9.4°, respectively. Looking into the drag coefficients in Figure 3.6b, within the range of $-9.6°$ *to* 10.4°, the drag coefficients show regular change where the frictional drag dominates as expected. The drag coefficients rise rapidly in the stall state, at this time the change in drag coefficient was dominated by pressure drag. When the angle of attack was less than 8.4°, the lift-to-drag ratios, as seen in Figure 3.6d, were all larger than the baseline airfoil. However, the maximum lift-to-drag ratios of the Gurney flap at three heights were smaller than the baseline airfoil. When the flap heights were $6mm$ (1% *chord*), $9mm$ (1.5% *chord*)

and 12mm (2% *chord*), the corresponding maximum lift-to-drag ratios were decreased by 17.16%, 22.79% and 24.47%, respectively.

In the range after the stall angle, the presence of the Gurney flap reduced the lift-to-drag ratios and the higher the flap height, the more the lift efficiency decreases. The authors also conducted a detailed wake analysis which revealed that the Gurney flap deflects the wake position from the pressure side of the airfoil, increasing the vertical distance between the airfoil chord and the middle arc. Before the stall angle, the wake of airfoil with the Gurney flap was inclined to the pressure side of the airfoil. Above stall angle, the Gurney flaps weaken the ability of the wake position deflection; moreover, the wake velocity deficit was significantly increased, and the Gurney flap began to have side effects on the aerodynamic characteristics of the airfoil. They conclude that the higher the Gurney flap is, the larger the wake velocity deficit is, so it indicates a higher mean drag. It is worth noting that only after perturbing the tip vortices that the enhancement towards wake recovery is obtained (will be explained in subsubsection 3.4.1.2). It should also be noted that the effect of Gurney flap will be different on different airfoils, airfoils with different thickness and camber and other characteristics. The changes in lift curve slope can also be evident which was found to be the case for the airfoil polars utilised in this study. These could not be discussed in this study due to confidentiality. However, there is plenty of research on analysis of airfoils with Gurney flaps. To realise these effects, the reader is referred to [57] for a detailed background. In particular page 170, figure 11 and 12 of the same help illustrate the effect of Gurney flaps on lift curve slope.

Continuing on the literature from [56], the authors also report a power density spectrum measured by the region 1cm directly behind the trailing edge under uniform inflow.

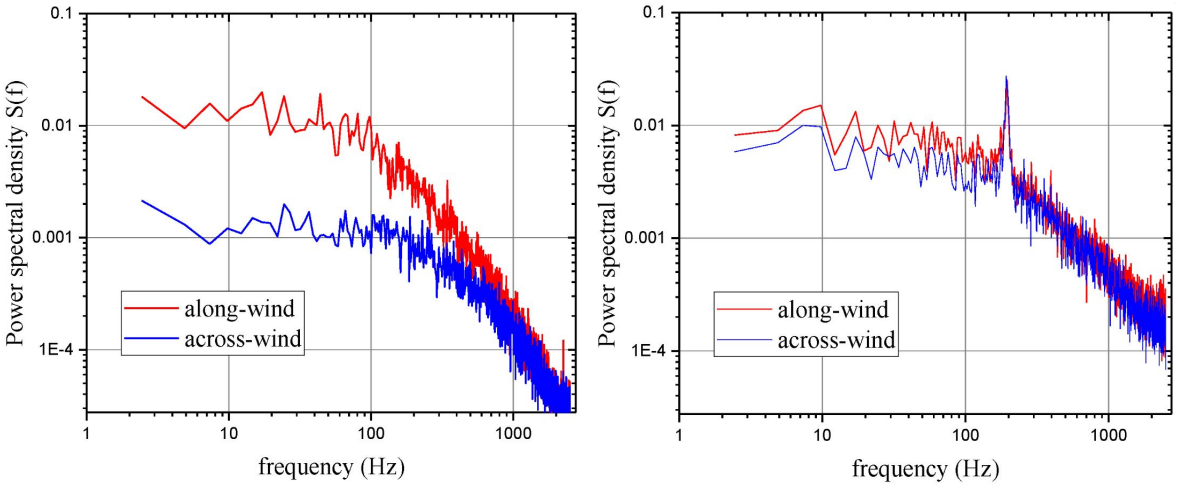

(a) Baseline airfoil (AOA=8.4°)

(b) With 1.5%*chord* Gurney flap

Figure 3.7: Comparison of the power density spectrum without and with Gurney flap in uniform inflow conditions (AOA=8.4°) [56]

From Figure 3.7 it can be observed that both along-wind and across-wind display a clear peak in the power density spectrum, meanwhile the across-wind energy increased in the flapped airfoil. It indicates there are counter rotating vortices generated by the Gurney flap, while the wake of baseline airfoil does not show the existence of vortex shedding. With regards to the particular frequency of the vortex shedding, an estimate can be made by using the Strouhal number.

$$St = \frac{f_{St} \times l_c}{U} \tag{3.6}$$

Represented by Equation 3.6, Strouhal number is a dimensionless parameter describing oscillating flow mechanisms, named after Vincenc Strouhal. f_{St} is the vortex shedding frequency or the Strouhal frequency, l_c is the characteristic length scale, in the case of Gurney flaps, the height of the Gurney flap facing the wind, the characteristic speed of which is represented by U. When the Strouhal number is unknown, one can utilise reference Strouhal number values of different shapes from literature (example, [58, 59, 60]) to get a first estimate of the vortex shedding frequency (f_{St}). For example,

the flap geometry used in [56] is most close to a rectangle, and literature suggests that for a rectangle of height 2 times its length, St is 0.06. Plugging in this value of St, $9mm$ height of Gurney flap and the inflow condition of $20m/s$, as reported in [56], for Figure 3.7b, the f_{St} is found as $133Hz$, off from the observed peak at $\approx 200Hz$. The difference attributed to the reference St not being fully representative of the Flap geometry, as the authors report the St of this case to be 0.088 which when utilised gives the f_{St} as $\approx 200Hz$, as also evident from the PSD in Figure 3.7b.

The Gurney flaps have also been evaluated for wind turbines, in some studies, for example, in [47, 61, 62, 63]. The authors in [47] utilised the Gurney flaps in a wind tunnel experiment, on a wind turbine of $3m$ rotor diameter. The experiment was performed for the cases of a clean geometry and a tripped geometry (to enable laminar-turbulent transition at a fixed point) and Gurney flaps of two different heights. This study focused on using Gurney flaps for load control and increase in power. In [61], the authors conducted wind tunnel experiments and tested Gurney flaps on a three-bladed 4.5 m diameter rotor. The Gurney flaps were tested in two different configurations, up to span-wise location of $60\%R$ and $46\%R$. For the longer configuration it was found that the extra lift from the Gurney flaps adds more power for low tip speed ratios, but this increase was outbalanced by the extra drag for the higher tip speed ratios. The shorter configuration was found to have a power increase for all measured tip speed ratios but the corresponding axial force increased significantly. An aerodynamic performance upgrade provided by Vestas [64] which is a combination of root Gurney flaps and vortex generators leads to an increase in annual energy production by $+0.8 - 1.2\%$.

There appears to be little to no literature on application of flaps (non actuating) or Gurney flaps particularly on the wind turbine blade tip. Thus, the resulting performance analysis (section 8.2) in this study aims to fill this gap in literature along with the field tests conducted (section 7.2).

3.4.1.2 Enhanced Wake Recovery Potential

When utilising Gurney flaps for enhanced wake recovery or wake vortex alleviation, [65, 66, 67, 48, 68, 69] provide detailed study on the topic. The study in [68] investigates the wake of a finite width Gurney flap on a $40kW$ wind turbine, in a wind tunnel. It was found that the flap's tip vortex consists of a stable inner vortex and an outer vortex sheet with adverse vorticity. The outer part interacts with the periodic upwash behind the flap. The authors also conclude that the periodic change in the flap's tip vortex and the crossflow are promising for future experiments to validate the advantage of a better mixing in the far wind turbine wake. They also state that small tip vortices may be advantageous for the dissipation of large wake structure.

In [67] the authors aim to generate a more suitable induced Gurney flap vortex wake by controlling the evolution time of vortex structures, shedding time rate, vortex strength and scales, etc. as an active flow control mechanism to enhanced aerodynamic performance. They conducted experimental studies on the wake at low Reynolds number of an airfoil $HQ - 17$ and a $Clark - Y$, retrofitted with Gurney flaps in different configurations regarding the position and the oscillating movement at different frequencies. They conclude that the effect of the fixed Gurney flap seems to be located in the near field wake whereas the influence of the oscillating flap appears as an increase in downwash in the far field wake.

An effective way of perturbing a wing tip vortex is to alter the shape of the span wise loading distribution (example, Figure 8.1). This is the underlying concept of turbulators introduced in the patent [2]. The specific way in which this is achieved, however, has direct consequences on the perturbation imparted to the vortex. One technique is using miniature trailing edge effectors (segmented Gurney flaps along the span of the lifting surface). The study from [65] uses this concept as the motivation. This study is quite relevant as will become evident in the following overview of the same. Their study was conducted on a $NACA0012$ wing. A visualisation of the same is given below:

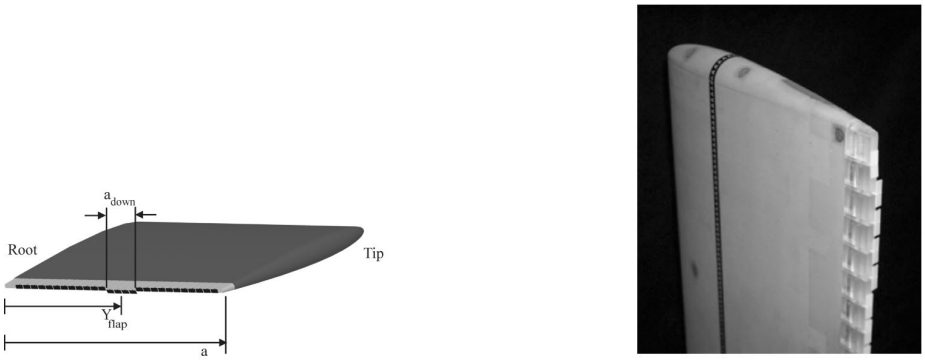

(a) Illustration of the configuration

(b) A rear oblique view

Figure 3.8: The miniature trailing edge effectors (segmented Gurney flaps) configuration used in the study of [65]

As seen in Figure 3.8, a number of segmented Gurney flaps are attached along the trailing edge of the wing. The authors tested various configurations in which the required number of Gurney flaps were actuated down. Apart from other parameters, they examined examine the effect of segmented Gurney flaps on the trailing vortex roll up process. In Figure 3.9, results of one configuration of segmented Gurney flaps tested is shown:

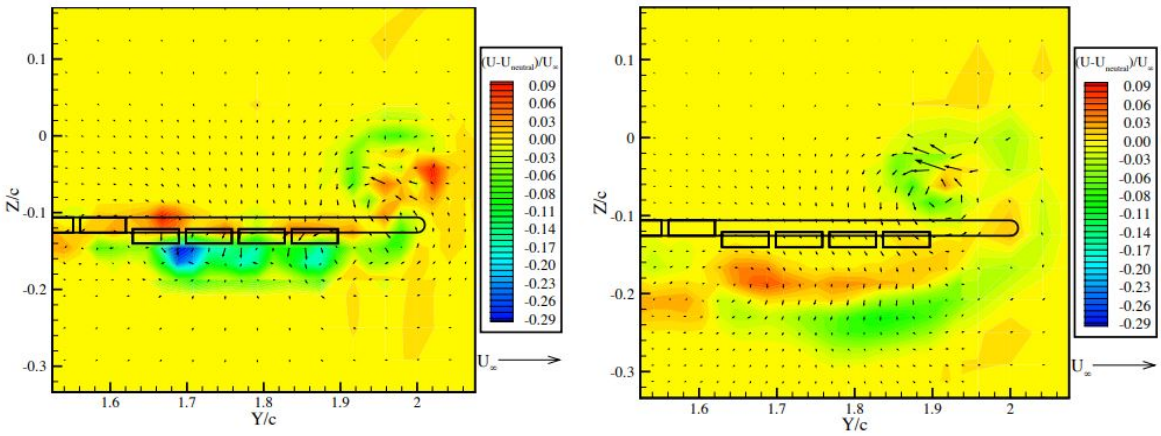

(a) $\frac{X_{downstream}}{chord} = 0.2$

(b) $\frac{X_{downstream}}{chord} = 0.83$

Figure 3.9: Velocity difference field (case of a wing with and without static segmented Gurney flaps) at 2 downstream distances [65] (Segmented black rectangles represent the flaps)

The configuration seen in Figure 3.9 is the closest to the segmented Gurney flap configuration used in this study on wind turbine blades (Figure 5.5 and Figure 5.6b). The expectations of wake recovery by use of segmented Gurney flaps is clearly illustrated. In Figure 3.9 the stream-wise velocity contour is superimposed with tangential velocity vectors. The segmented Gurney flaps caused an intensification of tangential and stream-wise velocity components. The reason behind it being the increase in circulation due to the change in the span-wise loading (example, Figure 8.2). The authors state that despite a smooth increment in the loading distribution in the configuration they experimented, a very small counter-rotating vortex pair also occurred at the flap tips which was then advected by the strong mean flow due to the primary trailing vortex. The velocity deficit around the Gurney flap is associated with the increased drag, however, as seen from Figure 3.9b as we go downstream it is no longer present; because as the vortex continues to roll up, the patches diffuse into one another by being constantly advected by the strong tangential velocities (which was also seen in Figure 3.7b and in the study of [68]). The segmented Gurney flaps' effects were being felt by the vortex more and more as it continued to roll up. From the experiments, the authors established that in order to significantly perturb the vortex, only 13% of the span needed to be deployed with Gurney flaps at any given time. The actuated span was applied only near the tip of the wing where the loading distribution varied the most. The intermediate wake insights from this study also confirmed that the effect of the segmented

Gurney flaps upon the vortex was a lasting and reliable change. They also conclude that miniature trailing edge effectors (segmented Gurney flaps) can be used to introduce spatial disturbances to a trailing vortex in both the span-wise and lift directions. Finally, they suggest about the use of miniature trailing edge effector configurations (segmented Gurney flaps), which if varied in time, may be useful for wake alleviation.

3.4.2 Winglets

Winglets are small extensions at the tip of any kind of lift-generating wing of finite length. Best known from their widespread application in modern aviation, winglets are recognized to reduce induced drag in the tip regions of aircraft wings. This concept was utilised for wind turbine blades in several studies ([70, 71, 72, 73, 74]). Most studies focused on assessing the improvement in power production and the thrust production of the wingletted rotor. The increase in power coefficient was estimated anywhere between 1 and 10% in the different studies.

A particular experimental study of the wind turbine wake, up to four rotor diameters behind a model wind turbine rotor with two different wing tip configurations has been performed in [71]. The objective of this experiment was to investigate how optimized winglets attached to a model wind turbine's blade tips affect the recovery of the wake flow behind it. Highly spatially resolved measurements in cross-flow direction were performed in the wake behind a two-bladed rotor (diameter of $0.9m$) with winglets and the same reference rotor blade with straight-cut tips, to investigate if winglets enhance the breakup of the tip vortices and possibly promote the recovery process of the wake velocity deficit. The downstream-facing winglets created a slightly wider wake compared with a non- wingletted reference rotor, while the mean velocity field otherwise was very similar. For the wingletted configuration, an instability was found in the downstream region $\frac{x}{D} \approx 2$ *and* 3, causing the tip vortices to interact before entirely breaking up around $\frac{x}{D} \approx 3$. In contrast to that, no interaction of the tip vortices behind the straight-cut reference tips was detected before $\frac{x}{D} \approx 3.5$. Considering the application of winglets on multiple rotors in a wind farm setup, the presented results indicate that a higher power extraction in a wingletted rotor's tip region can also positively affect the wake's mean kinetic energy recovery by stimulating a faster tip vortex interaction. Thus, it was concluded that winglets might not only positively affect the power output of a single turbine but also mitigate wake losses. However, the mean stream-wise velocity in the wind turbine wake region up to $\frac{x}{D} = 4$ was found not to be significantly affected by the presence of the winglets.

The concept of winglets was also utilised in the InnoTIP (Innovative rotor blade tips to improve offshore wind farm yield) project [75] (Figure 3.10a). This project was a collaboration project between Energy research Centre of the Netherlands (ECN) and LM Wind Power that aims at reducing the Levelized Cost of Energy (LCoE) of offshore wind by improving turbine yield as a result of an improved blade tip geometry. However, simulation studies analysing the effects of the winglets, did not yield good enough results and it was concluded that winglets are not effective to improve the power production of a wind farm. It was concluded that the production cost will increase when applying the winglets, mainly due to requirements of special production techniques. Due to the design and optimisation of winglet parameters, it was stated that the design cost will increase as well.

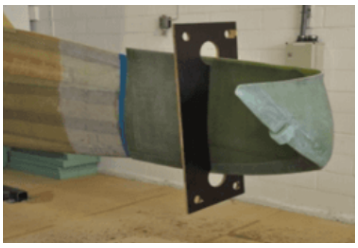

(a) Winglet on wind turbine blade

(b) Turbulators on wind turbine blade

Figure 3.10: A visualisation of the winglets and turbulators (teeth-like triangular shapes) installed on the wind turbine blade in InnoTIP project [75] (Photo courtesy of Skysurvey BV)

3.4.3 Turbulators

In the above-mentioned InnoTIP project, an another type of add-on to the blade tip was also tested, called as turbulators (refer Figure 3.10b). The concept of turbulators was first proposed in the patent [2] with the goal to destabilize the wind turbine blade tip vortex during operation of the rotor blade. Two versions of the turbulators were proposed and one of them was tested by means field experiments on ECN's 2.5 MW test wind turbines at a wind turbine test field in Wieringermeer, Netherlands, apart from computer simulations.

The one version of turbulators served as an add-on device on the existing blade. These were designed as triangular teeth on the tip of the blade. The other version was proposed a wavy shape to be integrated with new blade manufacturing. However, the latter was deemed to be less practical due to likely increase in manufacturing costs and time and the final wind turbine blade weight. The former was fitted on the wind turbines and field experiments were conducted to evaluate the power production of downstream wind turbine as well. An increase in power output of the wind turbine on which the turbulators were fitted, was observed. However, it was concluded that due to lack of data measurements, the effects on the downstream wind turbine were not evaluated and remains a recommendation for a future study. Furthermore, the wind turbine wake measurements were not carried out in this project, and thus the effect of turbulators towards the potential of faster wake recovery was not checked for. The further test and validation of the underlying concept of turbulators in this patent serves as the basis of this thesis. Literature provided in subsubsection 3.4.1.2 (particularly Figure 3.9) about miniature trailing edge effectors (segmented Gurney flaps) tested on aircraft wing in the study [65] also serves as a background information on the potential of the turbulators concept for wind turbine blades.

3.5 Summary

In this chapter, a wide variety of techniques to mitigate wind turbine wake loss were discussed. The wind turbine control oriented techniques of static and dynamic axial induction control by means of either pitch angle or torque output variation were discussed. The techniques relating to smart rotor concepts were explained which included the use of Gurney flaps, winglets and turbulators on the wind turbine blade. The reader was referred to several literature sources to gain further insights on these concepts and also to come across other concepts of mitigating wind turbine wake losses.

However, based on the literature study of the techniques, there were some limitations and disadvantages of these techniques. Firstly, most the studies were recommending field tests to fully validate a particular concept. Secondly, some proven concepts were prone to a inherent disadvantage of increasing the structural and fatigue loading on the wind turbines. Thirdly, there were recommendations to further validate certain simulation studies by higher-fidelity computational methods in order to capture all relevant details of the wind turbine wake. Lastly, there were manufacturing and design optimisation costs linked to certain concepts which did not make the concepts ready for a practical implementation at scale.

The potential of Gurney flaps towards wake control was clear by a variety of studies and its ease in manufacturing, as also evident by how simple its construction is, in comparison to other types of flaps. The aerodynamic and structural performance enhancement potential upon use of Gurney flaps was discussed as well. Based on the existing literature on wake control techniques, the studies did lack full-scale tests and field experiments or high fidelity simulations. To attempt to overcome these limitations, is the motivation of this thesis and the objectives of the thesis were clarified in Chapter 1.

Chapter 4

Background on Wind Turbine Wake Simulations

Contents

In the previous chapter, literature review of existing wake mitigation techniques was discussed. This chapter explains the background of the simulation environment used in this study to investigate the use of segmented Gurney flaps as turbulators for enhanced wind turbine wake recovery. Blade resolved CFD was not in the scope of this study and the wind turbine wake simulations were aimed to validate the hypothesis of faster wake breakdown by addition of segmented Gurney flaps. The simulations for the aerodynamic and structural performance analysis were conducted by the conventional method of dynamic blade element momentum theory (DBEMT). So, a detailed background on DBEMT is not detailed here. DBEMT is NREL OpenFAST ([76]) terminology for using blade element momentum theory in dynamic inflow conditions.

In this study, the original approach was to use the high- fidelity NREL-SOWFA [77]. NREL-SOWFA (Simulator fOr Wind Farm Applications) is a set of CFD solvers, boundary conditions, and turbine models. It is based on the OpenFOAM CFD toolbox [78], coupled with NREL OpenFAST. The main steps in using this approach involved the use of a precursor atmospheric boundary layer simulation which is used to set inflow conditions of the final simulation, which then also involves (in this study) using Large-eddy simulations [43] with actuator line modelling [44] for the wind turbine coupled with NREL OpenFAST. However there were certain limitations regarding computational expense to simulate the effect of segmented Gurney flaps with this approach; discussed in the coming section.

To overcome the limitations, a change in the approach was made and the simulations were performed by using the mid- fidelity NREL OLAF [79], coupled with NREL OpenFAST. cOnvecting LAgrangian Filaments (OLAF) is a free vortex wake (FVW) module. Brief overview on these techniques is given in the coming sections.

4.1 NREL SOWFA

4.1.1 Precursor Atmospheric Boundary Layer

The first step to running the high fidelity simulations was to generate a precursor atmospheric boundary layer. The bottom 0.3 to 3 km of the troposphere is called the atmospheric boundary layer (ABL). It is often turbulent, and varies in thickness in space and time. It is acted upon by the effects of the Earth's surface, which slows the wind due to surface drag, warms the air during daytime and cools it at night, and changes in moisture and pollutant concentration [80]. The precursor(s) are then used as the corresponding boundary condition for the inflow in the different simulation cases.

The atmospheric boundary layer solver is a large eddy simulation solver governed by LES-filtered continuity, momentum and potential temperature equations. The momentum equation consists of the Boussinesq-buoyant forces, the Coriolis force due to planetary rotation, uniform pressure gradient driving the flow, SFS momentum fluxes. The solver employs a wall model for surfaces stresses close to the ground, in accordance with Monin Obukhov- similarity theory. Detailed theory on the solver can be found in literature, for example, in [81, 82, 83]. This approach was chosen as it would allow to replicate the inflow conditions during the Field tests, in a realistic manner.

4.1.2 Actuator Line Modelling

Owing to the high computational expense and practical in-feasibility of blade-resolved CFD, NREL SOWFA makes use of the actuator line technique developed by [44]; where in the wind turbine blade is represented as lines (Figure 4.1). The loading is distributed along these lines which represent the blade forces. The developed algorithm combines a three-dimensional Navier-Stokes solver with this actuator line technique, originally developed in the vorticity-velocity (ω-V) formulation.

Figure 4.1: Representation of the actuator line method for a wind turbine rotor

The following relation was obtained after applying the curl operator on the Navier-Stokes equations in vorticity-velocity variables:

$$\frac{\partial \omega}{\partial t} + \nabla \times (\omega \times V) = -\nu \nabla \times (\nabla \times \omega) + \nabla \times f_\epsilon \tag{4.1}$$

In Equation 4.1 the formulation then is in terms of three transport equations for the vorticity components, three definition equations connecting velocity and vorticity and the continuity equation as shown below:

$$\nabla \times V = \omega \ , \quad \nabla \cdot V = 0 \tag{4.2}$$

Kinematic viscosity is represented by ν and f_ϵ is the loading which is introduced as a body force on the right-hand side of the momentum equations. Now, in terms of the primitive pressure and velocity variables the Navier- Stokes equations and the actuator line concept are combined as:

$$\frac{\partial V}{\partial t} + V \cdot \nabla V = -\frac{1}{\rho} \nabla p + \nu \nabla^2 V + f_\epsilon \tag{4.3}$$

Here again t is time and ρ is the air density and f_ϵ is the loading which is introduced as a body force that is added to the momentum equations, p is the pressure. The body forces are located along the blades, which are represented by actuator lines, as seen in Figure 4.1. The body forces are determined by the blade-element momentum theory ([84]) with two-dimensional airfoil data. The body force is given by Equation 4.10 and the equations that lead to that relation follow as:

$$L = \frac{1}{2} C_l(\alpha) \rho (U_{rel})^2 c dr \tag{4.4}$$

$$D = \frac{1}{2} C_d(\alpha) \rho (U_{rel})^2 c dr \tag{4.5}$$

Here L and D are the lift and drag respectively with c_l and c_d the respective lift and drag coefficients. The visual representation of these forces and other necessary parameters are shown in Figure 4.2 below:

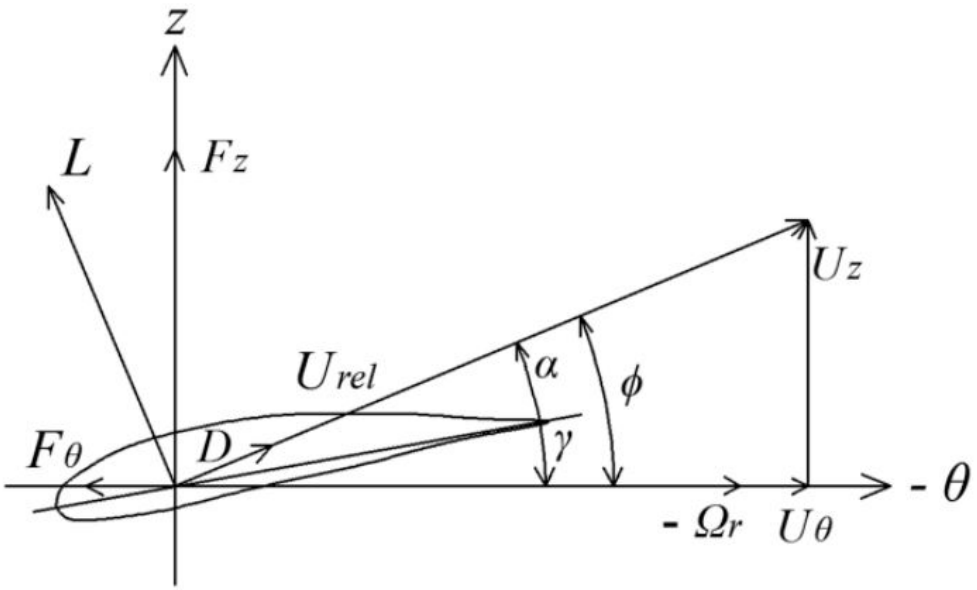

Figure 4.2: Cross-sectional airfoil element [85]

As seen in Figure 4.2, U_{rel} is the local velocity relative to the blade; c is the chord length and dr is the thickness of the blade elements. U_{rel} is calculated as:

$$U_{rel} = \sqrt{(U_z)^2 + (\Omega r - U_\theta)^2} \tag{4.6}$$

In the above equation, U_z and U_θ are the axial and tangential velocity respectively; Ω is the rotating angular velocity and r is the rotating radius. The angle of attack is given by the difference of the angle of inflow and the local pitch angle of the blade:

$$\alpha = \phi - \gamma \tag{4.7}$$

The force per span wise unit length is given by:

$$f = (L, D) = \frac{1}{2}\rho(U_{rel})^2 c(C_l\overline{e_L} + C_d\overline{e_D}) \tag{4.8}$$

In the above equation, e_L and e_D are the unit direction vectors of L and D respectively. As the source term in Equation 4.3 is given by the curl of the load, it acts as a singular vorticity source along the rotor blades. In order to avoid singularity, a constant ϵ is added to adjust the strength of the regularization kernel function, one form shown as:

$$\eta_\epsilon(d) = \frac{1}{\epsilon^3 \pi^{\frac{3}{2}}} \exp(-(\frac{d_i}{\epsilon})^2) \tag{4.9}$$

In the above equation d_i is the distance between the measured point (x_i, y_i, z_i) and the initial force points (x, y, z) on the wind turbine blade. η_ϵ is the kernel function between the measured and initial force points. Finally, the body force f_ϵ on the nearby mesh is calculated by the following relation:

$$f_\epsilon(x, y, z, t) = f \otimes \eta_\epsilon = \sum_{j=1}^{N} f(x_i, y_i, z_i, t) \frac{1}{\epsilon^3 \pi^{\frac{3}{2}}} \exp(-(\frac{d_i}{\epsilon})^2) \tag{4.10}$$

Here, N is the number of neighbouring blade sections and thus smooth interpolation of the discretised force on each blade section is possible on the neighbouring mesh nodes. One limitation of the blade-element theory is in terms of the necessity to correct for the tip loss effect of rotors which plays an important role in the prediction of wind turbine performance. Thus the Prandtl-Glauert tip loss function ([86, 84, 87])is used as:

$$F_{tip} = \frac{2}{\pi} \arccos(\exp(-\frac{B(R-r)}{2r \sin \phi})) \tag{4.11}$$

where B is the number of blades. However, in NREL SOWFA, we are simulating the entire 3-D flow around the blades, so there is not a present need to enable this correction. In this section and the previous section, a basic overview of the high- fidelity simulation environment of NREL SOWFA was provided. The precursor atmospheric boundary layer and its use as an input for inflow conditions for the large-eddy simulations with actuator line theory was explained. The next section explains the limitations faced with actuator line modelling to simulate the effect of segmented Gurney flaps on the wind turbine wake, which made it necessary to change the approach.

4.1.3 Limitations faced

Before mentioning the limitations faced in using actuator line modelling in this study, it should be noted that the limitations explained are not in the scope of general use of actuator line modelling, but for the case of also using it to evaluate the effect of segmented Gurney flaps (as in Figure 5.5) in comparison to the baseline case. Thus, some of the limitations discussed here can be tackled after careful simulation setups, when only simulating the baseline case, while could not be tackled (by use of the current publicly available version of NREL SOWFA) for the retrofitted wind turbine case with segmented Gurney flaps. For detailed insights into requirements of a good simulation setup, the reader is referred to, for example, [88, 89, 90]

In Equation 4.9 and Equation 4.10, the regularization kernel ϵ in Gaussian form is user specified based on a variety of factors, such as, CFD grid cell size, blade chord, sensitivity study by looking at power production with changing ϵ (also see [88, 91]). Depending on the specified ϵ parameter and the CFD grid cell size, the neighbouring cells are effected by the body force of each element. A visualization of the same is given below:

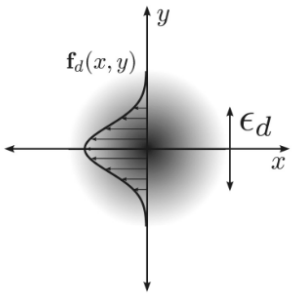

Figure 4.3: Example for 2-D rotational flow over Gaussian lift distribution) [91]

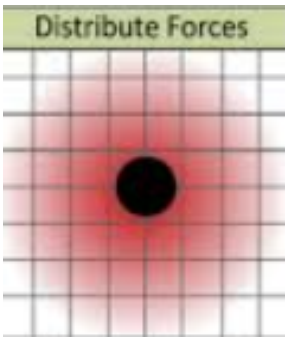

Figure 4.4: Example for body force distribution about an actuator line element [92]

With the visualisation in Figure 4.4, it is emphasized how important the choice of ϵ is when trying to resolve the body force of the Gurney flaps on the wind turbine blade tip, without affecting neighbouring cell with no Gurney flap. In Figure 5.5 the Gurney flap implemented on the wind turbine blade in segments is shown. To preserve confidentiality, not stating the exact dimension of the Gurney flap, an intuitive example is provided here to realise the limitation faced. Let us assume the Gurney flap has length $1m$, and the general rule of thumb stating to use a value of $\frac{\epsilon}{\Delta_{CFD\ cell}} = 2$ ([13]) as a way to avoid numerical instability with very small ϵ values but achieve accurate turbine power predictions. With these assumptions, to resolve the different lift distributions of the segmented Gurney flaps along the blade span would require a CFD cell of size $0.5m$ along the blade span (apart from the further need for gradual refinement in the wind turbine wake and induction zone for proper capture of turbulence), under the current implementation of a constant span- wise ϵ value in NREL SOWFA. If it were possible to implement different ϵ along the blade span, the problem of small CFD cell size could be alleviated and only the tip regions could be refined. However, with the the use of Large- eddy simulations, to ensure the blade tip does not traverse more than 1 cell in a timestep would lead to very small timestamps. For example, if we calculate the required number of time steps per rotation, for a rotor of $70m$ radius:

$$N_{min,per\ rotation} = \frac{2\pi \times R}{\Delta_{CFD\ cell}} = \frac{2\pi \times 70}{0.5} \approx 880\ timesteps\ per\ rotation \tag{4.12}$$

Thus, for a rotor of $70m$ radius and let us assume, $\Omega = 10rpm = \frac{1}{6}rps$, we will need $\Delta t = 6.8\mu s$. Alternatively it can also found using the widely checked CFL (Courant–Friedrichs–Lewy) condition [93], and using the rotor tip speed instead of the inflow wind speed in the below equation:

$$C = \frac{U_{tip} \times \Delta t}{\Delta_{CFD\ cell}} \leq C_{max} \tag{4.13}$$

The CFL condition as represented by the Courant number (C) in the above equation is a condition for the stability of unstable numerical methods. For an explicit time marching solver, the C_{max} as seen in Equation 4.13 is the maximum permissible Courant number, which is 1, while it can be higher for implicit solvers. With this example it is evident that to resolve the body forces accurately for every segmented Gurney flap, there is an inherent requirement of the very small timestep which is further reduced because of the ϵ requirement stated above. Thus, to solve the timestep in the order of micro-seconds for a typical case of operation, for a 10 minute simulation, would require huge computational expense and time which is not practical.

The ϵ parameter also has an important effect on the circulation and thus the shed vorticity (shown in Figure 4.5). With lower and lower ϵ, the circulation can be found to be same as lifting line theory. Because the velocity is sampled at the center of each actuator element, which is the center of the bound vortex circulating about the actuator line, the effects of the upwash and downwash created by the bound vortex are not seen. $\frac{\epsilon}{c} \approx 0.25$ and $\frac{\epsilon}{\Delta_{CFD\ cell}} \approx 4$ lead to accurate prediction of the expected constant downwash [90].

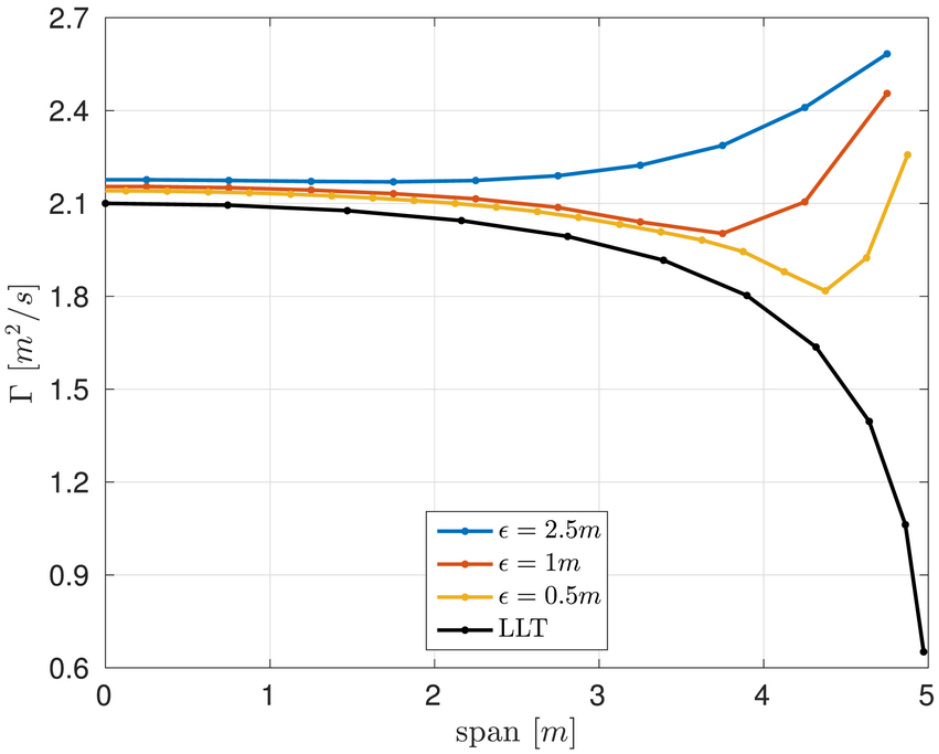

Figure 4.5: Comparison of circulation distributions from lifting line technique (LLT) and actuator line method (ALM) with different ϵ values for $AR = 10$ wing [94]

The changing circulation distribution with ϵ is seen from Figure 4.5, however, trying to reduce ϵ down to optimal value as listed above, would once again bring us back to the problem with very small timestep. There has been research on this topic and attempts to add corrections to the actuator line modelling, for example, in [94, 95, 96, 97, 98]. The effect of ϵ on the shed vorticity is shown below:

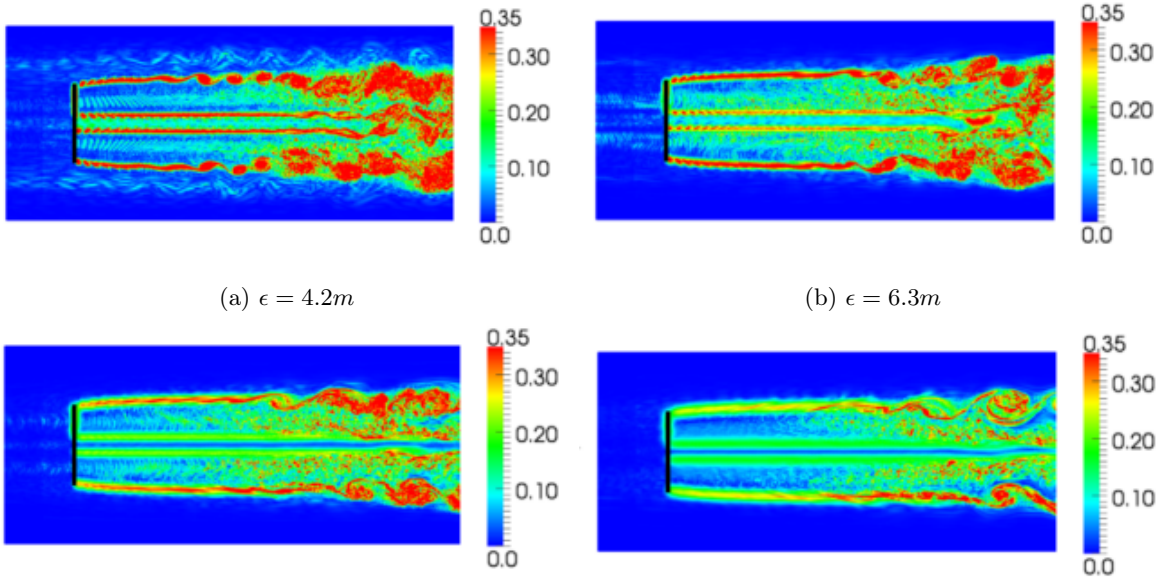

(a) $\epsilon = 4.2m$ (b) $\epsilon = 6.3m$

(c) $\epsilon = 8.4m$ (d) $\epsilon = 10.5m$

Figure 4.6: Illustration of influence of ϵ in ALM on shed vorticity [98]

Figure 4.6 shows that the shed vortices interact differently, specially, away from the rotor. This will have a significant impact on the wake development and thus without the use of an optimal value of ϵ, an accurate comparison of the wake of the wind turbine with and without segmented Gurney flaps cannot be made. The corrections implemented in NREL SOWFA by [98] did manage to significantly reduce the effect of ϵ on the wind turbine power production. However, when analysing the wake, it was concluded that the correction needs further work. Some corrections were found to be already implemented in EllipSys3D, the flow solver developed in co-operation between the Department of Mechanical Engineering at DTU and The Department of Wind Energy at Risø National Laboratory [99]. Particularly a vortex-based tip/smearing correction which has been implemented in the actuator line modelling in EllipSys3D can be seen in [96]. However, EllipSys3D was not considered for this study, for one, as it required licensing unlike the open source NREL SOWFA.

With this discussion, the reasons for a change in approach are established. Mainly, attempting to replicate the effect of segmented Gurney flaps (without going down the path of blade- resolved CFD) with actuator line modelling and the corresponding requirement of a very small time-step, of order micro- seconds has made it necessary to use an alternative method for simulations. The approach of using Free- vortex modelling can deal with the above mentioned circulation and shed vorticity problem because it is built on the lifting line technique. The use of NREL OLAF is made for this study and is explained in the coming sections. The drawbacks of using this approach are also mentioned in line with the explanation, and in section 6.1.

4.2 NREL OLAF

OLAF is incorporated into the NREL OpenFAST module AeroDyn15. For the wake simulations in this study, OLAF is used as the free vortex wake modelling option. For detailed literature towards free vortex wake modelling, the reader is referred to [100, 101]. Some general background on the technique is given here.

The OLAF module uses a lifting-line representation of the blades, which is characterized by a distribution of bound circulation. The spatial and time variation of the bound circulation results in free vorticity being emitted in the wake. The OLAF model is based on a Lagrangian approach, in which the turbine wake is discretized into Lagrangian markers defined in terms of wake age (ζ) and azimuthal position (ψ) (Figure 4.7).

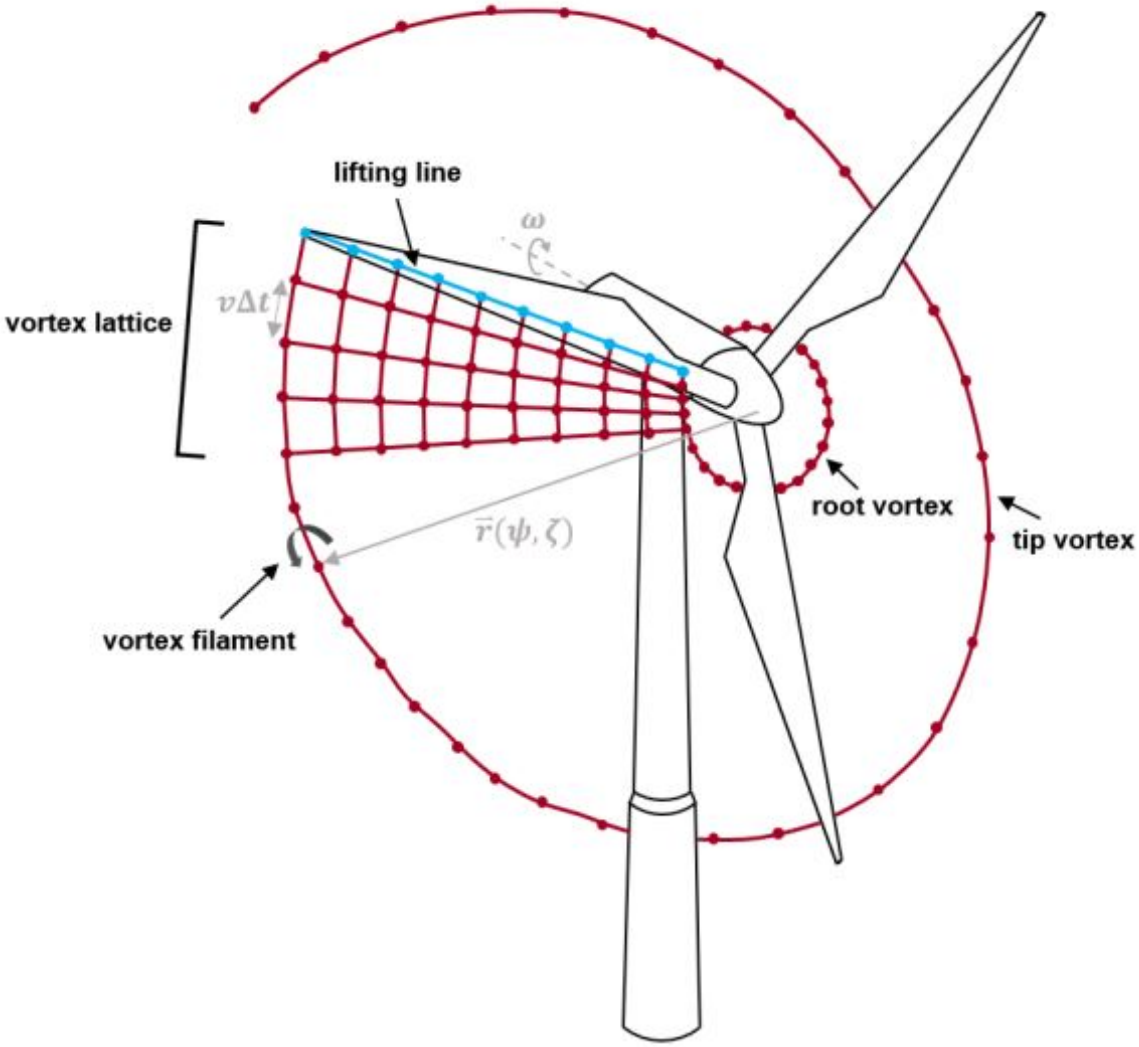

Figure 4.7: NREL OLAF: Evolution of near-wake lattice, blade root and tip vortex, and Lagrangian markers[45]

In OLAF, a hybrid lattice- filament method (Figure 4.7) is used to represent the Lagrangian markers. The near wake region (specified by user) utilises the lattice method and after this region, the wake is assumed to instantly roll up into a tip vortex and a root vortex. Each Lagrangian marker is connected to adjacent markers by straight-line vortex filaments, approximated to second-order accuracy [102]. The wake is discretized based on the span wise location of the blade sections and a specified time step. To limit computational expense, the settings can be set such that the root and tip vortices are truncated after a specified distance downstream from the turbine. The wake truncation violates Helmholtz's first law stating that the strength of a vortex line is constant along its length, and introduces an erroneous boundary condition. To alleviate this, OLAF has an option to set a frozen wake which is a buffer zone, in which the markers convect at the average ambient velocity, and the truncation error is minimized ([103]). The buffer zone is typically chosen as the convected distance over one rotor revolution. However, OLAF does provide an option to only use the near wake which allows for more accuracy, with a compromise on computational expense.

With a brief introduction to OLAF, a few formulations are mentioned in this part. OLAF solves for the turbine wake in a time-accurate manner, which allows the vortices to convect, stretch, and diffuse. The vorticity equation used to describe the evolution of the wake vorticity (for incompressible

homogeneous flows in the absence of non-conservative force) is given by:

$$\frac{d\vec{\omega}}{dt} = \frac{\partial\vec{\omega}}{\partial t} + \underbrace{(\vec{u}\cdot\nabla)}_{\text{convection}}\vec{\omega} = \underbrace{(\vec{\omega}\cdot\nabla)}_{\text{strain}}\vec{u} + \underbrace{\nu\Delta\vec{\omega}}_{\text{diffusion}} \tag{4.14}$$

In the above equation, $\vec{\omega}$ is the vorticity, $\vec{u}$ is the velocity and ν is the viscocity. The projection of vorticity onto a discrete number of filaments and separately treating the convection and diffusion steps can be done by means of different approximations; known as viscous-splitting. The discretization requires a regularization of the vorticity field (or velocity field) to ensure a smooth approximation. The forces exerted by the blades onto the flow are expressed in vorticity formulation as well. This vorticity is bound to the blade and has a circulation associated with the lift force. A lifting-line formulation is used in NREL OLAF to model the bound vorticity:

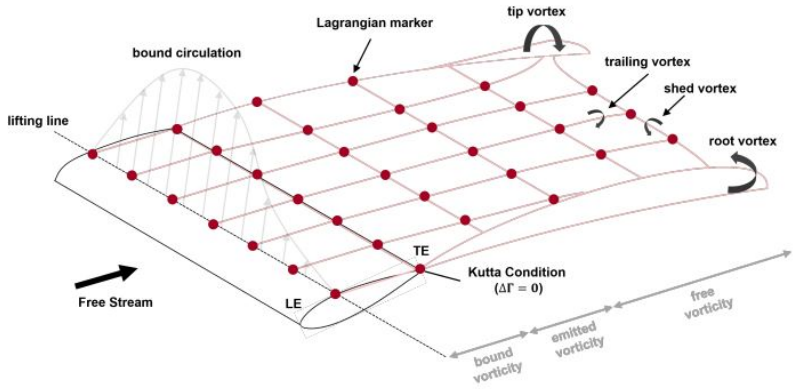

Figure 4.8: Free vortex wake model based on the lifting-line and the vortex- filament representation [45]

The need of smoothing functions is explained later with Equation 4.18 and Figure 4.12. NREL OLAF uses a lifting-line formulation to model the blades. The lifting-line in the current version of NREL OLAF is defined as the $\frac{1}{4}$ chord location from the leading edge. The loads at each cross-section of the blade are lumped onto the mean line of the blade. In the vorticity-based version of the lifting-line method, the blade is represented by a line of varying circulation. The line follows the motion of the blade and is referred to as 'bound' circulation. The bound circulation does not follow the same dynamic equation as the free vorticity of the wake, but is linked to airfoil lift via the Kutta-Joukowski theorem. Spanwise variation of the bound circulation results in vorticity being emitted into the wake, referred to as trailed vorticity. Time changes of the bound circulation emitted in the wake are referred to as 'shed' vorticity. These terms can be visualised in Figure 4.8.

At a given time step, the circulation (Γ) of each lifting-line panel is determined according to one of the three methods: C_l-Based Iterative Method ([101]), No-flow-through Method [104, 105] or User prescribed circulation. With the C_l-Based Iterative Method utilises airfoil polar data at each control point on the lifting line and uses it in a nonlinear iterative solver to determine the circulation. The method makes sure that the lift obtained using the airfoil angle of attack and the airfoil polar data matches the lift obtained with the Kutta-Joukowski theorem. At the end of the time step, the circulation of each lifting-line panel is emitted into the wake, forming free vorticity panels. To satisfy the Kutta condition, the circulation of the first near wake panel and the bound circulation are equivalent, as seen in Figure 4.10:

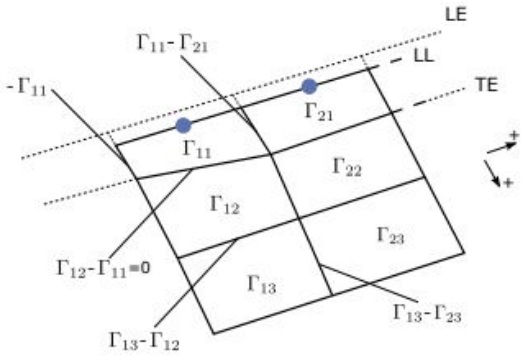

Figure 4.9: Circulation of panels and corresponding circulation for vorticity segments between panels [79]

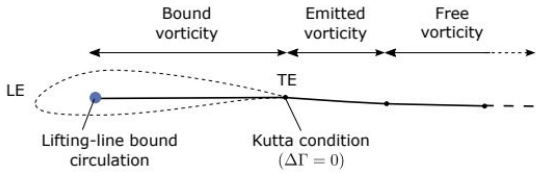

Figure 4.10: Leading-edge, trailing edge, and lifting-line in Wake and lifting line vorticity representation [79]

The wake panels model the thin shear layer resulting from the continuation of the blade boundary layer. This shear layer is modeled using a continuous distribution of vortex doublets (constant strength assumed on each panel), equivalent to a vortex ring of constant circulation. The boundary between two panels corresponds to a vortex segment of intensity equal to the difference of circulation between the two panels. The circulation of the bound panels and the first row of near wake panels are equal, and thus the vortex segments located on the trailing edge have no circulation. The governing equation of motion for a vortex filament given by the convection equation of a Lagrangian marker is formulated as:

$$\frac{d\vec{r}}{dt} = \vec{V}(\vec{r}, t) \tag{4.15}$$

In the above equation, $\vec{r}$ is the Lagrangian marker position. The Lagrangian convection of the filaments stretches the filaments and thus automatically accounts for strain in the vorticity equation. A first-order forward Euler method is used to numerically solve the above equation explicitly. In polar co-ordinates (in terms of the variables shown in Figure 4.7), the equation of motion for a vortex filament is formulated as:

$$\frac{\partial\vec{r}(\psi,\zeta)}{\partial\psi} + \frac{\partial\vec{r}(\psi,\zeta)}{\partial\zeta} = \frac{\vec{V}\left[\vec{r}(\psi,\zeta), t\right]}{\Omega} \tag{4.16}$$

In the above equation, $\frac{d\psi}{dt} = \Omega$, $d\psi = d\zeta$ ([103]), and $\vec{r}(\psi,\zeta)$ is the position vector of a Lagrangian marker. In Equation 4.15 the right hand side velocity term is a nonlinear function of the vortex position representing combined free-stream and induced velocities. Using the Biot- Savart law, the induced velocity is represented by:

$$d\vec{V}(\vec{x}) = \frac{\Gamma}{4\pi}\frac{d\vec{l}\times\vec{r}}{r^3} \tag{4.17}$$

Upon integration of Equation 4.17 filament length (of elementary length $d\vec{l}$) delimited by points $\vec{x}_1$ and $\vec{x}_2$ we get:

$$\vec{V}(\vec{x}) = F_\nu\frac{\Gamma}{4\pi}\frac{(r_1+r_2)}{r_1r_2(r_1r_2+\vec{r_1}\cdot\vec{r_2})}\vec{r_1}\times\vec{r_2} \tag{4.18}$$

The above equation in conjunction with Figure 4.11, contains the terms as $\vec{r_1} = \vec{x} - \vec{x_1}$ and $\vec{r_2} = \vec{x} - \vec{x_2}$. The smoothing function is a part of the Equation 4.18 as the regularization parameter F_ν. To avoid the numerical instability because of the singularity issue as evident in Equation 4.17, the use of a regularisation parameter is made to obtain numerical method to converge to Navier- Stokes solutions. The regularization is used to improve the regularity of the discrete vorticity field, as compared to the 'true' continuous vorticity field, for a physical vortex filament, viscous effects prevent the singularity from occurring and diffuse the vortex strength with time. The circular zone where the velocity drops to zero around the vortex is referred to as the vortex core.

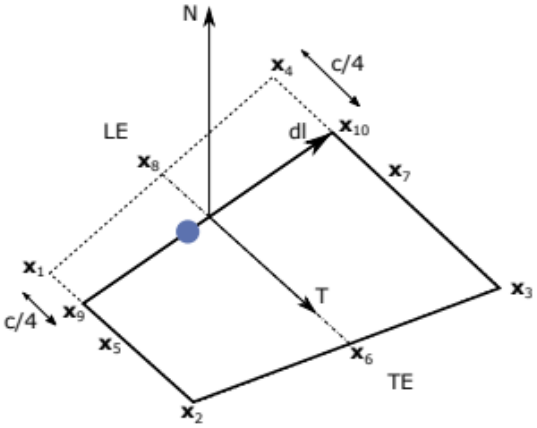

Figure 4.11: NREL OLAF: Geometrical quantities for a lifting-line panel [79]

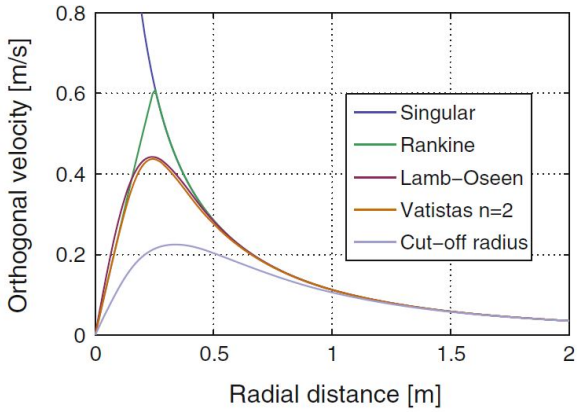

Figure 4.12: Vortex segment velocity for different F_ν [100]

In NREL OLAF, the choice of regularisation function is among Rankine method, Lamb-Oseen method, Vatistas method, denominator offset method or no correction. The time evolution of the regularization parameter may be chosen as a constant value, stretching, wake age or stretching and wake age. With the Vatistas method [106], the regularisation function is formulated as:

$$F_\nu = \frac{(\frac{\rho}{r_c})^2}{\left(1 + (\frac{\rho}{r_c})^{2n}\right)^{\frac{1}{n}}} \; here \; \rho = \frac{|\overrightarrow{r_1} \times \overrightarrow{r_2}|}{r_0} \tag{4.19}$$

A visual representation of the different functions can be seen in Figure 4.12. The Vatistas method with $n = 2$ in the above equation is a good approximation to the analytical Lamb- Oseen vortex. The algebraic formulation of the Vatistas method allows for a faster computation compared to the exponential form of the Lamb- Oseen vortex. The term r_c represents the viscous core radius, which can be chosen to evolve with time. With the wake age method, the viscous core radius is used as:

$$r_c(\zeta) = \sqrt{(r_{c0})^2 + 4 \times 1.25643 \times \delta \times \nu \times \zeta} \tag{4.20}$$

In the above equation, the second term accounts for the viscous effects as the wake propagates downstream. The term δ represents a user- specified viscous diffusion parameter and depends on the inflow conditions. Relation between δ and vortex Reynolds number can be found in [107], which also summarises other research on this topic. The time evolution of the viscous core radius is formulated as:

$$\frac{dr_c}{dt} = \frac{2 \times 1.25643 \times \delta \times \nu}{r_c(t)} \; with \; \frac{dr_c}{dt} = 0 \; on \; the \; blades \tag{4.21}$$

In this chapter, the limitations because of the low time step requirement when using actuator line modelling for segmented Gurney flaps were clarified. A change of approach to using free vortex wake modelling for wind turbine wake simulations was discussed. Background information on the technique was provided. With this chapter, the literature review chapters of this thesis are concluded. The coming chapters of this report discuss the setup, data processing and results of the field tests and simulations conducted in this study.

Chapter 5

Field Tests

Contents

The field tests in this thesis were conducted for assessing the wind-turbine wake and performance of a 3.8 MW research wind turbine with and without segmented Gurney flaps. The field tests were conducted at a wind farm in Wieringermeer, The Netherlands. The field tests involve two components, wind turbine wake analysis and, aerodynamic and structural performance analysis of retrofitted wind turbine in comparison to baseline configuration. The wake analysis implies the assessment of the effect of segmented Gurney flaps on wind turbine wake recovery; and the performance analysis, implies the assessment of the wind turbine power and load measurements. For the wind turbine under study, the undisturbed wind sector ranges from wind directions from ≈ 180 deg (South) to ≈ 340 deg (North-Northwest), measured with North as 0 deg.

The wakes in the sector of 190 deg (South by West) to 250 deg (West-Southwest) were utilised for this study, this aligns with the choice of Scanning LiDAR set up to ensure a fast scan time along with capture of wake up to $4D$ to $5D$ downstream at various altitudes. For the wind turbine performance analysis, the entire undisturbed wind sector was used. The representation of the sectors is shown in Figure 5.7. This chapter explains the set up and data processing of the field tests conducted in this thesis. Firstly, an overview of the measurement site and the instruments is given. The retrofitting of the wind turbine with segmented Gurney flaps is discussed as well. Secondly, the data processing of the field tests' data is explained. Then, the data binning is explained, following which, an atmospheric stability analysis of the site is discussed.

5.1 Measurement Site and Instruments

The field instruments of a ground based profiling LiDAR, scanning LiDAR, and a met mast were used for the data analysis. The inflow conditions were measured by a ground based profiling LiDAR, which was placed upstream ($\approx 2.2D$ or $\approx 282m$) of the 3.8 MW research wind turbine of $130m$ rotor diameter and $110m$ hub height. This profiling LiDAR was used to assess the inflow conditions at 11 different altitudes between $42m$ and $188m$. The Scanning LiDAR was used to get a three-dimensional visualisation of the wind turbine wake. The met mast was used for atmospheric stability calculations, explained in section 5.4. The Leosphere Vaisala Windcube 200S scanning LiDAR was used in this study. Throughout the measurement campaign, the operating settings were tweaked in order to focus on different types of visualisation. This was done by changing the Scanning LiDAR azimuth, elevation and range settings (Refer Figure 5.8 to see the co-ordinate system). The Scanning LiDAR was placed at a distance of $\approx 912m$ from the wind turbine.

Figure 5.1: TIADE GE 3.8MW research wind turbine [108]

Figure 5.2: Leosphere Vaisala Windcube 200S Scanning LiDAR placed in the TIADE test site in Wieringermeer, The Netherlands

In Figure 5.1 and Figure 5.2 the wind turbine utilised in this study is shown and the Scanning LiDAR in use is shown. The satellite view of the test site and the exact geographic positioning of the wind turbine is not shown here with regards to confidentiality.

With the measurement site and instruments discussed, the retrofitting of the above mentioned wind turbine is explained. The retrofitting was done by addition of 4 segmented Gurney flaps on each blade tip. The Gurney flaps were designed as a simple add-on to the existing wind turbine blade. As discussed in subsection 3.4.1, the height of the Gurney flap is usually 2% of the airfoil chord. Thus, upon literature study the Gurney flaps installed on the wind turbine blade were designed to have height of 2% of the chord. Figure 5.3 below illustrates the height and placement of the Gurney flap with respect to chord. Figure 5.4 provides the shape of the Gurney flap in 3-Dimensions (Exact dimensions are not provided to preserve confidentiality about the wind turbine blade dimensions).

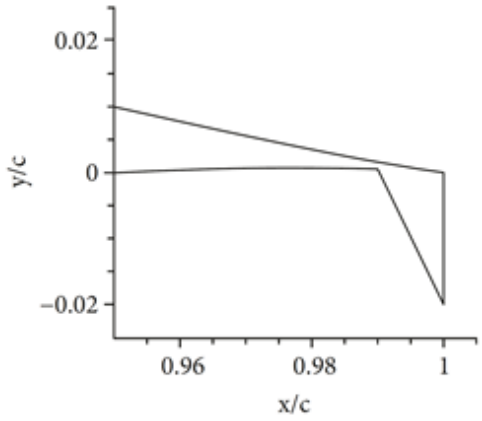

Figure 5.3: Gurney flap extending from wind turbine blade trailing edge

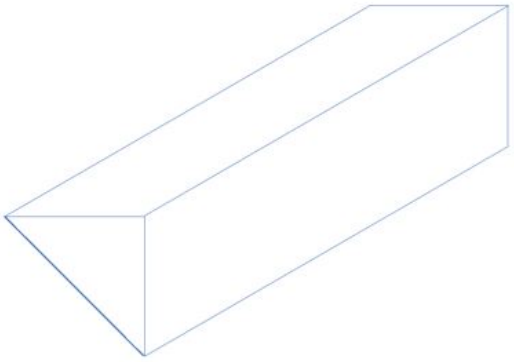

Figure 5.4: Gurney flap design

The Gurney flaps were manufactured with SikaBlock M940, which has a density of $1200 kg/m^3$. Some more details about the material can be found in [109]. The resultant weight came to a maximum of $130g$ for one Gurney flap. Following on literature (subsubsection 3.4.1.2) and turbulators concept (subsection 3.4.3), 4 Gurney flaps were designed and manufactured for each of the 3 wind turbine blades, in line with the hypothesis for causing a spatial variation to the tip vortex. So, a total of 12 Gurney flaps for the wind turbine rotor. The visualisation of the spacing between each Gurney flap on the wind turbine blade is shown in Figure 5.5 below:

Figure 5.5: Gurney flaps (Blue thick line) shown on wind turbine blade (only a part of the blade is shown)

In Figure 5.5, the spacing between the Gurney flaps is clarified. The exact height of each Gurney flap is not mentioned as per confidentiality on the wind turbine blade chord. The manufactured Gurney flaps were installed to the wind turbine blade by use of Plexus MA 320. Some insights to the installation phase are provided below:

(a) Cherry picker and the wind turbine

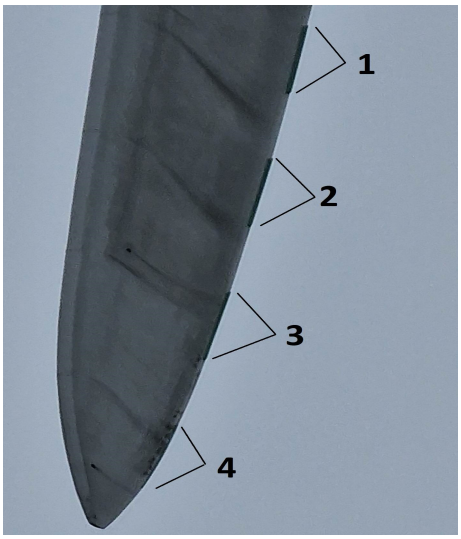

(b) Installed Gurney flaps

(c) Close up of 3 of the Gurney flaps

(d) Close up of the tip Gurney flap

Figure 5.6: Gurney flap installation phase (Picture taken by author of the report, Edwin Bot and Aeroconcept GmbH)

Figure 5.6 helps illustrate the scale of the Gurney flaps with respect to the wind turbine blade. This simple design and add-on feature made it possible to have the installation phase complete in just 4 hours. See timestamps in section 7.1 for the dates of the retrofitted wind turbine in operation. The sectors mentioned in the start of this chapter are shown below:

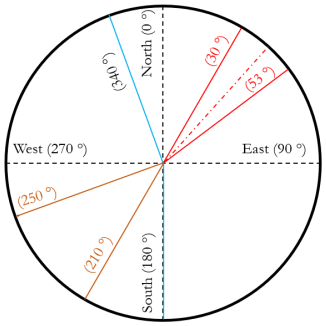

Figure 5.7: Compass plot (Red lines- scanning LiDAR sector; Blue lines- Undisturbed sector)

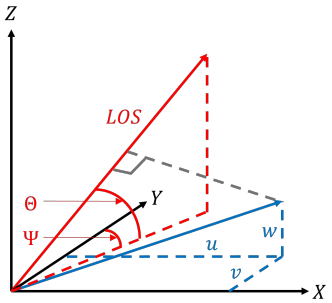

Figure 5.8: Co-ordinate system of Scanning LiDAR

In Figure 5.8, the LOS represents the line of sight of the LiDAR. ψ and θ represent the scanning azimuth and elevation angle in degrees. The changes to the Scanning LiDAR settings were based on changes to the step sizes of the parameters, different bounds or a combination of both. With these changes the time taken for one individual scan changed. Two of the main operation settings are described below.

Firstly, in order to get a thorough three-dimensional description of the wind turbine wake and not compromising too much on the individual scan time, the scan pattern was set as shown in Table 5.1:

Parameter	**Min.**	**Max.**	**Step size**	**No. of unique points**	**Time for 1 Scan (minutes)**	**Total no. of points in ideal scan**
Azimuth (°)	30	52.95	0.15	154	5.5	40656
Elevation (°)	3	7.2	0.6	8		
Range (m)	900	1700	25	33		

Table 5.1: Scanning LiDAR settings 1

With the scan settings shown in Table 5.1, it was ensured that the vertical (altitude) profiles of the wind turbine wake are captured to a reasonable extent. This allowed to analyse the wind turbine wake profiles. One limitation to this pattern was the high scan time which would mean that within a 10-minute period at most 2 samples were available at a point in the wind turbine wake. However, it was an important pattern to get data for the vertical profiles of the wind turbine wake. Upon utilising this pattern for around 1 month, a comprehensive data set for different inflow conditions, such as, different turbulent intensity bins, wind speed and wind direction bins to name a few, was made. A visualisation of this pattern is shown in Figure 5.9

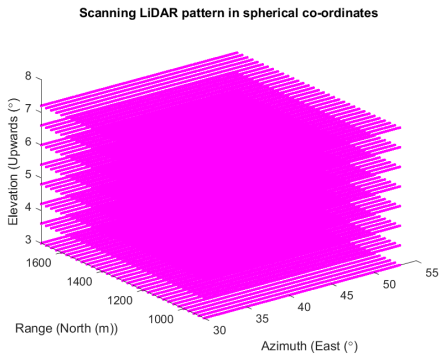

(a) Spherical co-ordinates

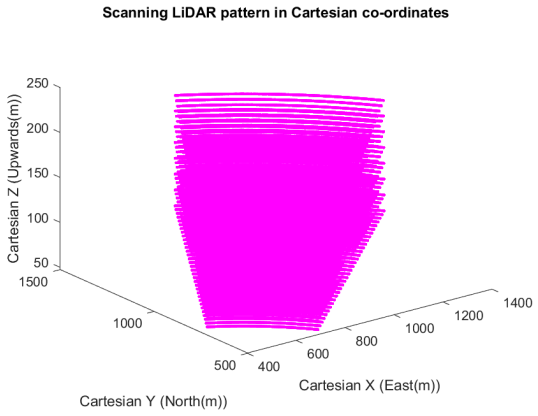

(b) Cartesian co-ordinates

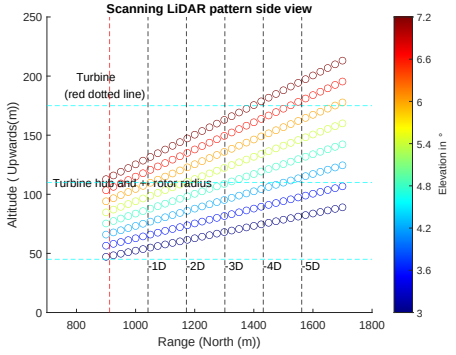

(c) Side view

Figure 5.9: Scanning LiDAR pattern 1 visualisation (Wind turbine is located at ≈ 41.5 deg azimuth)

In order to tackle the limitation of high scan time, a new scan pattern was set as shown in Table 5.2:

Parameter	Min.	Max.	Step size	No. of unique points	Time for 1 scan (minutes)	Total no. of points in ideal scan
Azimuth (°)	30	52.88	0.22	105	2.8	22050
Elevation (°)	4	7.5	0.5	7		
Range (m)	900	1625	25	30		

Table 5.2: Scanning LiDAR settings 2

The scan settings shown in Table 5.2 were set with the objective to have a more accurate representation of the wind turbine wake at hub height. The focus with this pattern was not towards the vertical profile of the wind turbine wake. With this new pattern, more samples in a 10-minute time frame helped for better averaging during data binning as per inflow conditions. The data binning will be explained in the coming section. A visualisation of this scan pattern is shown in Figure 5.10

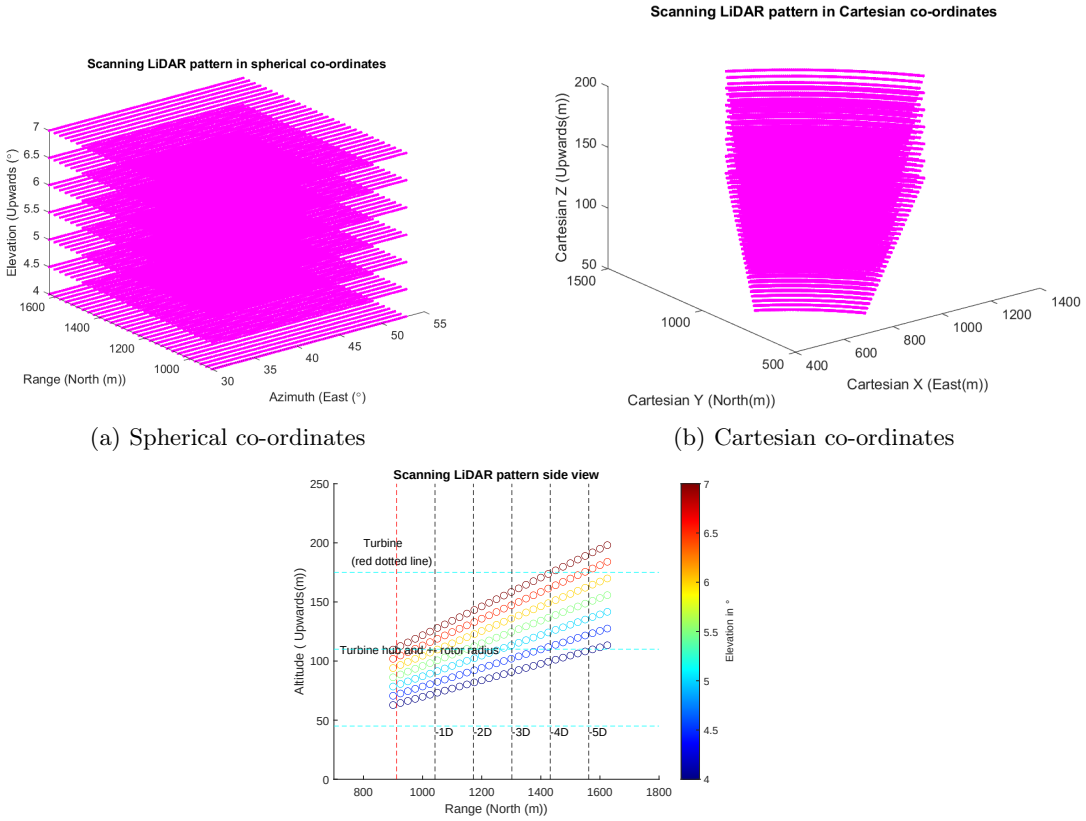

(a) Spherical co-ordinates

(b) Cartesian co-ordinates

(c) Side view

Figure 5.10: Scanning LiDAR pattern 2 visualisation (Wind turbine is located at ≈ 41.5 deg azimuth)

5.2 Processing of LiDAR Data

LiDAR measurements of the wind field work through analysis of laser light reflected from aerosol particles in the air. The frequency of the back scattered laser light is shifted by Δf from its original value $\frac{c_{light}}{\lambda_{wave}}$, due to the Doppler effect, in proportion to the speed of the reflecting particle resolved along the direction of the laser beam, the radial wind speed V_r:

$$\Delta f = \frac{2V_r}{\lambda_{wave}} \tag{5.1}$$

A single LiDAR is thus only able to provide the radial component of wind speed, essentially the wind component in the direction the LiDAR beam is facing. However it is important to retrieve the other

wind components. Apart from this issue, there can also be gaps in LiDAR data. This is because of reduction of back scatter quality. This can happen in certain atmospheric conditions such as heavy fog or cloud. This can be due to too many aerosols and too much absorption. During rain it can be that too many aerosols are removed which also reduces signal quality. In general, aerosol backscatter, relative humidity, precipitation, and atmospheric refractive turbulence affect the LiDAR performance [110]. Such a set of possibly faulty data is reflected in the carrier to noise ratio, provided by the LiDAR (Also see [111, 112, 113] for background information). Having addressed the possible concerns with raw LiDAR data, the following subsections explain the approach followed in this work to tackle them.

5.2.1 Filtering

As explained above, the radial wind speed obtained from the LiDAR can contain faulty data at certain instances. Such data was treated by filtering it in 3 steps:

1. Filtering based on the radial wind speed status output by LiDAR, which is binary 0 or 1. Data with status 0 was filtered out. This status is computed internally by the LiDAR based on Carrier to Noise ratio and Spectrum analysis.

2. Filtering based on the Carrier to Noise ratio output by the LiDAR, which is a number with units decibels (dB). After literature study [114, 115] and analysis on different limits to this ratio, the filtering was done such that data within -23dB to -3dB was preserved. Any other data was filtered out. In particular, in [114], the same LiDAR was used as this study, and thus, the same limits were used here as well.

3. An additional step was taken by using filtering on basis of standard deviation, with data more than 5 standard deviations away from the mean, filtered out.

An example of this filtering effect, a combination of the 2 steps mentioned above, is shown in Figure 5.11.

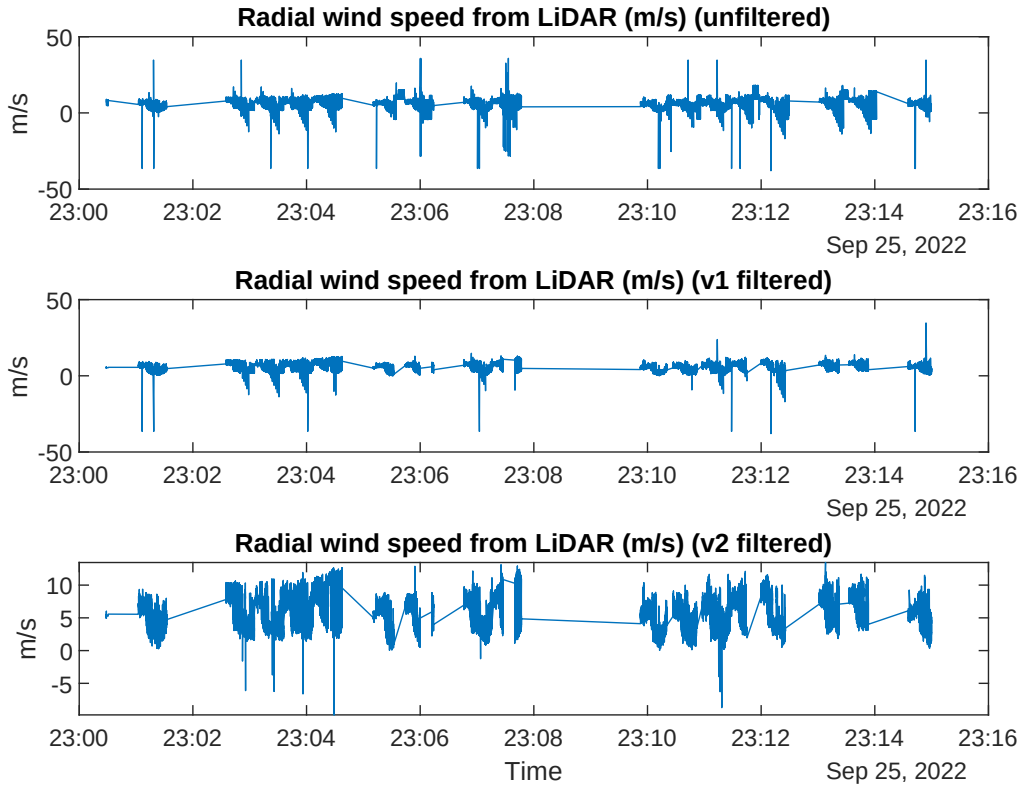

Figure 5.11: Plots showing Filtering of data-set

The steps 1 and 2 of the filtering process were carried out on raw LiDAR data and the step 3 was carried out on the bin-averaged data-set (explanation of data binning in subsection 5.3.1).

5.2.2 Gaussian Process Regression

After filtering of the raw scanning LiDAR data, there were gaps in the LiDAR scan domain (possible reasons were mentioned above). This causes a complete 3-Dimensional visualisation of the wind turbine wake to be lacking. Gaussian process regression (GPR) was used in this work to obtain reliable wind field estimates at these gaps. Gaussian process regression has also been utilised in other research [116, 114]. Here, the Gaussian process regression was implemented on MATLAB [117] to interpolate wind fields in a 3- Dimensional domain.

Gaussian process regression is a non parametric method under Bayesian inversion. Gaussian processes can be seen as an infinite-dimensional generalization of multivariate normal distributions [118]. The Gaussian processes model is a probabilistic supervised machine learning framework that has been widely used for regression and classification tasks. A Gaussian processes regression (GPR) model can make predictions incorporating prior knowledge (kernels) and provide uncertainty measures over predictions. In regression, given some observed data points, infinite number of functions can be used to fit these data points and use them to make predictions at new data points.

In GPR, the Gaussian processes conduct regression by defining a distribution over these infinite number of functions. This is done by means of independent Gaussian correlated to each other as a joint Gaussian distribution. The joint Gaussian distribution is described by the multivariate normal distribution theory defined as:

$$\mathcal{N}(x \mid \mu, \sum) = \frac{1}{2\pi^{\frac{D}{2}} \mid \sum \mid^{\frac{1}{2}}} \exp[\frac{-1}{2}(x-\mu)^T \sum^{-1}(x-\mu)] \tag{5.2}$$

Here, D represents the number of the dimension, $\boldsymbol{x}$ represents the variable, $\mu = \mathbb{E}[x] \in \mathbb{R}^D$ is the mean vector, and $\sum = cov[x]$ is the D X D covariance matrix. The $\sum$ is a symmetric matrix that stores the pairwise covariance of all jointly modeled random variables with $\sum_{ij} = cov(x_i x_j)$ as its (i, j) element.

Upon achieving the multivariate Gaussian distribution, kernels (defining covariance functions) are used to smooth the resulting function. That is, to have close (naturally) response (target values (y_i)) for points with similar predictor values x_i. They specify covariance between the two latent variables $f(x_i)$ and $f(x_j)$ where both x_i and x_j are $d - by - 1$ vectors. In other words, it determined how the response at one point x_i is affected by other points x_j, $i \neq -j$,$i = 1, 2, ..., n$. The covariance function $k(x_i, x_j)$ can be defined by various kernel functions. It can be parameterized in terms of the kernel parameters in vector θ, as $k(x_i, x_j \mid \theta)$. For many standard kernel functions, the kernel parameters are based on the signal standard deviation σ_f and the characteristic length scale σ_l. The characteristic length scale briefly define how far apart the input values x_i can be for the response values to become uncorrelated. Both σ_l and σ_f need to be greater than 0, and this can be enforced by the unconstrained parameterization vector θ [119], such that:

$$for\ same\ length\ scale\ for\ each\ predictor : \theta_1 = \log(\sigma_l), \theta_2 = \log(\sigma_f) \tag{5.3}$$

$$for\ separate\ length\ scale\ for\ each\ predictor :\ \theta_m = \log(\sigma_m),\ for\ m = 1, 2, ..., d\ \ \theta_{d+1} = \log(\sigma_f) \tag{5.4}$$

The choices in MATLAB [120] are among: exponential kernel, squared exponential kernel, Matérn kernel with parameter 3/2 (or 5/2), rational quadratic kernel with or without separate length scale per predictor or a custom kernel function. The different kernels are not described in this report and the reader is referred to [118]. The kernel utilised in this work is the ARD (Automatic relevance determination) Matérn 3/2, that is, the Matérn kernel with parameter 3/2 and a separate length scale per predictor. The standard Matérn 3/2 kernel with same length scale per predictor is given by:

$$k(x_i, x_j \mid \theta) = \sigma_f^2(1 + \frac{\sqrt{3}r}{\sigma_l}) \exp(\frac{-\sqrt{3}r}{\sigma_l}) \ \ where,\ \ r = \sqrt{(x_i - x_j)^T(x_i - x_j)} \tag{5.5}$$

The Matérn 3/2 kernel for various hyper-parameters: standard deviation σ_f and the characteristic length scale σ_l, is shown in Figure 5.12 below:

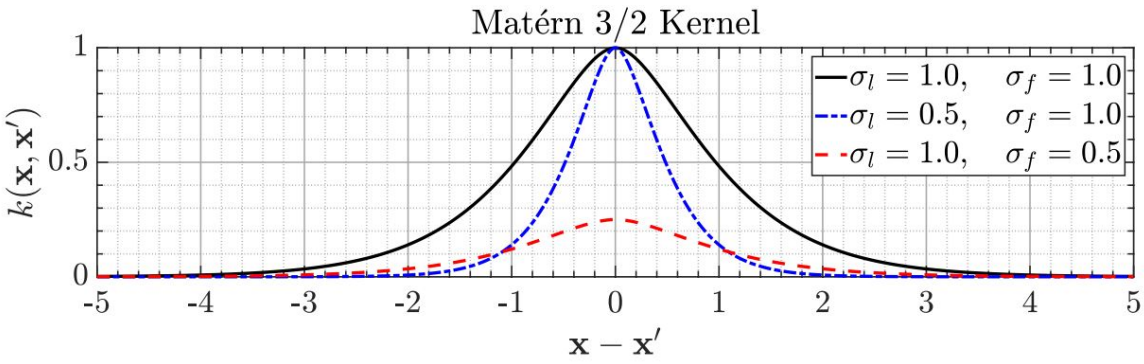

Figure 5.12: Matérn 3/2 kernel for various σ_f and σ_l [121]

Now, a visualisation of the kernel matrix of the Matérn 3/2 kernel is provided in Figure 5.13 below:

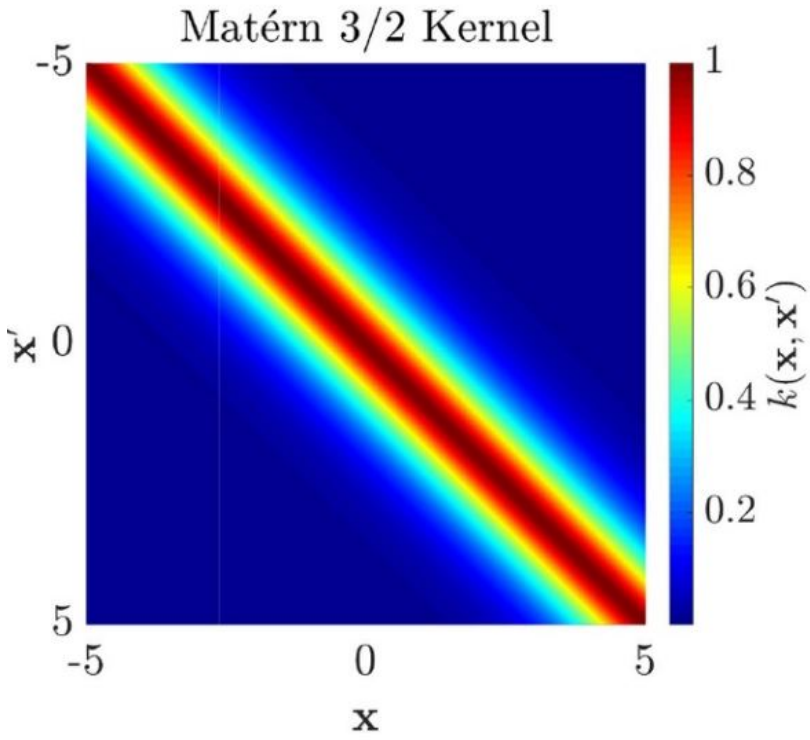

Figure 5.13: Matérn 3/2 kernel matrix for various σ_f and σ_l [121]

Figure 5.12 and Figure 5.13 provide the representation of the Matérn 3/2 kernel with changing hyper-parameters. The optimal choice of the hyper-parameters is made for each predictor by the ARD (Automatic relevance determination) Matérn 3/2 kernel used in this work. The reason of this choice is that Matérn 3/2 kernel is a standard kernel for environmental data and that upon initial testing of different kernels on the data-set, ARD Matérn 3/2 kernel resulted in good match with observations. The ARD Matérn 3/2 is defined as:

$$k(x_i, x_j \mid \theta) = \sigma_f^2(1 + \sqrt{3}r)\exp(-\sqrt{3}r) \quad where, \quad r = \sqrt{\sum_{m=1}^{d} \frac{(x_{im} - x_{jm})^2}{\sigma_m^2}} \tag{5.6}$$

A Gaussian processes model describes a probability distribution over possible functions that fit a set of points. The function (posteriors) updates with new observations. The mean function calculated by the posterior distribution of possible functions is the function used for regression predictions. The regression function modeled by a multivariate Gaussian is given as:

$$P(f \mid X) = \mathcal{N}(f \mid \mu, K) \tag{5.7}$$

Here, $X = [x_1, x_2, ..., x_n]$, $f = [f(x_1, f(x_2), ..., f(x_n)]$, $\mu = [m(x_1), m(x_2), ..., m(x_n)]$ *and* $K_{ij} = k(x_i, x_j)$. X are the observed data points, m represents the mean function, and k represents a positive definite kernel function. With no observation, the mean function is default to be $m(X) = 0$ given that the data is often normalized to a zero mean. The Gaussian processes model is a distribution over functions whose shape (smoothness) is defined by K. If points x_i and x_j are considered to be similar by the kernel, function outputs of the two points, $f(x_i)$ and $f(x_j)$, are expected to be similar. Referring Figure 5.14, given the observed data (red points) and a mean function f (blue line) estimated by these observed data points, predictions are made at new points X_* as $f(X_*)$.

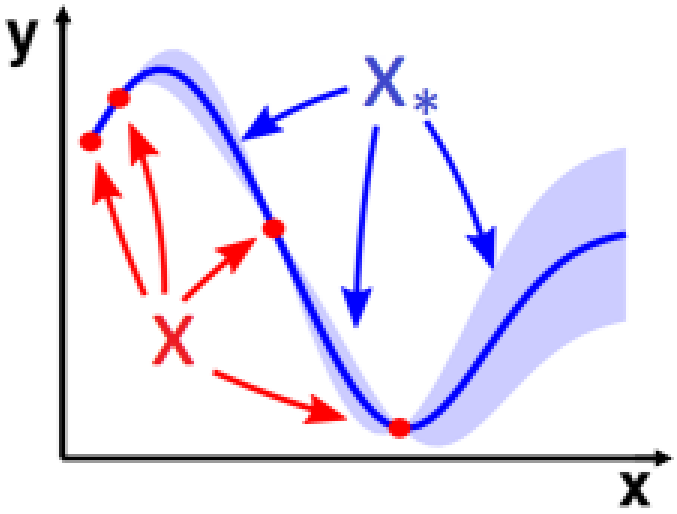

Figure 5.14: A illustrative process of conducting regressions by Gaussian processes. [122]

The joint distribution of f and f_* is expressed as:

$$\begin{bmatrix} f \\ f_* \end{bmatrix} \sim \mathcal{N}\left(\begin{bmatrix} m(X) \\ m(X_*) \end{bmatrix} , \begin{bmatrix} K & K_* \\ K_*^T & K_{**} \end{bmatrix} \right) \tag{5.8}$$

where, $K = K(X, X)$, $K_* = K(X, X_*)$ and $K_{**} = K(X_*, X_*)$. And the mean $(m(X), m(X_*) = 0$. This is the joint probability distribution $P(f, f_* \mid X, X_*)$ over f and f_*, but regressions need the conditional distribution $P(f_* \mid f, X, X_*)$ over f_* only. The derivation from the joint distribution to the conditional results in:

$$f_* \mid f, X, X_* \sim \mathcal{N}(K_*^T K f, K_{**} - K_*^T K^{-1} K_*) \tag{5.9}$$

With noisy variations, that is, $y = f(x) + \epsilon$, assuming additive independent and identically distributed Gaussian noise with variance σ_n^2, the prior on the noisy observation becomes $cov(y) = K + \sigma_n^2 I$. The joint distribution of the observed values and the function values at new testing point becomes:

$$\begin{bmatrix} y \\ f_* \end{bmatrix} \sim \mathcal{N}\left(0 , \begin{bmatrix} K + \sigma_n^2 I & K_* \\ K_*^T & K_{**} \end{bmatrix} \right) \tag{5.10}$$

By deriving the conditional distribution, we get the predictive equation of the Gaussian processes regression as:

$$\overline{f_*} \mid X, y, X_* \sim \mathcal{N}(\overline{f_*}, cov(f_*) \tag{5.11}$$

where, $\overline{f_*} \triangleq \mathbb{E}[\overline{f_*} \mid X, y, X_*$, which is further $= K_*^T [K + \sigma_n^2 I]^{-1} y$; and $cov(f_*) = K_{**} - K_*^T [K + \sigma_n^2 I]^{-1}] K_*$.

5.2.3 Implementation

With the background provided on the Gaussian process, this section explains the implementation in this work. The machine learning model has been utilised using the MATLAB [117] function, 'fitrgp'.

The predictor array was set to the LiDAR scanning azimuth, elevation and range. The response array was the bin- averaged LiDAR obtained radial wind speed. Upon implementation of the Gaussian process an estimate of the wind field at missing data points (such as on filtered out points) was obtained, with reasonable uncertainty. An example of this is shown in Figure 5.15.

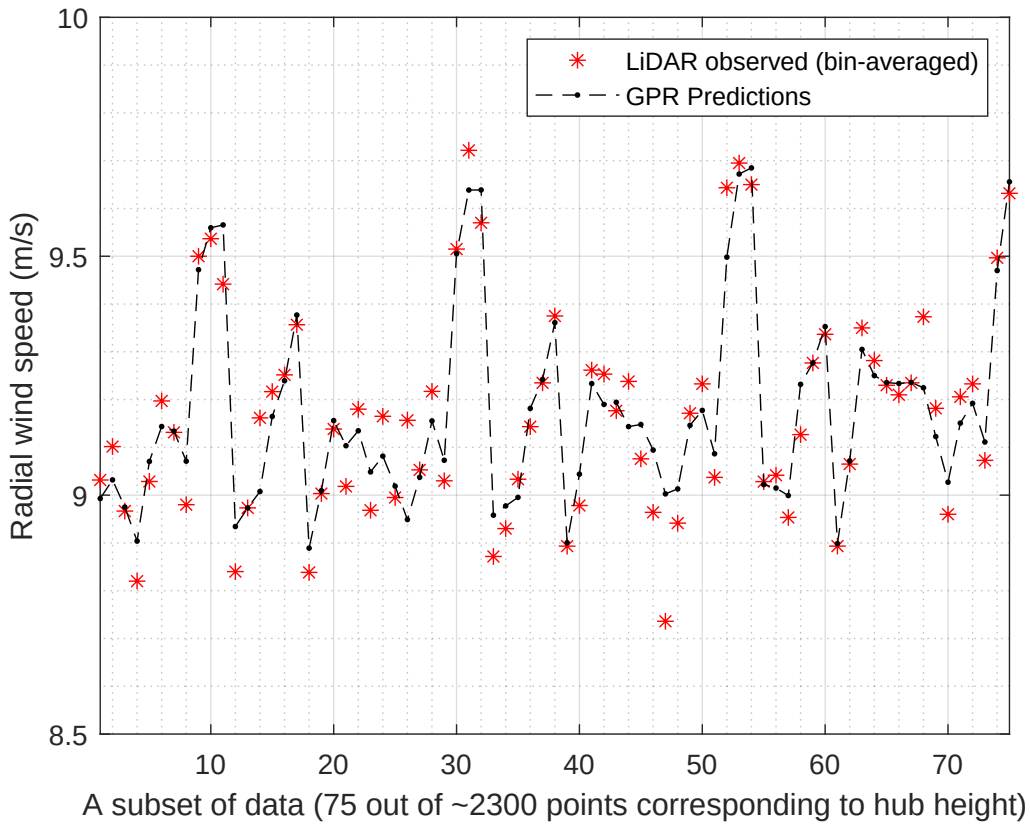

Figure 5.15: An example visualisation of the Gaussian process regression results

Figure 5.15 above shows a zoomed view of the data-set and only focuses on 125 data points out of the over 22000 data points (Table 5.2) in a single pattern. This figure is made for the points corresponding to some of the points corresponding to the hub height of the wind turbine in study. The machine learning model was trained on $(\frac{1}{3})^{rd}$ of the data-set, such that closely related points are not taken into the training set. The Gaussian process regression was carried out on the bin-averaged data-set. This implies that the radial wind speed at each unique azimuth, elevation and range was averaged from their respective bins (explained in subsection 5.3.1). Figure 5.15 shows the LiDAR obtained radial wind speed and the GPR predictions. It can be seen that with the introduction of the GPR model to the post-processing chain, the radial wind speed at certain points is adjusted as per the model's response. This adjustment helps add smoothness to the data set and take care of certain outliers. This adjustment can however be accepted because there is an inherent standard error in the bin-averaged LiDAR data. To further evaluate the usage of the GPR model, Figure 5.16 shows the standard error of the bin-averaged LiDAR data at hub height; where:

$$Standard\ error = \frac{\sigma_{RWS_{binned}}}{\sqrt{N_{samples}}} \tag{5.12}$$

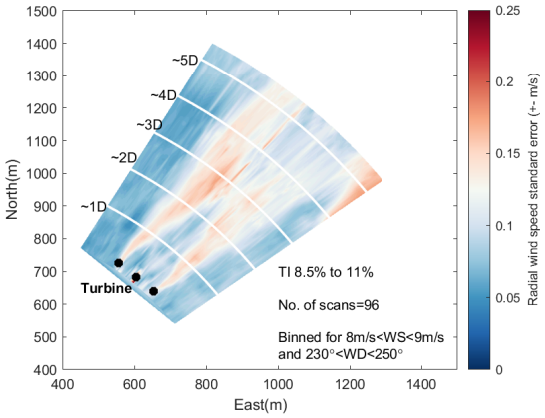

Figure 5.16: Example for standard error of bin-averaged LiDAR data at hub height

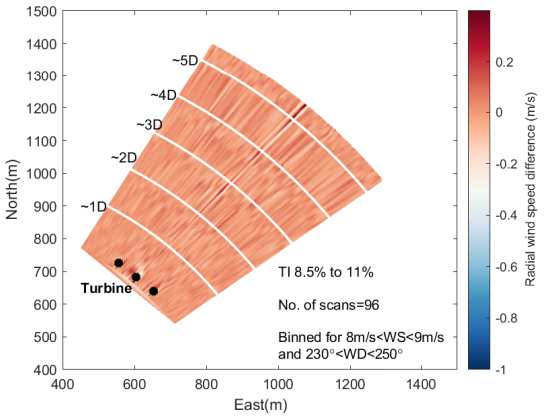

Figure 5.17: Example for difference between GPR predictions and bin-averaged LiDAR data at hub height

In Equation 5.12, $\sigma_{RWS_{binned}}$ represents the standard deviation of the bin-averaged data set samples and $N_{samples}$ represents the number of samples in a particular bin. Figure 5.17 illustrates the difference of results of GPR predictions and the bin-averaged LiDAR data. With Figure 5.15, Figure 5.16 and Figure 5.17 the validation of the implementation of the GPR model is provided. This is done for an example case of the inflow conditions as mentioned in the plots, which correspond to the baseline case of Figure 7.6. This implementation is then followed for all the results in this report, which allows for an enhanced representation of the wind turbine wake. The next subsection explains how the necessary wind components were retrieved from the single LiDAR given radial wind speed.

5.2.4 Retrieval of Wind Component

The wind turbine wakes analysed in this study are in the wind sectors which are not affected by the neighbouring wakes. Since the scanning LiDAR only provides the radial component of wind speed, assumptions were made to retrieve the necessary wind speed components. The choice of sectors makes the retrieval of the necessary wind components less challenging and less prone to error, which is discussed below. First, the method utilised in this study is discussed and then it is validated against the commonly used methods of wind component retrieval.

Using geometric relations the following equation was used to write the radial velocity in terms of the u, v, w components and the Scanning LiDAR's scanning azimuth (ψ) and elevation (θ) as follows:

$$V_r = u \sin\psi \cos\theta + v \cos\psi \cos\theta + w \sin\theta \tag{5.13}$$

This follows from Figure 5.8, where the sign convention followed is that the 0° azimuth points to the North and 90° East and so on. The elevation is 0° in the horizon and increases towards zenith in the vertical plane. Furthermore, the horizontal wind speed V_h and the wind direction α can be determined as follows:

$$V_h = \sqrt{u^2 + v^2} \tag{5.14}$$

$$\alpha_{WD} = \arctan\frac{u}{v} \tag{5.15}$$

As seen in Equation 5.13, there are three unknowns (u, v, w) but only one equation. This is commonly known as the Cyclop's dilemma [111]. Two assumptions were made solve the equation. Firstly, the w component (vertical) was assumed to be zero, as it can be considered negligible (very low elevation angles (as seen in Table 5.1 and Table 5.2), lead to a small sine component). Secondly, it was assumed that the wind direction is homogeneous throughout the wind turbine wake (similar to approach in, for example, [123]). This wind direction was assumed as the inflow wind direction at the hub height of the wind turbine under study, $\approx 2.2D$ upstream. These assumptions lead to the following relations:

$$V_h = \frac{V_r}{\cos(\overline{\alpha_{WD}} - 180 - \psi)}) \tag{5.16}$$

$$V_{\parallel \; to \; Turbine \; axis} = Longitudinal \; component = \cos(\overline{\alpha_{WD}} - \overline{\alpha_{Yaw}}) * V_h \tag{5.17}$$

$$V_{\perp \; to \; Turbine \; axis} = Lateral \; component = \sin(\overline{\alpha_{WD}} - \overline{\alpha_{Yaw}}) * V_h \tag{5.18}$$

In the above equations, $\overline{\alpha_{WD}}$ represents the mean wind direction of the incoming wind and $\overline{\alpha_{Yaw}}$ represents the mean wind turbine yaw angle. Using these simple assumptions the necessary wind components were retrieved. Next, the validation for the use of these assumptions is provided.

5.2.4.1 Validation

The most common approach in resolving the Cyclops' dilemma mentioned above is to use a non linear least square fitting method to solve Equation 5.13. The assumption for $w = 0$ is commonly used because of the inability of the LiDAR to measure the vertical wind component at very low elevation angles. This method can be found in plenty of research, for example, [124, 125, 126]. The results of the above mentioned simple reconstruction technique is validated with the non linear least square fitting and a slightly sophisticated Maximum A Posteriori (MAP) method.

For the non linear squares method, the Equation 5.13 is used with $w = 0$ and the Levenburg-Marquardt algorithm is used to fit the u and v components, given the radial wind speed (V_r) and the scanning LiDAR azimuth (ψ) and elevation (θ) in a non linear least squares sense. The Maximum A Posteriori method (see [127, 128] for a short overview) is a Bayesian estimation which incorporates prior belief about the unknowns, and then the posterior distribution of the unknowns is updated. This method is equivalent to the commonly used Maximum Likelihood estimation (MLE) when the said priors are uniform, that is, equal distribution of probabilities. The reader is referred to [129, 130] for detailed background on these techniques. The use of UQLab [131] was made for implementation of the Maximum A Posteriori method.

The prior belief was given as a Weibull distribution with $\lambda = 8.6$ and $k = 2.4$ for the u component; $\lambda = 5.3$ and $k = 1.4$ for the v component. To decide the prior belief, a data set of wind speed measurements at the hub height of the research wind turbine under study, which is $110m$, was used. The data set was made for the wind directions in sectors of interest, which is, 190 deg to 250 deg, as mentioned in the start of this chapter as well. In this wind sector (South by West to West-Southwest) it is evident that the u component will be in the Westerly direction and v component in the Southerly direction, which will imply negative values. So the signs were revered and then fit into the standard Weibull distribution. The Weibull fit to this data set is shown in section A.3. Additionally, the Gaussian distribution is shown for the w component, which further supports the assumption of $w = 0$ in the analysis. It should be noted that in the wind turbine wake, the said prior belief will not completely hold true, for one, because the wake will have wind speed deficits. This will likely shift the distribution peak in both wind speed and probability axes, or altogether result in a different distribution. However, with no means of determining the u, v components' distribution in the wake, the above mentioned priors are utilised. Another point of concern could be that the prior belief is based on hub height wind speed, while the scanning LiDAR is used for measurements at different altitudes as well.

With this, a short discussion on the approach used for the 3 methods, which are, simple wind direction assumption, non linear least squares fitting and Maximum A Posteriori estimation, is provided. The below figures compare the results of the three methods. The comparison provided here is on basis of the inflow conditions in Figure 7.1, with the baseline case of low TI. First, the contours are shown at hub height, for the non linear least square fitting and Maximum A Posteriori estimation (to avoid confusion with the different color map limits, the simple wind direction assumption method result is not provided here and can be found in Figure 7.3a which has the necessary (different) color map limits). Then, the contours at hub height illustrating the wind speed difference from the method of simple wind direction assumption are provided. The green dots on the contour indicate the 50% span point in the wind direction axis at the different downstream distances (see section 7.1 for more information).

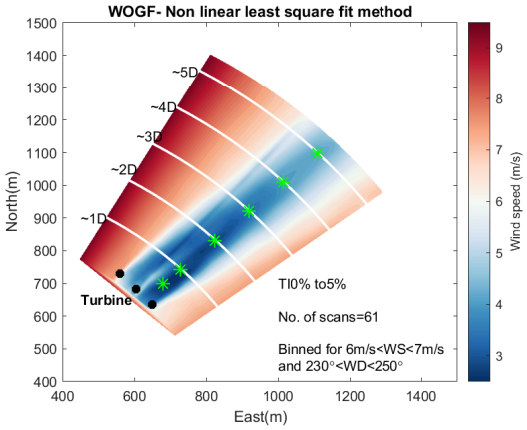

(a) Non linear least square fitting comparison (note the higher than inflow wind speeds, particularly on the left edge of the scan)

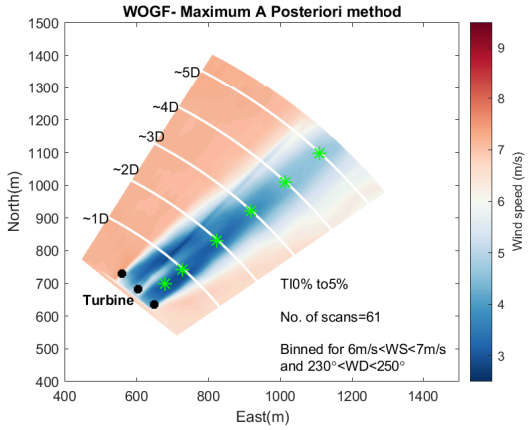

(b) Maximum A Posteriori estimation comparison

Figure 5.18: Horizontal wind speed ($\sqrt{u^2+v^2}$) ($6m/s < U_{\infty,hub} < 7m/s$)

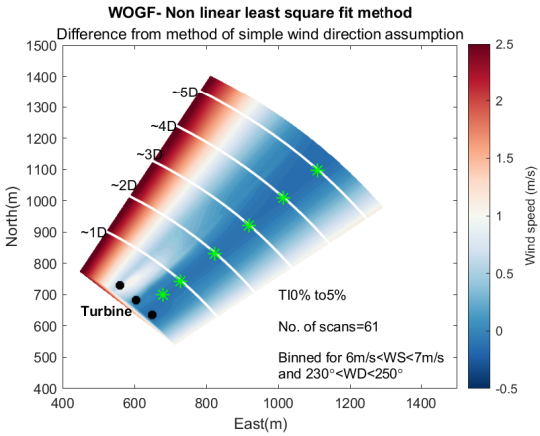

(a) Non linear least square fitting comparison (note the higher color map upper limit)

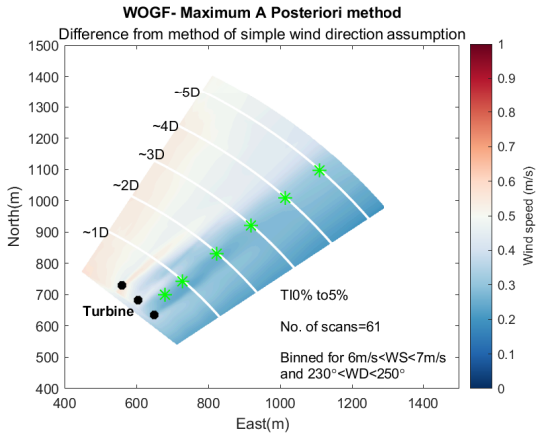

(b) Maximum A Posteriori estimation comparison

Figure 5.19: Horizontal wind speed ($\sqrt{u^2+v^2}$) difference ($6m/s < U_{\infty,hub} < 7m/s$)

From Figure 5.18a and Figure 5.19a it is seen that the non linear least squares method has higher values from the simple wind direction assumption method, when away from the wind direction axis. This implies that the wind direction estimates from the non linear least squares method is quite different from the inflow wind direction, which averaged to 240 deg. The reconstructed wind direction of the points at hub height was checked for. It was found that the non linear least squares method has the reconstructed wind direction ranging from 185 deg to 240 deg. It seems unlikely to have such a large variation in the wind direction. This is also evident from the high wind speed in the free stream on the left edges of the scan pattern. The free stream conditions were in the bin $6-7m/s$ while there are clearly higher values from the non linear least square fit method. For more clear difference of wind speed see Figure 5.19a.

On the other hand, this is not seen in the Maximum A Posteriori estimation (Figure 5.18b), as the reconstructed wind direction ranged from 200 deg to 210 deg, which is more realistic than the non linear least square fit method. The wind speed difference here is within $0.5m/s$ at majority of the points. Finally, the differences at all points (not only hub height) become clear with the histograms shown below:

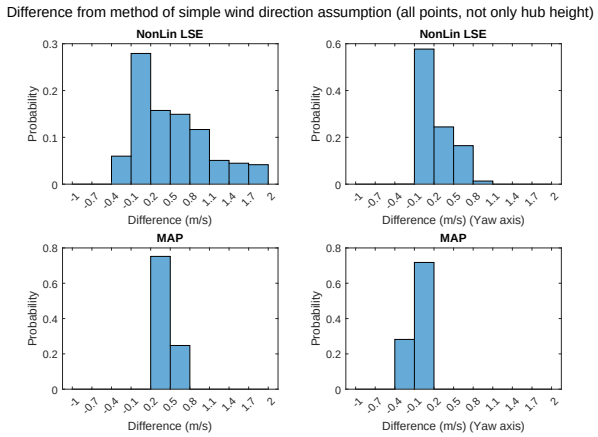

Figure 5.20: Comparison of different methods of wind component retrieval ($6m/s < U_{\infty,hub} < 7m/s$)

From Figure 5.20 it is clear that the difference in the methods is mainly within $\pm 0.5m/s$, lower for the yaw axis component (Equation 5.17). Since all methods are relying on assumptions, there is uncertainty associated with each of them. For further insights into the results of different methods, the vertical profiles are shown below:

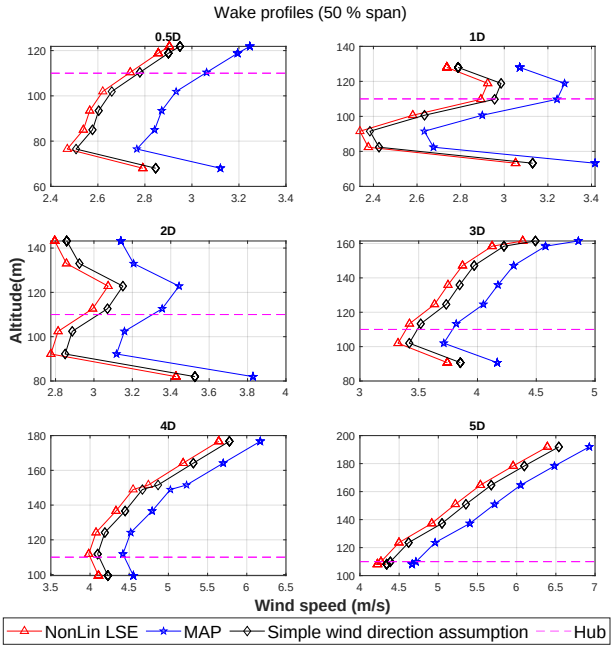

Figure 5.21: Vertical profile comparison of different methods of wind component retrieval ($6m/s < U_{\infty,hub} < 7m/s$)

As evident from Figure 5.20, the yaw axis component is very similar in the different methods, so only the horizontal component has been plotted in Figure 5.21. Note that the non linear least square fit method estimate is found to be close to simple wind direction, when analysing 50% span point (also seen in Figure 5.19a, with less differences (darker blue colour) than the Maximum A Posteriori method near wind direction axes). The vertical profiles reveal that the wind components are only differing in magnitude and are remaining same in the variation across the altitudes. However, when looking at all the points, considering the unrealistic wind direction estimate and the considerably higher than inflow wind speed speed estimates by the non linear least square fit method, it is decided to use the simple wind direction assumption method for the wind component retrieval in this study; due to the computational ease and from the comparison it proves to be more applicable in the sectors of wake analysed in this study.

5.3 Data Binning

In the previous section the processing of the LiDAR data was explained. The processing of the scanning LiDAR data involved use of various steps. But, the processing of the turbine performance data was simplified and done by means of use of 10 minute measurement data; the filtering was done on basis of NaN values, turbine status (to ensure normal operation), following which data binning was conducted. So, for the turbine performance data, directly the data binning is explained. In this section, first, the data binning of the wake analysis data sets is explained and then, retrofitted wind turbine performance analysis data sets are explained.

5.3.1 Wake Analysis

It was mentioned that the Gaussian process regression and the wind component retrieval was conducted on bin-averaged data set of the scanning LiDAR data used for wake analysis. This section explains the parameters taken into account to create this bin-averaged data set of the scanning LiDAR data. See section 7.1 for time stamps of the testing period. For the data binning, the 10 minute averaged measurement data of the following parameters was considered:

1. Wind direction measured by ground based profiling LiDAR.
   (a) The wind direction bins chosen were between $190 - 250°$ with respect to North, at hub height of $110m$, in steps of $20°$. With the scanning LiDAR orientation, this region allows for a proper capture of the wind turbine wake up to $4 - 5D$ downstream depending on the yaw angles.
   (b) This binning took care of yaw angles and yaw misalignment parameters, if not, additional filtering was done to have the bounds correctly set.
2. Wind speed measured by ground based profiling LiDAR.
   (a) The wind speed bins between $6m/s$ and $11m/s$ at hub height of $110m$, in steps of $1m/s$ were used.
3. Turbulence intensity calculated from ground based profiling LiDAR measurements.
   (a) The turbulence intensity bins were chosen as $0 - 5\%$, $5 - 8.5\%$ and $8.5 - 11\%$ at hub height of $110m$. The turbulence intensity was defined as Equation 5.19, where σ_{U_∞} is the standard deviation of the free-stream wind speed (at hub height) in a 10 minute interval and $U_{\infty,avg}$ is the average free-stream wind speed (at hub height) in a 10 minute interval:
   $$TI = \frac{\sigma_{U_\infty}}{U_{\infty,avg}} \tag{5.19}$$
4. Atmospheric stability was checked for, explained in section 5.4.
5. The wind shear exponent that is typically used by a power law assumption was not directly included in the binning procedure in this study. This is because of the uncertainty with the wind speed profile fit to be used (for example, see [132] for the effect of different wind shear profiles). The empirical constants seen for these models were mostly found for offshore wind farms and thus it was decided to not use it in this study for the onshore wind farm. However, as seen in (for example, Figure 7.1) the wind inflow profiles were checked for at the last stage and if need be an additional filtering was done to the data (for reference, if the difference of power law exponent of the baseline and retrofitted case was greater than 0.1 then the additional filtering was done).
6. Subsequent checks on wind turbine operational parameters of power output, rotor speed, blade pitch were done, which are individually discussed in the results of field tests. This is because, at times, the data binning as per the 5 steps mentioned above could lead to variations in the wind turbine operational parameters. For example, during a low wind speed period with a gust. This leads to high 10 minute mean value of wind speed but the turbine power performance could be varying through the 10 minute period which will lead to different effects on the wake. Such period could be identified generally by the standard deviation statistics of the performance parameters stated above, but do need a careful check before finalising the data (one such anomaly is shown in Figure B.6).

5.3.2 Aerodynamic and Structural Performance Analysis

The second component of the field tests was the analysis of the retrofitted wind turbine aerodynamic and structural performance in comparison to the baseline configuration. See section 7.2 for time stamps of the testing period. The bins for the retrofitted wind turbine performance comparison have been made the 10 minute averaged measurement data of the following parameters:

1. Wind direction measured by ground based profiling LiDAR.
   (a) The entire undisturbed wind sector was chosen, that is, $180 - 340°$ with respect to North, at hub height of $110m$. The reason for a broader sector than the one in wake visualisation is that the scanning LiDAR sector does not have to be taken into account and the wider undisturbed sector allows for more samples.
2. Wind speed measured by ground based profiling LiDAR.
   (a) The wind speed bins chosen were between $4m/s$ and $25m/s$ at hub height of $110m$, in steps of $1m/s$. This is to take into account cut in wind speed to roughly the cut out wind speed.
   (b) A bin higher than cut in wind speed of $3m/s$ was chosen because it was found that $3-4m/s$ had high standard deviations associated with start up times.
3. Turbulence intensity calculated from ground based profiling LiDAR measurements.
   (a) The turbulence intensity range between $0 - 15\%$, at hub height of $110m$ was chosen.
   (b) The turbulence intensity was defined as in Equation 5.19.
   (c) Considering the limited data set, a broad TI range was chosen to get most number of samples.
4. Because a broad TI range is chosen, here a power law wind shear exponent was directly taken into account to avoid excessive wind shear bias in the retrofitted case of low samples; and $\alpha_{pow,exp} \leq 0.3$ was chosen.
5. Yaw misalignment was ensured within ± 15 deg as a reasonable range to distinguish the effect of yaw misalignment on the performance.
6. A criterion for minimum number of 10 minute samples was set to 5 to ensure reasonable averaging.
   (a) The resulting count of each statistics (for the retrofitted case) is indicated on the plots in the results in section 7.2.
   (b) The counts can be different in the different parameters for the same wind speed bin, which implies that not all parameters had an equal signal availability. For example, in the $7-8m/s$ bin, the number of 10 minute sample for the retrofitted case power assessment was 64 but the flapwise bending moment signal had only 13, because of more NaNs in the flapwise bending moment signal.

5.4 Atmospheric Stability

To ensure that the comparison of the baseline and the retrofitted configuration is done during similar atmospheric conditions, the site assessment was done by use of the ground based profiling LiDAR and a met mast. Literature about atmospheric stability analysis can be found in, for example, [133, 132, 134, 135]. To determine the atmospheric stability bins, the table from [135] was utilised:

Stability	Monin- Obukhov length (m)
Strongly unstable	$-100 \leq L_{M-O} \leq -50$
Unstable	$-200 \leq L_{M-O} \leq -100$
Near- neutral	$\lvert L_{M-O} \rvert \geq 500$
Stable	$50 \leq L_{M-O} \leq 200$
Strongly stable	$10 \leq L_{M-O} \leq 50$

Table 5.3: Atmospheric stability for the bin- vise averaged data sets ([135])

In Table 5.3 the parameter for different atmospheric stability bins is listed in terms of the Monin-Obukhov length. Originally the Monin- Obukhov length [136] is formulated as:

$$L_{M-O} = -\frac{\overline{\theta_v} u_*^3}{\kappa g \overline{w'\theta'_v}} \tag{5.20}$$

The Monin-Obukhov length can be interpreted as the height in the stable surface layer below which shear production of turbulence exceeds buoyant consumption. In the above equation, the bars represented the mean value and the prime (') represents the fluctuating component, usually calculated over 30 minute period [137, 138, 139]. The term θ_v is virtual potential temperature, u_* is the friction velocity, κ is the Von- Kármán constant, g is the acceleration due to gravity and $\overline{w'\theta'_v}$ is the kinematic sensible heat flux. The friction velocity is formulated as $((\overline{u'w'})^2 + (\overline{v'w'})^2)^{\frac{1}{4}}$. The virtual potential temperature serves as a stability criterion for an atmosphere with moisture gradient. When θ_v is constant a statically neutral atmosphere is implied, when it is decreasing with altitude an unstable atmosphere and when it is increasing with elevation a stable atmosphere. The virtual temperature, a temperature at which dry air would have density as moist air at a given pressure can be measured to calculate the virtual potential temperature [124]. u, v, w represent the wind components. The fluctuating components in these above equations make it necessary to use high- frequency data to retrieve them. With no availability of this data, specially the wind components near the surface layer, this method could not be utilised in this study. Alternatively, the calculations for the Monin-Obukhov length (L_{M-O}) can be done by a variety of methods ([140, 80, 141]) depending on the availability of data and discretion based on the measurement equipment accuracy. Here the bulk Richardson number (RI_b) method ([142]) was utilised (also utilised in, for example, [132, 134, 143, 144]) and the following steps were followed:

1. Calculation of the Richardson number (RI) with the formulation:

$$RI = \frac{g\Delta\overline{\theta_v}\Delta z}{\overline{\theta_v}(\Delta\overline{u})^2} \tag{5.21}$$

2. Considering surface conditions of $u(z_0) = 0m/s$ and taking the reference height as the wind turbine hub height.

3. For the virtual potential temperature, a multi step approach had to be utilised since it was not directly available from the measurements. The temperature (T), pressure (p) and relative humidity (RH) (the proportion of the vapor pressure to the pressure of the saturation vapour) recorded at $2.5m$ (assuming the data here as the surface data) and the hub height of $110m$ were utilised (thus $\Delta z = 107.5m$).

   (a) First the potential temperature (θ) was calculated as (temperature that an air parcel would attain if adiabatically brought to a standard reference pressure of $p_0 = 1e5Pa$):

$$\theta = T\left(\frac{p_0}{p}\right)^{\frac{R_g}{c_p}} = T\left(\frac{p_0}{p}\right)^{0.286} \quad for\ air \tag{5.22}$$

   (b) In the above equation R_g is the gas constant and c_p is the specific heat capacity.

   (c) Next, the Clausius-Clapeyron equation with the August–Roche–Magnus formulation [145] was used and the specific humidity (SH) (mass of water vapour per unit mass of moist air) was found using the measured relative humidity (RH):

$$SH = \frac{RH}{0.263p}\exp\left(\frac{17.67(T - T_0)}{T - 29.65}\right), T_0 = 273.16K \tag{5.23}$$

   (d) Next, the mixing ratio (ratio of mass of water vapour to mass of dry air) was found out as :

$$r_m = \frac{SH}{1 - SH} \tag{5.24}$$

   (e) Finally the virtual potential temperature, under the assumption of unsaturated air with mixing ratio r_m was calculated as [146]:

$$\theta_v = \theta(1 + 0.61 r_m) \tag{5.25}$$

(f) This step was done for both $2.5m$ and the $110m$ height and the Δ terms were found and substituted in Equation 5.21.

4. Lastly, upon calculation of the bulk Richardson number, the following relation was used to find the L_{M-O}:

$$\frac{z}{L_{M-O}} = \begin{cases} \frac{10RI}{1-5RI} \;\; if \; RI \geq 0 & \text{(5.26a)} \\ 10RI \;\; if \; RI \leq 0 & \text{(5.26b)} \end{cases}$$

The inflow conditions were obtained by use of a ground based profiling LiDAR and a met mast on the site. For relative humidity RH, pressure p and temperature T the met mast was used and for the wind speed and the corresponding turbulence intensity, the profiling LiDAR was used (mainly because it was specially located upstream of the wind turbine outside the induction zone. With the L_{M-O} calculated, the correspondence to the turbulence intensity as per Table 5.3 was checked for the measurement period, apart from some other statistics calculated to see the trend of the atmospheric conditions through the day and the winter months (see section 7.1 for the duration of testing specially for the wind turbine wake). The resulting statistics (for the undisturbed wind sector of $180° - 340°$) are shown below:

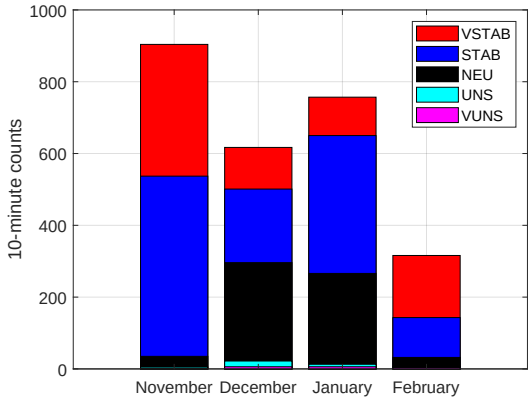

Figure 5.22: Monthly variation of stability conditions

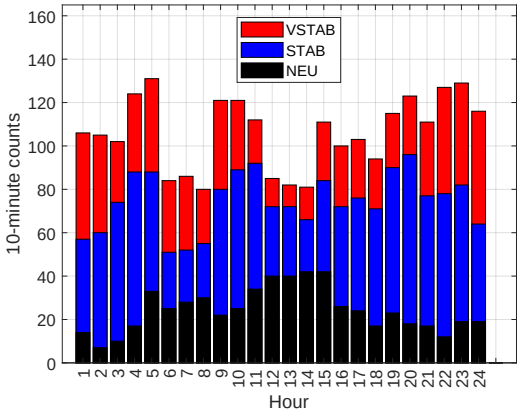

Figure 5.23: Hourly variation of stability conditions (all 4 months inclusive)

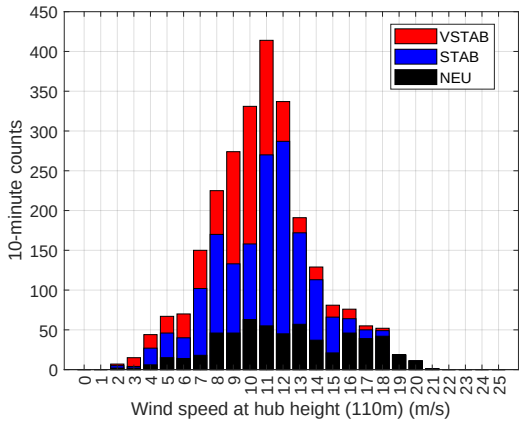

Figure 5.24: Wind speed variation with stability conditions (all hours and 4 months inclusive)

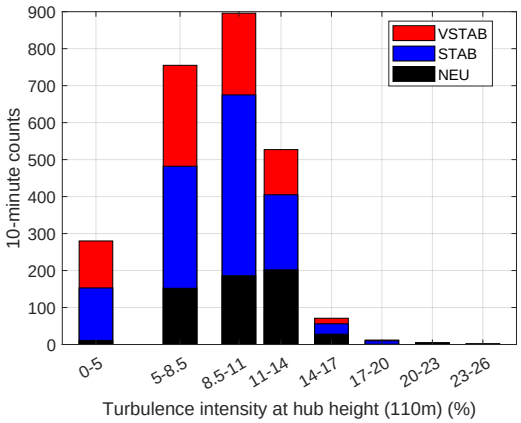

Figure 5.25: Turbulence intensity variation with stability conditions (all hours and 4 months inclusive)

In Figure 5.22 the monthly variation shows that during the winter months at the wind farm in this study, the unstable conditions are hardly present. This was also found to be the case [134] for the

Egmond aan Zee Offshore Wind Farm (OWEZ) located off the coast of Netherlands. Thus, in this study, it should be noted the wakes are under prevailing stable or neutral atmospheric conditions, owing to the testing period during the winter months (section 7.1). When looking at Figure 5.23 there is not a clear trend of the atmospheric conditions through the hours. Some indications of more neutral conditions during noon time while stable conditions during the night time, as expected; as likely during the night, the stable layers of air will be associated with light winds and a surface that is cooler than the air. Since the unstable conditions are hardly present, Figure 5.23 to Figure 5.25 are shown only with the prevailing atmospheric conditions. In Figure 5.24 the component $\sqrt{u^2 + v^2}$ is shown and not just u, as was used in Equation 5.21. It can be seen that with the neutral conditions, the higher wind speeds prevail more. This was also seen for the OWEZ wind farm. With Figure 5.25 the lower turbulence region being dominated by stable conditions is clear. The data set used to make the above plots corresponds to 0.66%, 1.08%, 22.51%, 46.34% and 29.41% for very unstable, unstable, neutral, stable and very stable conditions respectively (This was for a total of 2594, 10 minute samples, after filtering out the data which did not lie in the atmospheric stability bins as mentioned in Table 5.3). It is also important to note the varied turbulence regime in the stability conditions. Thus, a direct correspondence of each atmospheric stability bin with a range of turbulence intensity cannot be made. Similar results were found in, for example, the study for OWEZ wind farm in [147]. Their analysis also indicated that while TI is generally lower in the stable class this assumption cannot be uniformly applied due to the wide range of TI in both stable and unstable classes. From Figure A.3 and Figure A.7, the trend of turbulence intensity with the wind speed can also be observed.

5.5 Summary

The set up of the field tests was explained on this chapter. The retrofitting of the wind turbine with segmented Gurney flaps was discussed as well. The use of a ground based profiling LiDAR and a met mast was made for assessment of inflow conditions. The use of Scanning LiDAR to visualise the wind turbine wake was explained. The scan pattern setting and the scan times were explained. The fastest scan time results in about 3 radial wind speed samples at the same point, in a 10 minute interval which allows for smooth averaging in a bin- averaged data set. The processing of data was explained which included, standard filtering procedure and Gaussian process regression on the bin-averaged data set, to interpolate at missing points of data and smooth the wind speed variations. The Cyclop's dilemma to tackle the wind component retrieval was resolved by use of simple homogeneity assumptions in regards to the wind direction. This method was found to be more reliable than two other methods, non linear least square fitting and Maximum A Posteriori.

The data binning procedure was explained in detail. The data binning involved the binning a per wind direction, wind speed and turbulence intensity bins, and other checks on the data, to ensure similar turbine performance. The data binning was explained for the wind turbine wake analysis data set and the performance analysis data set. With the binning method used, it was ensured that the following wake visualisations will be conducted within the correct atmospheric stability conditions and ensure a fair comparison of the baseline and retro-fitted wind turbine case. The bulk Richardson number method was used to determine the Monin-Obukhov length and subsequently classify the atmospheric stability. This chapter forms the basis of the field test results. The next chapter explains the set up of the simulations.

Chapter 6

Setup of Simulations

Contents

In the previous chapter, the field test set up and data post processing was explained. This study also involves conducting simulations, to further validate field tests results and cope with certain limitations in field tests. For the wind turbine wake analysis in simulations, the use of NREL OLAF was explained in section 4.2. As mentioned previously, the performance analysis in simulations was done with the conventional approach of using dynamic blade element momentum theory, which is, blade element momentum theory simulations in dynamic inflow conditions. In this chapter, the wake and performance analysis setup and validation in the simulation environment are discussed in the respective sections.

6.1 Wake Analysis

The wake simulations were done for the wind speed bin of $10m/s - 11m/s$. This choice was made because this wind speed bin falls at the highest thrust of the wind turbine under study. Additionally, it was seen in the field tests that in this wind speed bin, the wake of the retrofitted wind turbine was significantly different from the wake of the baseline wind turbine.

It should be noted that the aim of this wake simulation was to validate the faster breakdown of the tip vortices by the segmented Gurney flaps. That is, to validate the effect of the change in lift and circulation distribution brought about on the wind turbine blade upon addition of segmented Gurney flaps. As blade resolved was not considered in the scope of this study, the $3 - D$ boundary layer effects that would have been the case for the reality where the Gurney flaps protrude perpendicularly from the wind turbine trailing edge are not simulated. It should also be noted that owing to the limitation of vortex filament method in solving the velocity field upon vortex breakdown, the far wake cannot be accurately solved. The turbulent mixing cannot be modelled by the vortex filament method (also see [148]). The velocity profiles after the wake breakdown may be erroneous and so these are not considered, and the focus of the set up is only on evaluating the change in breakdown position.

The simulations were conducted in steady and uniform inflow conditions to distinguish the effects of the segmented Gurney flaps on the wind turbine wake. With the scope of the wake simulations discussed above, the important parameters of the OLAF input file are discussed here. The table below lists the important setup parameters:

Parameter	**Value**
Azimuthal discretisation	5 deg
Circulation solving method	Cl-based iterative method
Near wake (fully free)	31 rotations
Viscous diffusion parameter (δ)	7.5
Viscous diffusion function	Vatistas ($n = 2$)
Inital core radius (r_{c0})	$0.6dr_{min}$
Core radius evolution	Wake age

Table 6.1: NREL OLAF inputs

The azimuthal discretisation, that is, the movement of the wind turbine blade in 1 time step was chosen as 5 deg. This is the recommended discretisation for NREL OLAF [149] and is also a widely chosen value for free vortex wake modelling. It was mentioned in section 4.2 that to limit computational expense the wake is truncated to root and tip vortices. However, this is user's choice and it can be chosen not to and just have a free wake. To ensure higher accuracy in the results, a long near wake was used which all vorticity included in the wake. The output was saved for 2 full rotations after the wake development. The small value of viscous diffusion parameter, $\delta = 7.5$ (Equation 4.20) was chosen because the simulation was performed at uniform and steady inflow conditions. The value of

$\delta = 5 - 7.5$ is also used in [148].

With this discussion, the necessary details about the set up are provided. To validate the set up, the rotor torque and thrust force were checked for against the specification values at this wind speed for the baseline wind turbine. The rotor torque was found to be +4.5% and rotor thrust was found to be +4.4%, both within acceptable limits. The next section discusses the set up and validation of the performance analysis simulations.

6.2 Aerodynamic and Structural Performance Analysis

In the previous section, the set up and validation of the simulations of the wind turbine wake using the free vortex wake method was discussed. This section discusses the simulation set up and validation for the aerodynamic and structural performance analysis of the retrofitted wind turbine in comparison to the baseline configuration. The performance analysis is focused on cut in to cut out wind speed with varying turbulence profiles, which will be shown below. All simulations were run for $660s$, with a time step of $0.005s$. The first $60s$ were considered as a transient and excluded from the calculations. Considering the required number of simulations and the computational expense of free- vortex wake modelling, the performance analysis was done with the dynamic blade element momentum theory on NREL OpenFAST [76]) and the Delft Research controller ([150]). The important parameters of the set up are discussed below and then the validation of the set up is discussed.

The inflow conditions for the performance analysis in simulations were set up in correspondence to IEC standards [151]. The inflow conditions according to normal turbulence model (NTM) and the cut in to cut out wind speeds were simulated using TurbSim [152]. The IEC NTM was used with class C turbulence characteristic. So the necessary correction to the standard blade element momentum theory were employed. The extension to the Beddoes-Leishman unsteady model by González [153] was used. The discrete-time Øye's model, with varying time constsant (τ_1) was used for the dynamic inflow correction. The Prandtl hub and tip loss correction was used. The reader is referred to [154, 100, 155] for the background information. Comparison of different dynamic stall and dynamic inflow models can be found in, for example, [156] and [157, 158] respectively. With this short discussion on the set up of performance analysis, the inflow conditions utilised are shown in Figure 6.1 below:

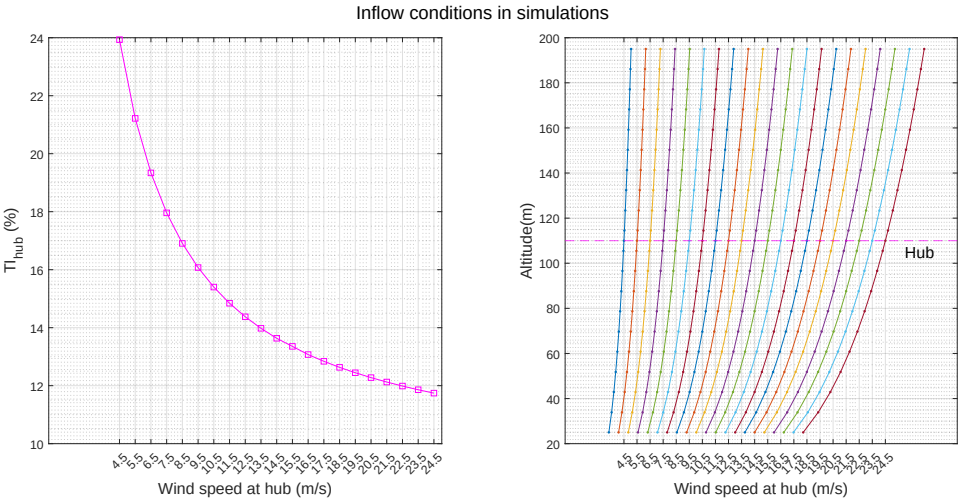

Figure 6.1: Inflow conditions in simulations

The *IEC*-Kaimal Model (as defined in [151], that has some modifications to the original Kaimal spectrum [159]) was used for the turbulence model and a power law wind profile of shear exponent as 0.2 was specified. The Delft Research Controller [150] was used for the simulations for the control of the generator, blade pitch, rotor speed through the turbulent inflow conditions. The constant torque setting was employed for the generator and individual pitch control and yaw control was disabled. A torque- speed look up table was provided with inputs from the specification sheet for the 3.8 MW research wind turbine generator.

The resulting wind turbine behaviour upon use of this controller and the inputs was validated with the measurement campaign, in which the mean values were compared. This comparison is not provided here with regards to confidentiality. As a further validation exercise, an important part of simulation result which is the temporal variation of the rotor and generator parameters is discussed. This is done for an above rated wind speed bin of $14m/s - 15m/s$ and the standard deviation statistics are compared against an equivalent period during the measurements. This is done by means of illustrating the temporal response of wind turbine rotor and generator.

The equivalent inflow during the measurement period was found by extracting a data set fulfilling the following conditions: wind direction and yaw misalignment as listed in subsection 5.3.2; hub height wind speed in the bin of $14m/s - 15m/s$ with a power law wind shear exponent $0.2 \leq \alpha_{power,exp} \leq 0.3$; hub height turbulence intensity in the bin of $11\% - 15\%$. One of such ten- minute sample is discussed here. The visualisation of the wind speed at hub height in this wind speed bin is shown below:

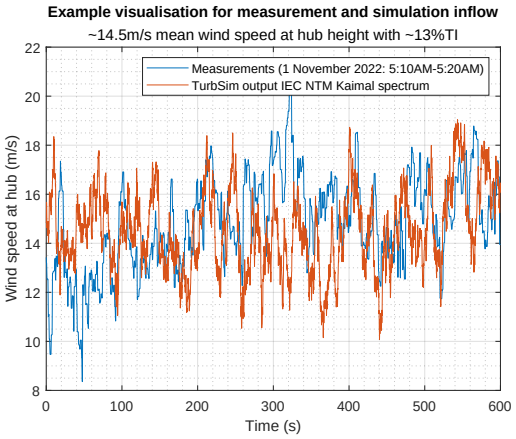

Figure 6.2: Wind speed at hub height

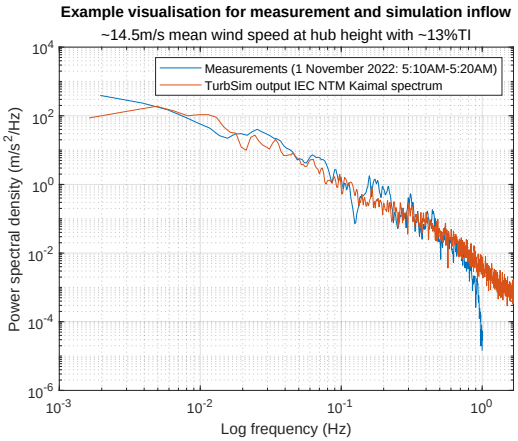

Figure 6.3: Spectral density for the wind profile at hub height

In Figure 6.2 the wind speed variation lead to a turbulence intensity of $\approx 13\%$ in both simulations and measurements. The Figure 6.3 shows the spectral density which follows from the IEC Kaimal spectrum and that obtained from the measurement period. With the data set filters discussed and one example case chosen, first, the temporal variations in the main parameters of blade pitch, rotor speed, generator speed and rotor power are compared. In Figure 6.4 below, the difference of the parameters from the mean values is shown. With respect to confidentiality, the actual values are not shown.

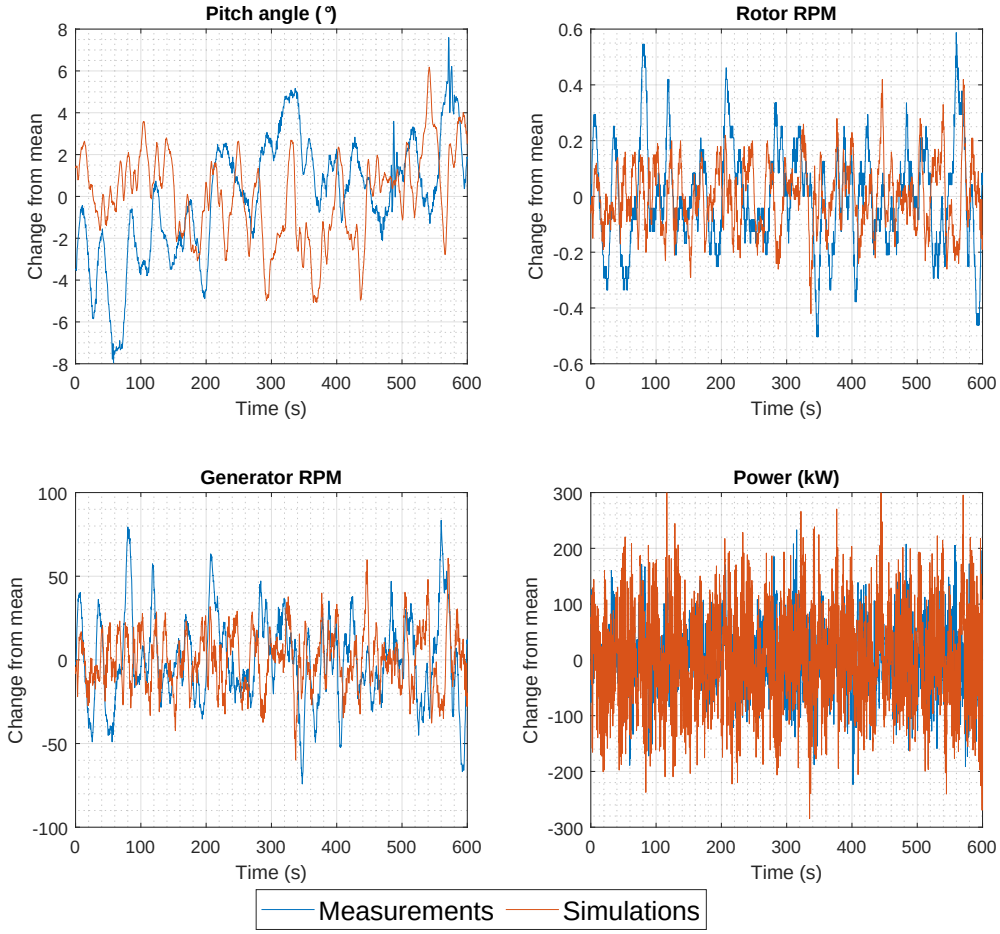

Figure 6.4: Variation of wind turbine parameters from mean value ($14m/s < U_{\infty,hub} < 15m/s$)

To thoroughly compare the wind turbine behaviour in simulation with the measurements, the standard deviation of these parameters was assessed. The standard deviation values at this wind speed bin for the measurements and the standard deviation value for the simulations are summarised below:

Parameter	**Measurements**	**Example measurement chosen**	**Simulations**
Blade pitch (deg)	$1.3 \leq \sigma_{pitch} \leq 3.3$	2.8	2.1
Rotor speed	$0.13 \leq \sigma_{Rot,RPM} \leq 0.23$	0.19	0.12
Generator speed	$18 \leq \sigma_{Gen,RPM} \leq 33$	26	17
Electrical power (kW)	$43 \leq \sigma_{P_{el}} \leq 123$	58	84

Table 6.2: Standard deviation comparison for $14m/s < U_{\infty,hub} < 15m/s$

The minimum and maximum value are shown in Table 6.2 to include all the measurements available in this wind speed bin (with the filters as mentioned above), and the example column corresponds to Figure 6.2. The comparison shows similar trend of controller behaviour in the simulation setup. With this discussion the validation of the simulation set up is provided. The next two chapters discuss the results of the field tests and the simulations, respectively.

Chapter 7

Results of Field Tests

Contents

The results of the field tests conducted for the 3.8 MW research wind turbine with and without Gurney flap are discussed in this chapter. The results are divided into two sections, first, the wake visualisation results to analyse the wind turbine wake recovery are discussed. Secondly, the results of the performance of the retro-fitted wind turbine in comparison to the base wind turbine are discussed.

It is worth noting that the retrofitted wind turbine measurement campaign was shorter than the baseline, because of noise concerns from the segmented Gurney flaps. So, as a precaution they were removed from the wind turbine after 23 days. This is reflected in the standard error of the results of the retrofitted configuration.

Note in regards to this chapter:

1. Baseline case- wind turbine without Gurney flaps or WO GF.
2. Retrofitted case- wind turbine with Gurney flaps or W GF.
3. Low TI- hub height turbulence intensity in the bin of $0-5\%$, moderate TI $5-8.5\%$ and high TI $8.5-11\%$ (in line with subsection 5.3.1).
4. The data binning was explained in subsection 5.3.1, and it was clarified that the wind direction, wind speed and turbulence intensity values of hub height were utilised for the binning. Later, the subsequent checks were performed to further investigate about need of additional filtering. These are explained in the results' discussion.

7.1 Wake Analysis in Various Inflow Conditions

The wake visualisation results correspond to the following data sets:

1. 25 November, 2022 to 24 January, 2023, for the wind turbine without Gurney flaps.
   (a) Corresponding to 59 days of data.
2. 24 January, 2023 to 14 February, 2023, for the retro-fitted wind turbine with Gurney flaps.
   (a) Corresponding to 23 days of data.

The contours are provided for the hub height, by combining the points which lie $\pm 3m$ from the hub height of $110m$, this is in accordance with the scanning LiDAR pattern (Figure 5.10). The axial and vertical profiles are provided for further insights into the wind turbine wake. Ideally these would have been plotted at the 75% span line, under the assumption that this point will correspond to the maximum lift and thus would roughly be the point of highest deficits [8, 160]. However, sometimes this point was found to lie away from the scan pattern or would coincide with the line along the nacelle which was poorly resolved by the LiDAR (for example, the spike in wind speed along the nacelle in Figure 7.3a). To avoid erroneous profiles, the 50% span was chosen and it also ensures uniformity throughout the wind speed bins. Also note that the highest deficit points would likely be different in the retrofitted wind turbine (Figure 8.1).

Only the wake comparisons using the scan pattern 2 (Table 5.2) are discussed. The reason being that the scan pattern 2 was implemented on 25 November, 2022, and from this month on the atmospheric stability effects were found to be similar up to February, 2023 (subsection 5.3.1). Scan pattern 1 which was employed in a different atmospheric stability regime was not considered for comparison of the baseline and retrofitted wind turbine wake. Also an important advantage of scan pattern 2 was the faster scan pattern, which allowed for a thorough wind field visualisation. Since the same general trends were observed in the different wind speed bins, 3 wind speed bins are discussed here and the

rest are provided in Appendix B.

The reader is also referred to some wind turbine wake field measurements in studies such as, [161, 160, 124, 162, 163, 164, 126] and a Large-eddy simulation study in [165]. The trends of wake recovery with turbulence intensity, wind shear and other atmospheric conditions as present in these studies will also become apparent in the discussion provided in this section. The different atmospheric conditions were taken care of with the data binning approach as mentioned in subsection 5.3.1; however, since the scope of this study was more towards comparing the difference in wake recovery with and without Gurney flaps than individually comparing wind turbine wake behaviour in the different atmospheric conditions, the above- mentioned studies are referred to.

7.1.1 $6m/s < U_{\infty,hub} < 7m/s$

Inflow: In this wind speed bin, there were adequate samples to provide visualisation with low and moderate TI bins for the baseline case. This is compared against the retrofitted case of low TI. Before discussing the results, a short discussion on the inflow conditions and performance parameters is provided. The corresponding inflow conditions are shown in Figure 7.1. The turbulence intensity at the lower heights was significantly higher in the retrofitted case. Owing to this difference, firstly, the turbine power production (P_{el}) and rotor rotational speed and blade pitch angle were checked for, to ensure that the wake comparison is not biased because of difference in these parameters (note that the expected power increase from installation of Gurney flaps was established in subsubsection 3.4.1.1. The check was done to ensure unexpectedly high variations). It was found that between the baseline case and retrofitted case of low TI, the P_{el} differed by only 3.5%; attributed mainly to the addition of Gurney flaps (also seen in Figure 7.14). The RPM was found to vary only by 0.7%.

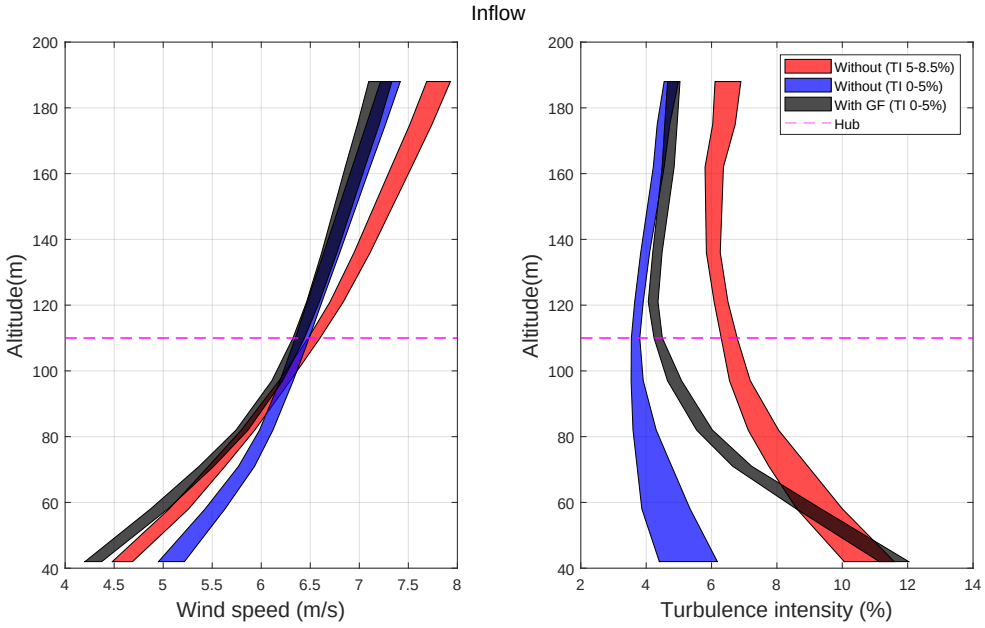

Figure 7.1: Inflow profile ($6m/s < U_{\infty,hub} < 7m/s$)

CNR Check: In this wind speed bin, an anomaly in hub height contour was found. So a further investigation was done into the reason behind it. This check is provided here, following which the result is provided. Figure 7.3c reveals a distinct patch after $1D$ downstream (as indicated by the region in the black outline). Specially, very low free stream wind speeds are seen. After the data binning, the checks on wind turbine operational parameters there was no anomaly in the data set. Apart from these, one factor which can help explain this patch is the scanning LiDAR data CNR (see section 5.2). The filtering was explained and the unreliable data was first filtered directly by the scanning LiDAR algorithm as mentioned in step 1 of subsection 5.2.1. Secondly, an additional carrier to noise ratio filter was employed. The reason for this patch is likely due to a heavy fog condition during this particular timestamp (also see [112, 113]). However it appears that this was not filtered

out by the steps mentioned. Figure 7.2 shows the variation of CNR in the 2 cases. From Figure 7.2c it becomes clear that the less negative CNR values upto $1.5 - 2D$ downstream are giving valid free stream conditions as also evident in Figure 7.3c upto $1D$ downstream free stream region. Further downstream, the values seem to be reduced, not in reality but possibly due to the back scatter in the foggy conditions. If one has access to the backscatter coefficient for the scans, it may be checked and compared with other scans to check which value can be deemed to relate with a foggy condition. Apart from this and a visual check, other evidence about a foggy condition can be gathered by analysing (including, but not limited to) parameters such as dew point difference from the actual temperature through the day, the relative humidity and vapor pressure. Such a comparison is provided in Figure B.1 which reveals favourable conditions for fog. The patch marked with black lines in Figure 7.3c seems to correspond well with the varying CNR values. The CNR is linearly proportional to the back scatter and inversely proportional to the square of the propagation distance (notice the smooth gradient in Figure 7.2a). The histograms shown also indicate the difference in the distribution of CNR values. The bin averaged data standard error of the retrofitted case radial wind speed was checked, but was found to be within $\pm 0.3 m/s$. It is difficult to determine a precise carrier to noise ratio threshold for each condition, thus a constant CNR threshold value was used in this study, as listed in subsection 5.2.1, as the best choice to keep the comparison unbiased.

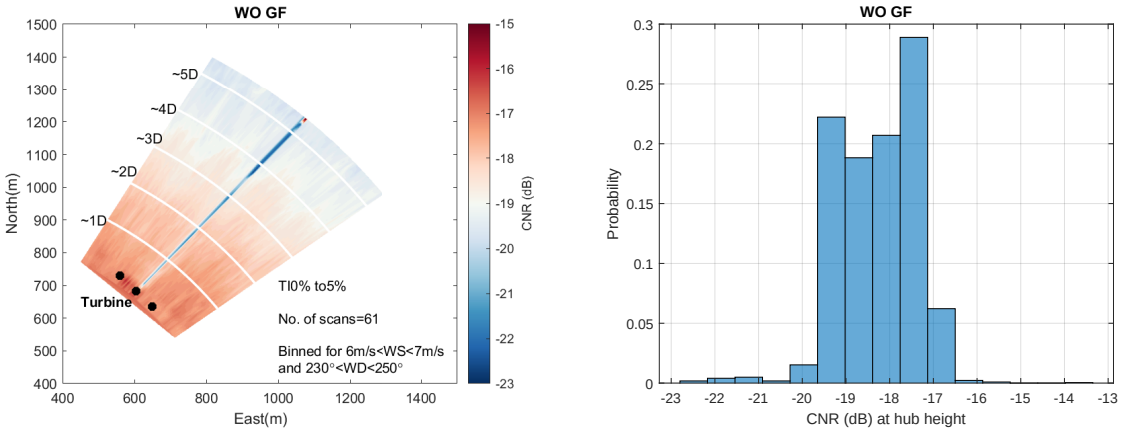

(a) WO GF Low TI

(b) WO GF Low TI

Figure 7.2: CNR visualisation ($6m/s < U_{\infty,hub} < 7m/s$)

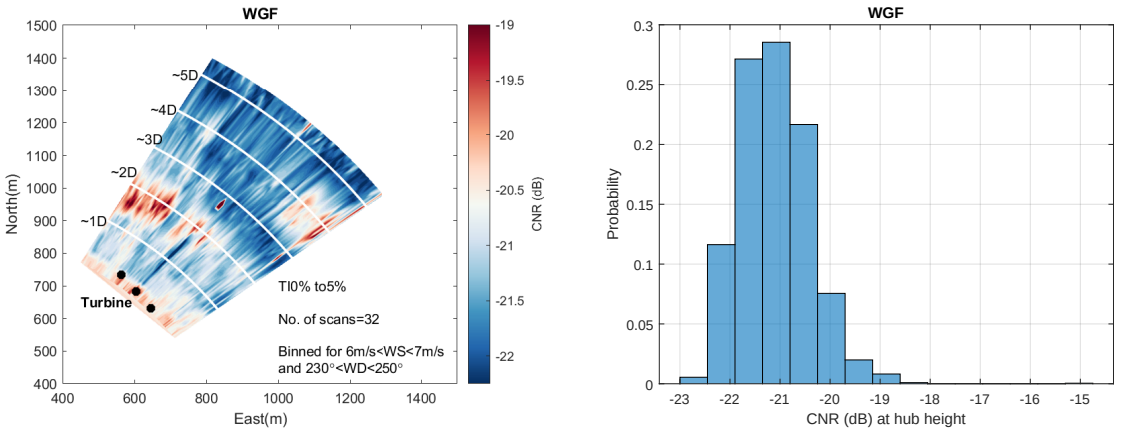

(c) W GF Low TI

(d) W GF Low TI

Figure 7.2: CNR visualisation ($6m/s < U_{\infty,hub} < 7m/s$)

Hub height contour: With the CNR check discussed, it appears that the values further downstream are of reduced magnitude, but with a low standard error. In light of this discussion, it can be stated that for this wind speed bin case, particularly downstream the reliability of data is questioned and could be underestimated when comparing the free stream conditions. Nevertheless, in proximity to the rotor, upto $1D$ downstream, it can be seen that the there is an indication of faster wake recovery.

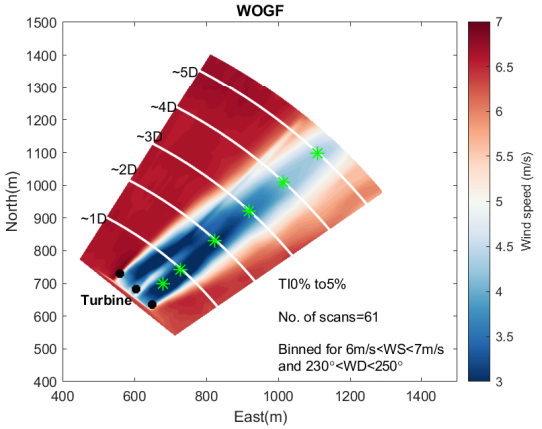

(a) WO GF Low TI

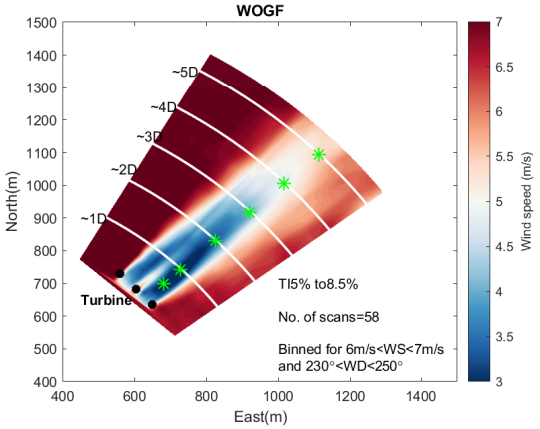

(b) WO GF Moderate TI

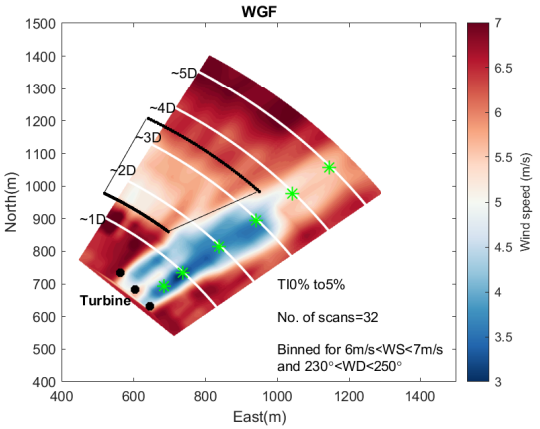

(c) W GF Low TI

Figure 7.3: Wake visualisation ($6m/s < U_{\infty,hub} < 7m/s$)

Axial profiles: The normalised deficit profiles at different heights are shown in Figure 7.4. It can be seen that with higher turbulence intensity faster wake recovery is achieved. This is expected specially further downstream when the ambient turbulence plays a key role in the wake breakdown. Thus, up to $2D$ downstream there is not an indication of difference in wake recovery between baseline low and moderate TI case. However, it is interesting to note that in this region, the retrofitted case is enhancing the wake mixing and a consistent decrease in deficit is observed. The sharp drop in deficit in the retrofitted case in Figure 7.4c is more clearly observed with the wake visualisation at hub height by means of contour provided above.

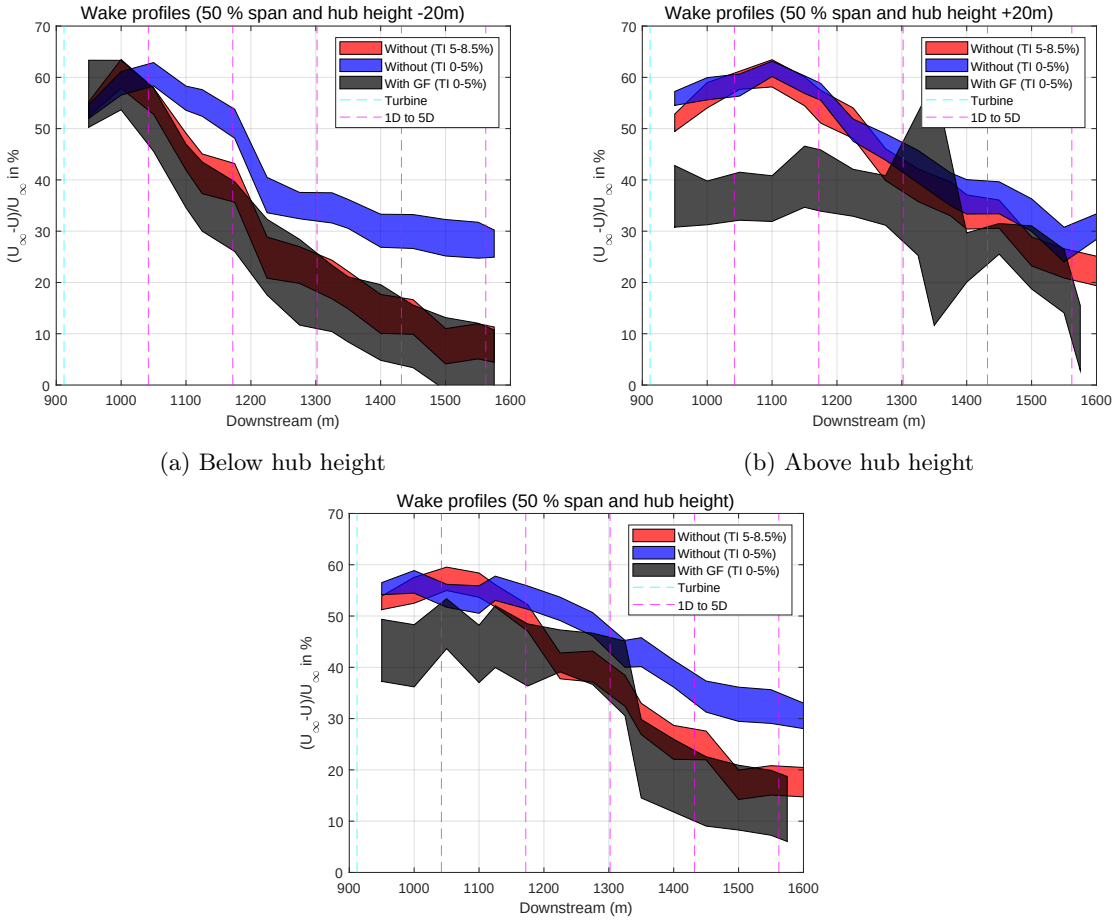

(a) Below hub height

(b) Above hub height

(c) Hub height

Figure 7.4: Axial wake profile (Normalised with U_∞ at the respective altitudes) $(6m/s < U_{\infty,hub} < 7m/s)$

Vertical profiles: There is an indication of a steep slope (higher difference in the maximum and minimum wind speeds) in the retrofitted case wind speed, particularly, at $1D$ downstream. The typical Gaussian and double Gaussian wake profiles can roughly be observed in Figure 7.5. For example, baseline case low TI at $4D$ downstream and retrofitted case at $2D$ downstream, respectively. At all distances downstream there is a general trend for increase in velocity in the retrofitted case. This also seems to be the case when comparing the retrofitted case of low TI to the baseline case of moderate TI. The observations indicate faster wake recovery in the retrofitted case, with some uncertainty in regards to the CNR values observed in this case.

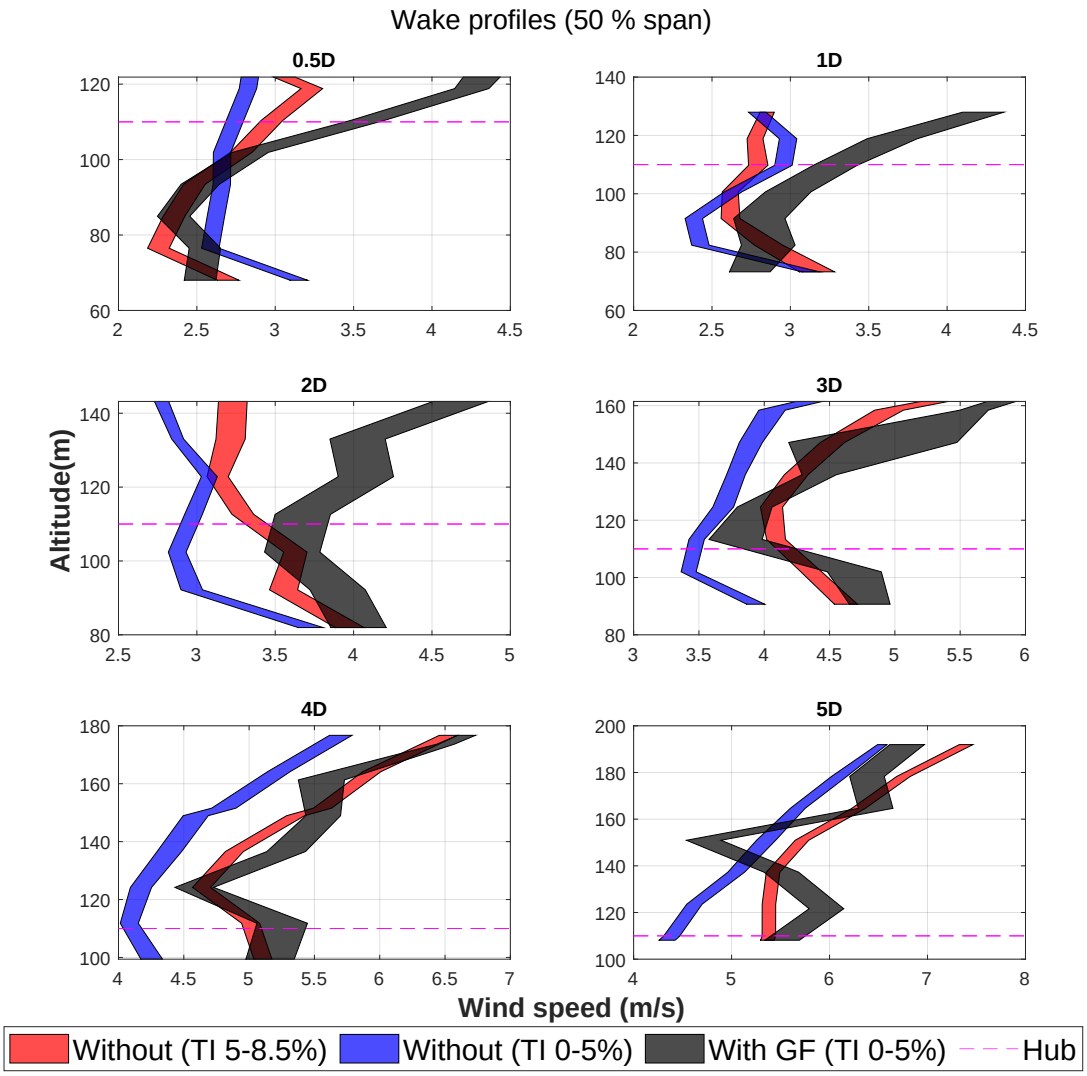

Figure 7.5: Vertical profile ($6m/s < U_{\infty,hub} < 7m/s$)

7.1.2 $8m/s < U_{\infty,hub} < 9m/s$

Inflow: The inflow conditions for this wind speed bin are provided in Figure 7.6, which corresponds to high TI. It was seen that the retrofitted case had slightly higher wind speed and turbulence intensity levels. However, the wind speed difference is around only $0.5m/s$, within the bin width, and turbulence intensity levels around 2%. However, in this wind speed bin, upon checking the P_{el} and RPM and blade pitch angle, it was found that the step 6 mentioned in subsection 5.3.1 was indeed necessary. For one of the samples, the P_{el} was found to be 15% more in the retrofitted case (which seems unlikely to be attributed to the addition of Gurney flaps) and the blade pitch was found to be 30% more in the retrofitted case. This is shown in Figure B.6. The rotor speed can be seen to stay almost constant around rated speed despite the lower than rated wind speeds; which is reflected in the difference of power from the expected value at this wind speed. The effect of pitch on the wake recovery was discussed in section 3.1 and section 3.3. This outlier was filtered out and the post-processing was redone. While this does not affect the validity of the results shown, it is stated here to realise the importance of the data- binning approach and subsequent checks.

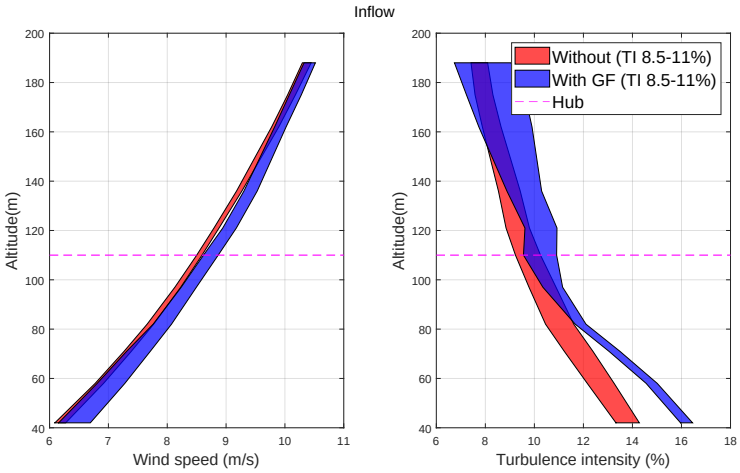

Figure 7.6: Inflow profile ($8m/s < U_{\infty,hub} < 9m/s$)

Hub height contour: Here it should be noted that the number of scans in the retrofitted case is 19, that is, 19 scans in the relevant bins were averaged to make this contour while in baseline case there were 96 scans. As mentioned in Figure 5.10, one scan corresponds to about 3 minutes and thus every ten minute interval, 3 samples of wind speed. In the contours in Figure 7.7 there is not a very sharp indication of the difference in the wind speeds, a thinner wake (after $3D$ downstream) for the retrofitted case is seen, but it unclear whether it can be attributed to the addition of segmented Gurney flaps; because this observation is not consistent in all wind speed bins. The discussion will be aided by the axial and vertical profiles shown next.

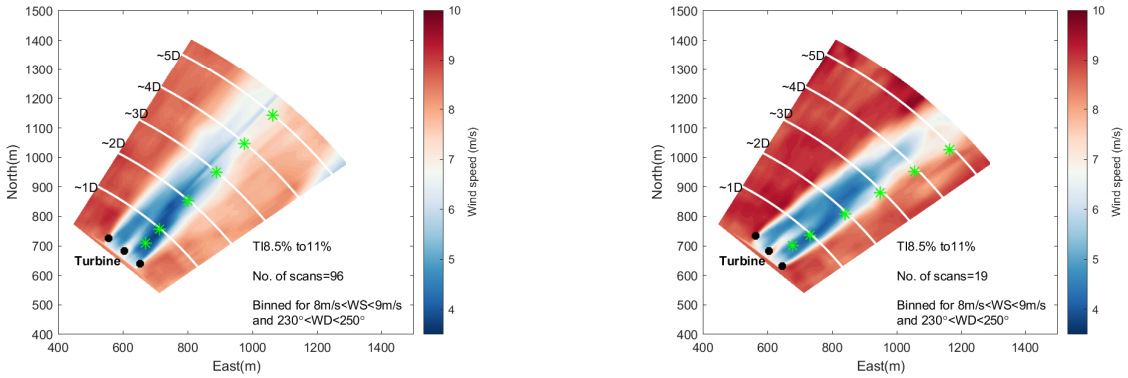

(a) WO GF High TI

(b) W GF High TI

Figure 7.7: Wake visualisation ($8m/s < U_{\infty,hub} < 9m/s$)

Axial profiles: The normalised deficit profiles indicate a faster recovery in the retrofitted case at the different altitudes, shown in Figure 7.8. In this wind speed bin there were not adequate samples to provide wake visualisation at other than high TI bins. The peaks for the deficit appear around $1D$ downstream after which both cases show recovery.

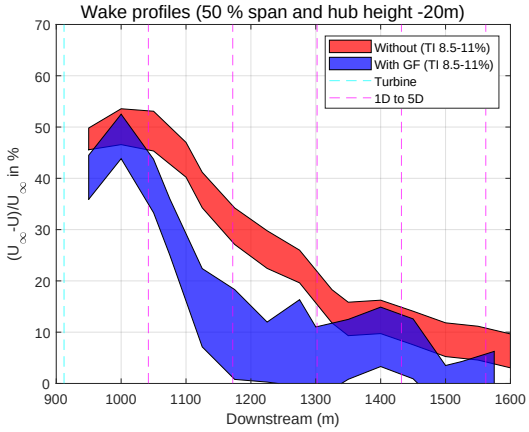

(a) Below hub height

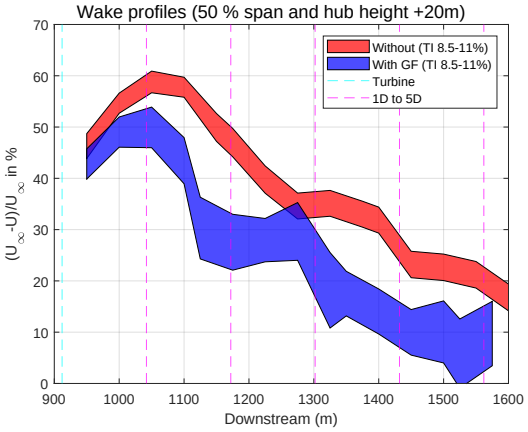

(b) Above hub height

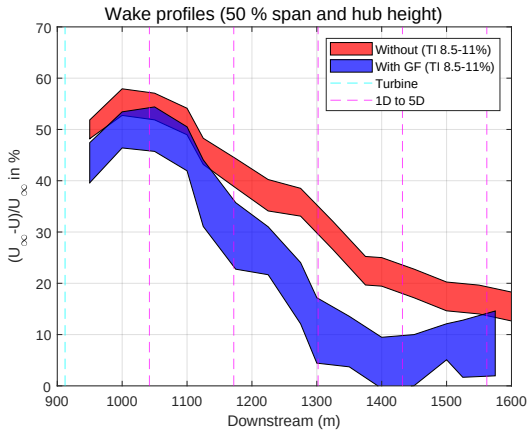

(c) Hub height

Figure 7.8: Axial wake profile (Normalised with U_∞ at the respective altitudes)$(8m/s < U_{\infty,hub} < 9m/s)$

Vertical profiles: Here it is interesting to see a clear increase in wind speed at every downstream distance. Once again, the double Gaussian wake profile can be observed generally. It can also be seen that upto $1D$ downstream, the wake profile of the baseline case and retrofitted case are quite similar with the retrofitted having increased wind speed throughout. The steep slope in the wind speed is also evident $1D$ downstream, for the retrofitted case, which was also seen for the $6-7m/s$ wind speed bin. After that, the wake profiles are different but clearly increased wind speed upto $5D$ downstream.

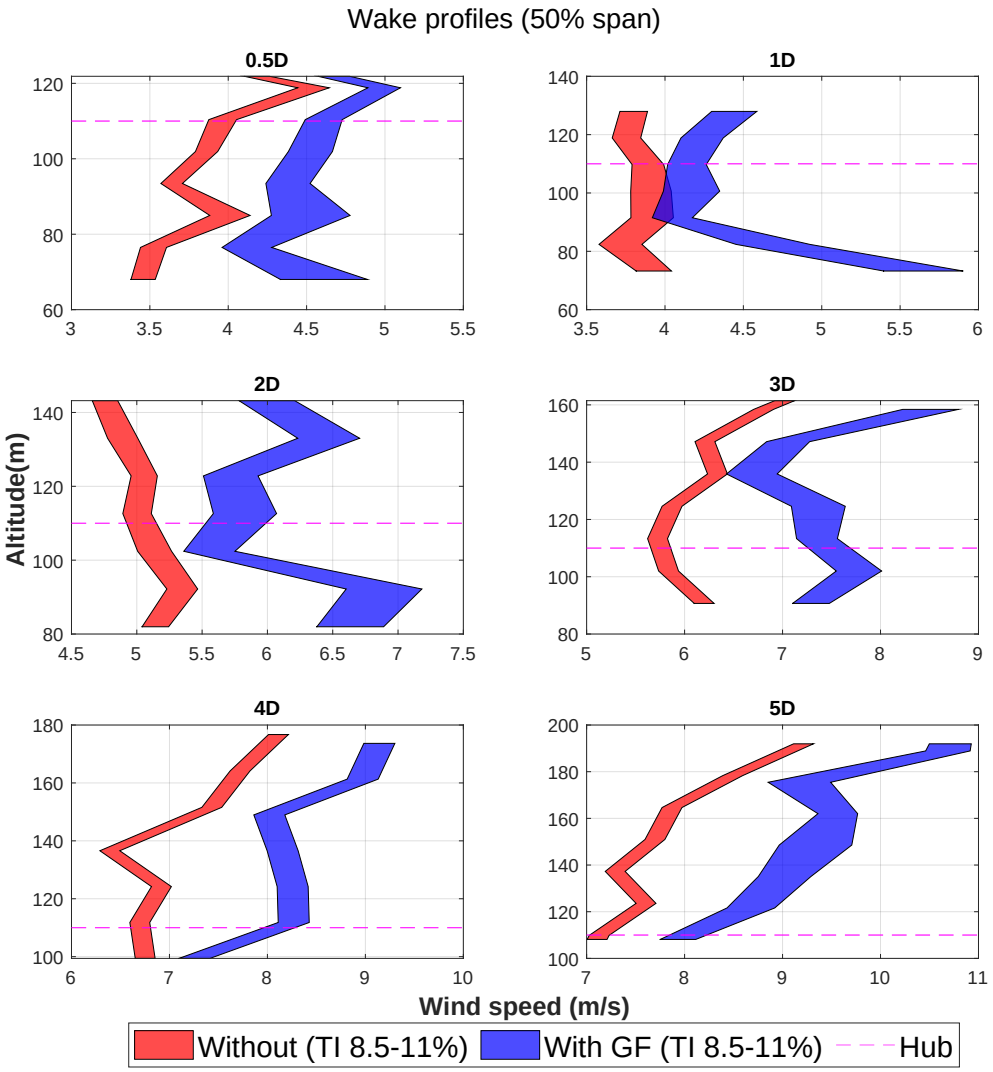

Figure 7.9: Vertical profile ($8m/s < U_{\infty,hub} < 9m/s$)

7.1.3 $10m/s < U_{\infty,hub} < 11m/s$

Inflow: The inflow conditions for this wind speed bin are provided in Figure 7.10, which correspond to high TI. The wind speed and turbulence difference are within the bin width for both the cases, but a slightly higher value of turbulence is evident for the retrofitted case. Upon checking the P_{el}, RPM and blade pitch, 6% increased power production was obtained for the retrofitted case, partly attributed to the slightly higher wind speed and mainly attributed to the Gurney flaps. This power increase could possibly have a negative effect on retrofitted case wake recovery, because the wind turbine extracted more energy from the incoming wind.

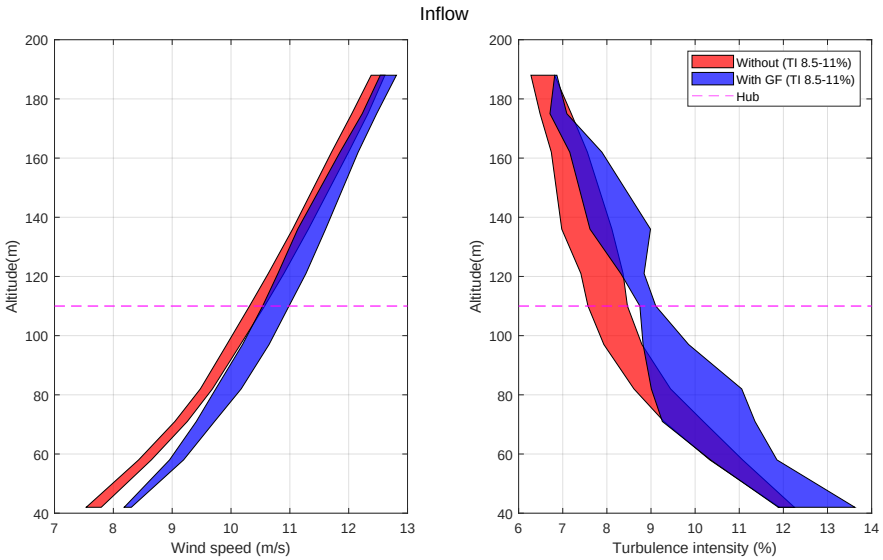

Figure 7.10: Inflow profile ($10m/s < U_{\infty,hub} < 11m/s$)

Hub height contour: Here, it is important to note the longer wake (low wind speed regions throughout the scan up to $\approx 5D$ downstream), particularly for the baseline case. This is mainly due to the low tip speed ratio at this wind speed; the exact numbers are not mentioned in regards to confidentiality. The effect of tip speed ratio on the wake was discussed in subsection 2.2.2. In the previous low wind speed wake visualisations, such a long wake was not evident from the hub height contours. Thus, as per expectations, the effect of Gurney flaps should indeed be more pronounced in this wind speed which is also evident from the axial and vertical profiles shown next.

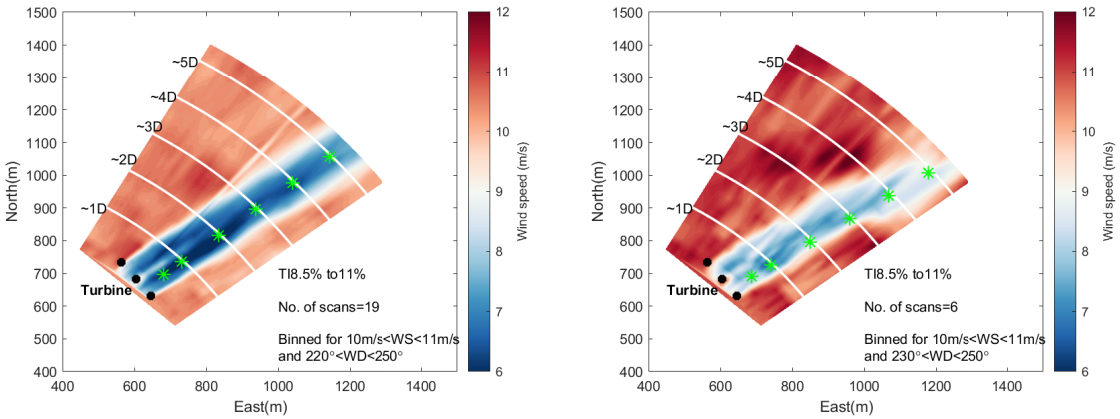

(a) WO GF High TI

(b) W GF High TI

Figure 7.11: Wake visualisation at high turbulence intensity ($10m/s < U_{\infty,hub} < 11m/s$)

Axial profiles: The normalised deficit profiles are shown in Figure 7.12. A consistent decrease in wind speed deficit is seen at all 3 heights. A higher standard error is observed for the retrofitted case which is due to the less number of scans available. The retrofitted case had only 6 scans averaged as shown in Figure 7.11b.

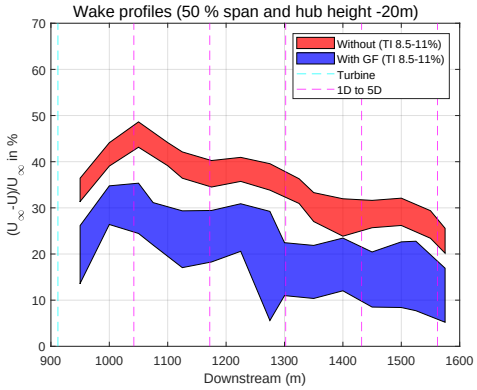

(a) Below hub height

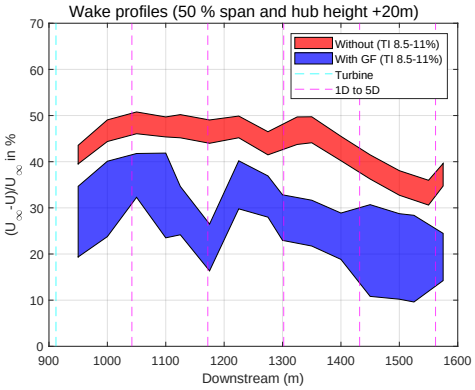

(b) Above hub height

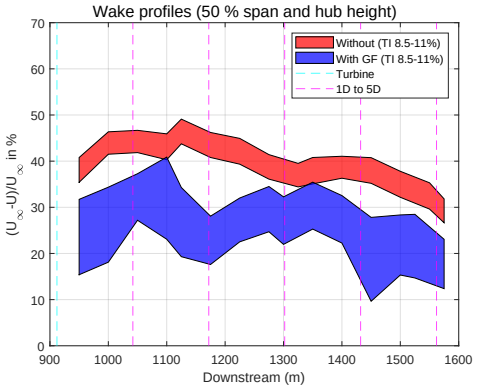

(c) Hub height

Figure 7.12: Axial wake profile (Normalised with U_∞ at the respective altitudes) $(10m/s < U_{\infty,hub} < 11m/s)$

Vertical profiles: The Gurney flaps are proving to be effective in wake recovery at all downstream distances. This wind speed bin appears to be the most important in terms of the effect of Gurney flaps, so it was tested in simulations as well (section 8.1).

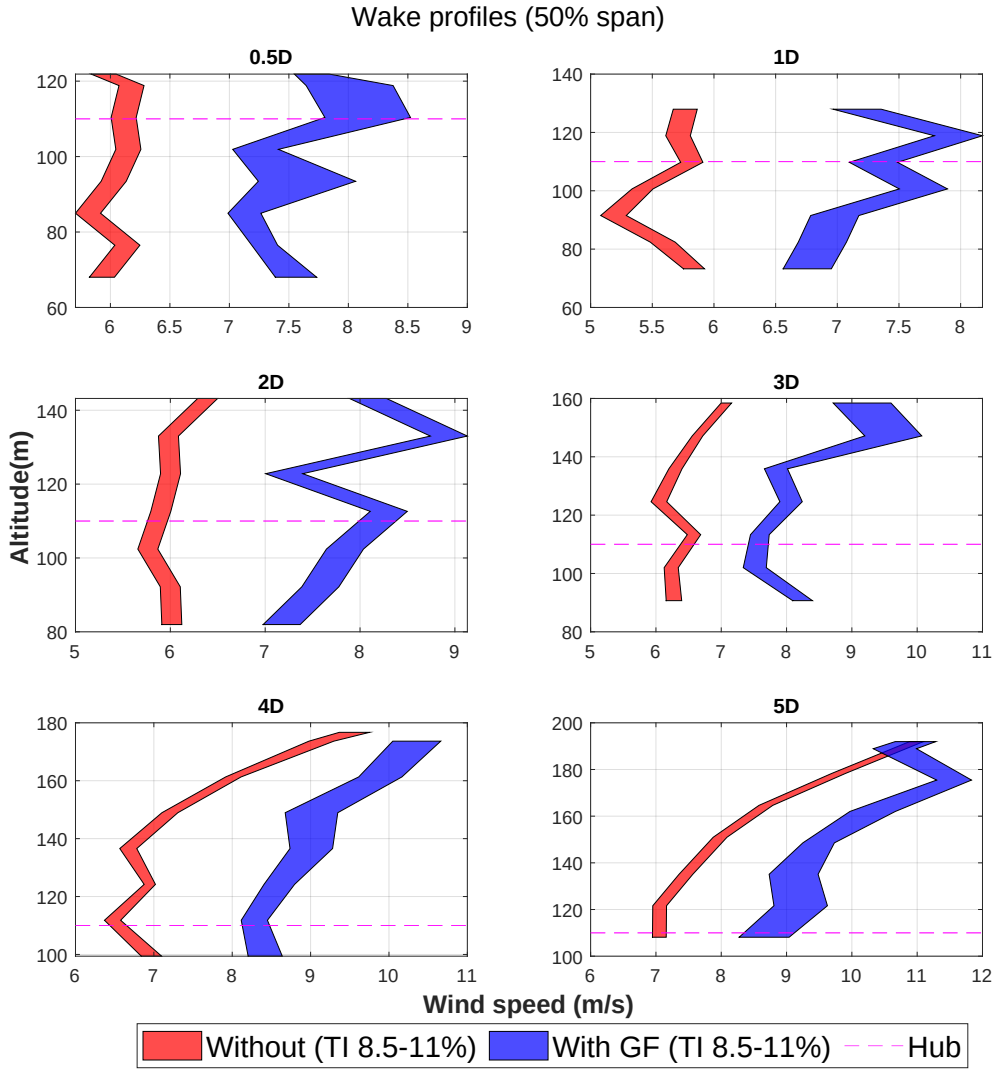

Figure 7.13: Vertical profile ($10m/s < U_{\infty,hub} < 11m/s$)

Some more general discussion on the field tests' wake study is provided next. Following that, the performance analysis of the retrofitted wind turbine configuration is discussed.

7.1.4 Overall Observations

Overall the field tests provided a lot of insights to the wind turbine wake. The thorough binning procedure coupled with subsequent checks to the data sets analysed was used to ensure an unbiased comparison as best as possible. To account for the changing wind shear and turbulence intensities within the bin averaged data, the lower wind speed bins had the retrofitted case compared with baseline case of two TI bins. The results indicate consistently observed faster wake recovery in the retrofitted configuration (generally at all downstream distances), with a higher standard error because of the shorter testing time.

The typical double Gaussian and single Gaussian wake profiles were observed in the field tests' wake study. The faster wake recovery with increasing turbulence was observed, as also stipulated in [164, 162]. The velocity deficit profiles were in line with previous studies as indicated in the start of this chapter. Particularly in [160] it was found that the observations indicate an initial velocity deficit of $50\% - 60\%$ immediately behind the turbine, which gradually declines to $15\% - 25\%$ at a downwind distance of $6.5D$. This is also observed in the field measurements in this study. The increase velocity deficit in close proximity to the rotor (observed throughout, but, for example, in Figure 7.12) is expected because of the relaxation of radial and stream-wise pressure gradients. This appears roughly upto $1D$ downstream, as also seen in [166, 167]. Highest deficits were observed for lower wind speed cases which are related to the variation in the turbine thrust coefficient [168].

With the increase in wind speeds the effect of Gurney flaps was expected to be higher, owing to the more stable baseline wake, in line with subsection 2.2.2. This was found to be the case during the field tests as well, with a certain compromise on the number of scans available. Furthermore, it is interesting to note that, at times, up to $2D$ downstream, the wake profile was very similar in both cases (for example, Figure 7.9) with increased wind speeds for the retrofitted case. Overall, the effect of Gurney flaps was clearly observed with the field tests, but with higher than baseline standard errors. The $0.5D - 2D$ downstream region also showed increased wake recovery, in line with subsubsection 3.4.1.2, suggesting indeed the interaction of additional vortices shed from the edges of each Gurney flap along with an increase in turbulence in the wake. In some wind speed bins, the retrofitted case was found to be performing better in terms of wake recovery also in comparison to the baseline case with higher TI bins, which indicates this increase in turbulence upon addition of the segmented Gurney flaps. However, this added turbulence could not be quantified in the field tests; there are recommendations in regards to this, listed in section 9.2. Lastly, since only 1 scanning LiDAR was utilised, the increase in tangential components (as found in literature) could not be reliably measured. The next section discusses the performance analysis by the field measurements.

7.2 Aerodynamic and Structural Performance Analysis

In the previous section, the effect of segmented Gurney flaps on the wind turbine wake was discussed. In this section, performance parameters are discussed to investigate the effect of segmented Gurney flaps on the retrofitted wind turbine. As mentioned in the start of this chapter, the duration of the data-set for the retro-fitted wind turbine with Gurney flaps is shorter than the one for the baseline wind turbine. Thus, it should be noted that certain differences in the result analysis can be present due to poor averaging of the sample points, which usually is reflected in the standard errors indicated. The performance analysis results discussed in this chapter correspond to the following data sets:

1. 1 September, 2022 to 23 January, 2023, for wind turbine without Gurney flaps.
   (a) Corresponding to 144 days of data.
2. 24 January, 2023 to 14 February, 2023, for the retro-fitted wind turbine with Gurney flaps.
   (a) Corresponding to 23 days of data.

The resulting statistics for the samples which fulfill the requirements listed in subsection 5.3.2 are discussed here. The plots are made with the $x - axis$ points lying on the bin centre. The ticks on the axes are not shown in regards to confidentiality. Firstly, the power coefficient, C_p was assessed, as follows from the equation:

$$C_p = \frac{P_{el}}{\frac{1}{2}\rho\pi R^2 U_\infty^3} \tag{7.1}$$

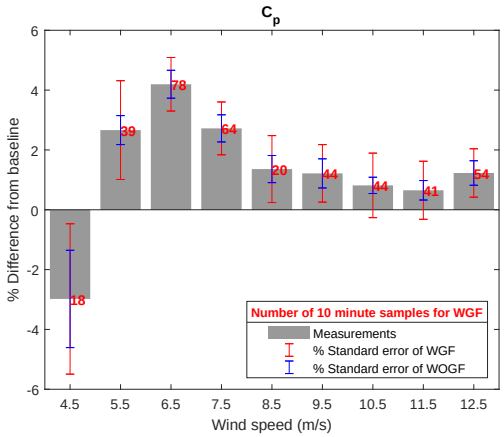

Figure 7.14: Power coefficient comparison

As expected from the increase in lift coefficient because of Gurney flaps, the increase in torque leads to increased power production up to rated wind speed. Above rated wind speed, generally speaking, the controller will pitch the blade more to curtail power, so it is not included in the comparison. The plot of power coefficient with standard error is not shown because of confidentiality. Instead, the standard error of the retrofitted case, as a percentage of the value of C_p is plotted. At the first 2 wind speed bins, a very high standard error is seen in the retrofitted case. So, the decrease in C_p in Figure 7.14 may not be fully representative of the effect of segmented Gurney flaps. Furthermore, it is clear that the standard error is very high to make conclusive arguments about the C_p increase. Next, the blade flap-wise bending moment was compared as shown below:

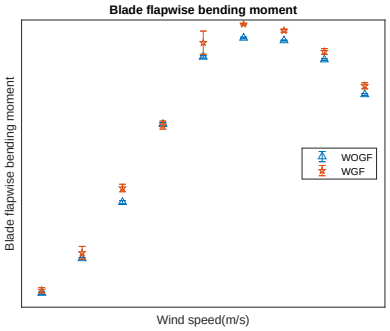

(a) Average with standard error

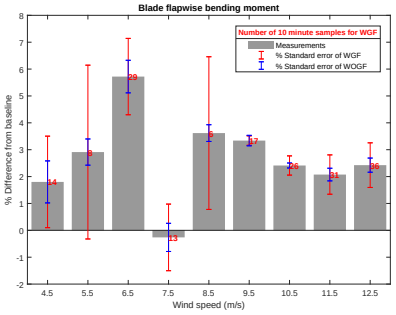

(b) Relative difference

Figure 7.15: Blade flap-wise bending moment comparison

Once again in line with increased rotor torque expectations, a general increase in blade flapwise bending moment is observed. The decrease in flapwise bending moment observed in the $7-8m/s$ bin was checked for and it was found that the samples available for the retrofitted case had an average wind speed lower by $0.4m/s$ from the baseline. The very high standard error for the $5m/s-6m/s$ bin also gets reflected in the very high change in tower fore aft bending moment shown below:

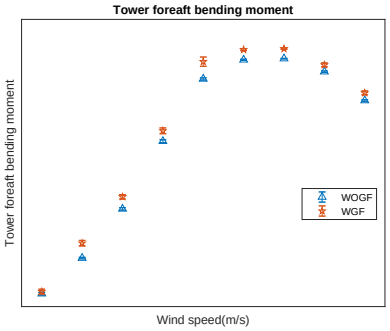

(a) Average with standard error

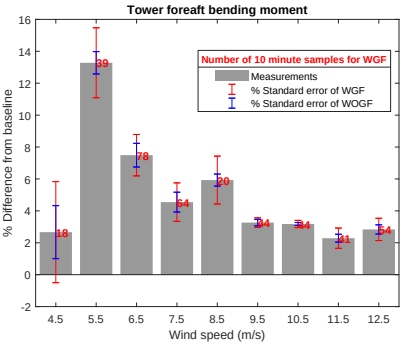

(b) Relative difference

Figure 7.16: Tower Fore-aft bending moment comparison

This wind speed bin data was checked and the reason behind the anomaly seen in the above 2 plots was found to be attributed to different distributions of the pitch and rotor speed values. This coupled with less samples, lead to some outliers being not averaged adequately. As indicated on the plot, the flapwise bending moment signal (and tower fore aft bending moment) for retrofitted configuration had only 8 (and 39) samples while the baseline configuration had 257 (and 268) samples. Similar observation was seen for the higher standard error in the $8m/s-9m/s$ bin in Figure 7.15. Because of such anomalies, the limited data for the performance analysis does not allow for conclusive arguments for the observed differences and the trend. To tackle this issue, there is extension of the performance analysis by means of simulations. The next chapter discusses the results of simulations.

Chapter 8

Results of Simulations

Contents

NREL OLAF was used for the wake analysis and DBEMT (BEM for dynamic inflow conditions) on NREL OpenFAST with the Delft research controller ([150]) was used for the aerodynamic and structural performance analysis. The set up and validation of the simulation environment was explained in chapter 6. In this chapter, the wake and performance analysis results in the simulation environment are discussed in the respective sections.

8.1 Wake Analysis in Steady and Uniform Inflow Conditions

One of the main motivation behind utilising segmented Gurney flaps was to alter the lift distribution along the blade. This was to get the spatial variation in the circulation. In Figure 5.5 and Figure 5.6b the positioning of the Gurney flaps on the wind turbine blade was discussed. With the use of these segmented Gurney flaps, the spatial variation is enhanced because of the significant increase in the lift coefficient in comparison to the neighbouring elements. This can be seen in the normal force (to chord) variation shown in Figure 8.1 below, where 'W GF' represents the retrofitted configuration:

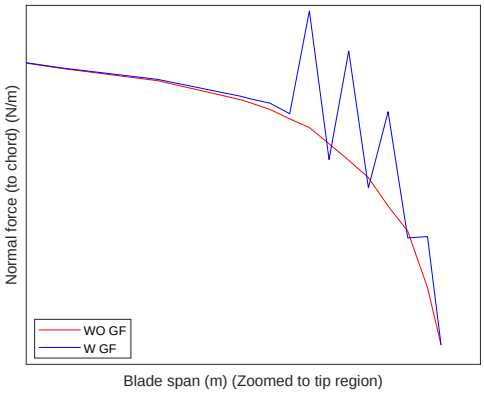

Figure 8.1: Normal force (to chord) comparison

Figure 8.2: Circulation comparison

In the figures above, the jagged lift and circulation distribution along the blade span are illustrated. It is also desired to not change the overall loading on the rotor blade to ensure minimal structural downsides. The integral of the normal force (to chord) curve resulted in only about an $\approx 1\%$ increase for the retrofitted configuration in this inflow condition. The effect of the changing circulation is on the shed vorticity, as evident below, where the lower plot labelled 'W GF' represents the retrofitted configuration:

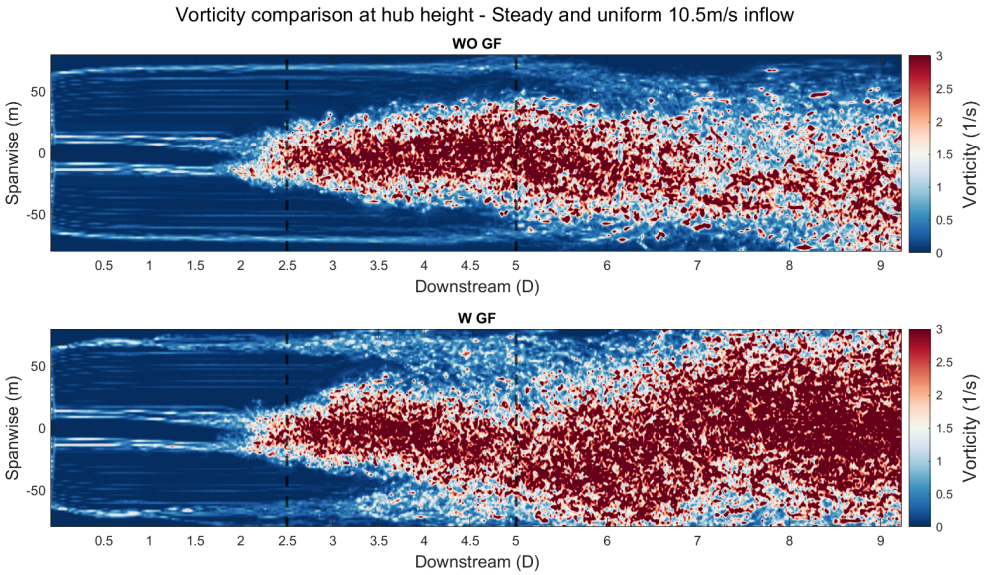

Figure 8.3: Wake mean vorticity visualisation at hub height $110m$

Figure 8.3 illustrates the mean vorticity at hub height, the mean which was calculated for 2 full rotations. Both the simulations have the same regularisation parameter and span wise spacing values. The only difference is the change in the airfoil polar data for the retrofitted case. The effect of former is evident from the similar discrete lines of mean vorticity up to the tip region and by the same distortion of the root vortices along the centre line. The effect of the latter becomes evident in the tip region which involve the different airfoil polars. It is evident the the retrofitted configuration has significant disturbances in the rotor tip region, from roughly $2.5D$ downstream. While for the baseline configuration such significant disturbance is seen only after $5D$ downstream. This faster (earlier) mutual interaction of the tip vortices provides validation for one of the reasons behind the faster wake recovery by segmented Gurney flaps in the field tests, specially in farther downstream distances. The field test results also indicate the faster wake recovery in proximity to the rotor. This could not be validated in the simulations because the actual Gurney flap was not resolved in the simulations, and only the airfoil polars were changed. This validation may be made possible by longer field tests or blade resolved simulations. In line with this, recommendations are listed in section 9.2.

Apart from this visual check, the formulation presented by the authors in [169] may be used in case of a turbulent inflow. They present a semi empirical model to predict the stable wake length of a wind turbine wake in different inflow turbulence conditions. In [170] the constants to the model are calibrated. They conduct simulations under turbulence intensities of 0.1%, 3% and 8.8% with the wind turbine operating at the optimal point. However, in the free vortex simulations presented in Figure 8.3 the inflow was steady and thus the above mentioned equation cannot be used to get the physical representation of the tip vortex breakdown location. But it is mentioned here as it can be a useful formulation for the interested reader.

8.2 Aerodynamic and Structural Performance Analysis in Various Inflow Conditions

In this section, the results are discussed in regards to the rotor properties. The impacts on rotor thrust, power, flap-wise bending moment are discussed. An annual energy production estimation is done and lastly, the results of a fatigue analysis conducted in terms of the damage equivalent load formulation are discussed.

The rotor performance upon addition of the Gurney flaps on the blade tip will mainly be affected by the change in lift distribution achieved (apart from 3-D boundary layer effects). This change is affected mainly by the lift and drag characteristics in that blade region, which depends on the angle

of attack at these positions. In Figure 5.5 and Figure 5.6b the positioning of the Gurney flaps on the wind turbine blade was discussed. To realise the changing lift characteristics, here the mean angle of attack comparison during the simulations with the inflow shown in Figure 6.1 was analysed. The exact values are not shown here with regards to confidentiality. The angle of attack ranged from roughly 2 deg to 0 deg for $4 - 10m/s$ wind speed range and then decreasing to roughly -8 deg to -12 deg for $24 - 25m/s$ wind speed range. The range of angle of attack follows for the spanwise positions corresponding to the Gurney flap 1 to 4. A plot indicating the change in angle of attack due to the Gurney flaps is shown below:

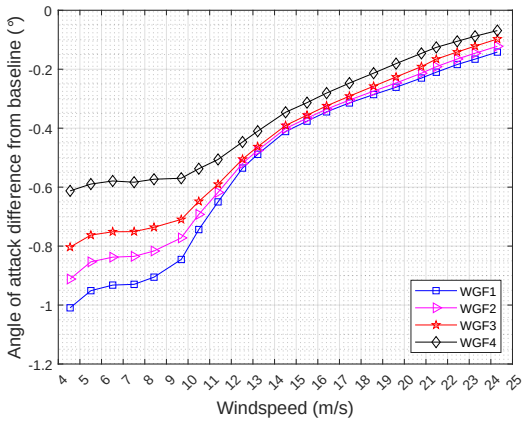

(a) Difference from baseline (at Gurney flap positions)

Figure 8.4: Angle of attack at different wind speeds at regions near blade tip

In Figure 8.4 the $WGF1$ to $WGF4$ correspond to the angle of attack at the position of the 4 Gurney flaps (Figure 5.6b); and $WOGF1$ and $WOGF2$ correspond to the positions adjacent to the first Gurney flap. With Figure 8.4a, it can be seen that the Gurney flaps cause a reduction in the angle of attack. This is because of the higher downwash associated with the Gurney flaps and the resulting induced drag effect. The last position, that is, $WGF4$ has significant changes in the angle of attack in comparison to the position without Gurney flap. This change can sometimes work in the direction of increasing lift while sometimes increasing drag but reducing lift. The corresponding changes in the airfoil parameters can be visualised by the example visualisation in Figure 3.6 provided by means of a literature study. This distinction is provided to help correspond to the required points on the airfoil performance curves. With the literature provided it can be said that the effect of Gurney flaps on lift coefficient is evident in the angle of attack range of ≈ -8 deg to ≈ 12 deg. Thus, at very high wind speeds the effect of Gurney flaps will be evident in terms of drag but not in terms of lift.

As mentioned about the change in lift distribution, in Figure 8.1 the change in normal force (to chord) was shown for one wind speed bin. Here a plot indicating the difference in the area under the normal force (to chord) curve for all wind speed bins is shown:

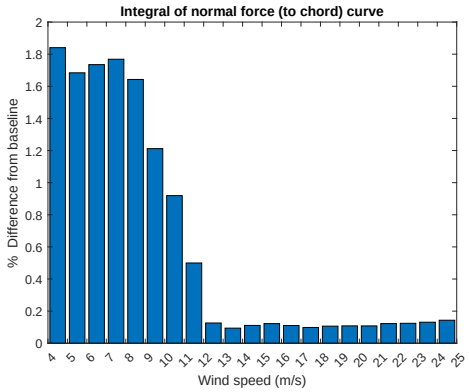

Figure 8.5: Normal force integral comparison at different wind speeds

This clarification on the operating angle of attack for the wind turbine blade tip and the corresponding change to the effective lift distribution on the wind turbine blade, forms the basis of the performance results. The below figure show the rotor thrust and power comparison:

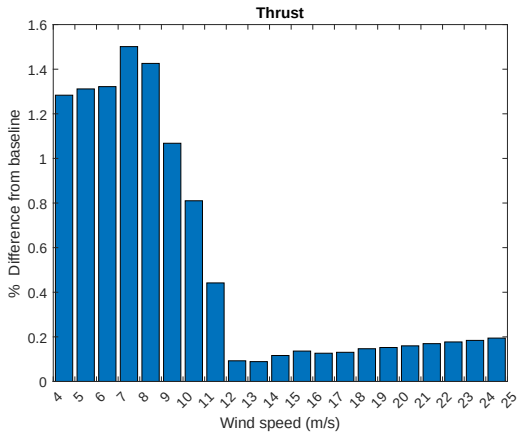

Figure 8.6: Rotor thrust comparison

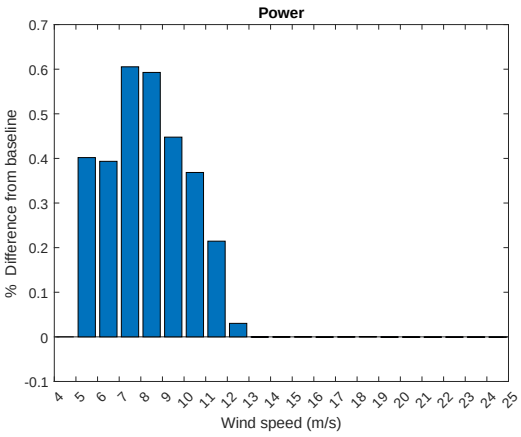

Figure 8.7: Rotor power comparison

In Figure 8.6 the trend of increase in the rotor thrust at all wind speeds is evident. As the normal force (to chord) is nearly an out of plane force just like the thrust force, the trend of increase in thrust force is similar to that shown in Figure 8.5. For a wind turbine, up to rated wind speed, the thrust force increases, after which it decreases as the wind turbine power remains constant. So above $11m/s - 12m/s$ bin, the increase in thrust force is not that high from the baseline case. These trends also follow from the effective change in the lift distribution brought about by the Gurney flaps and the difference in angle of attack. The higher increase up to $8m/s - 9m/s$ is explained by the angle of attack curve shown in Figure 8.4. The same behaviour is reflected in the power difference as well.

Furthermore, in regards to power difference, it is seen that the increase in power is not as high as found in the field tests (Figure 7.14). As mentioned before, for the field tests' retrofitted wind turbine performance analysis, a broad turbulence intensity and shear exponent range was used because of limited data availability. This leads to certain bias in the differences in the field tests' performance results, along with the high standard errors relative to the percentage difference in C_p, associated with the retrofitted configuration measurements. In simulations, the same inflow conditions were used as shown in Figure 6.1 and thus the distinction is based from the effect of Gurney flaps. So the power comparison obtained from the simulations is used to estimate the increase in annual energy production. From cut in to cut out wind speed range, the annual energy production (AEP) estimate was made with the formulation shown below:

$$AEP = T \int_{U_{cut-in}}^{U_{cut-out}} P_{el}(U) f_{prob}(U) dU \tag{8.1}$$

In the above equation, T represents the time, for energy calculation, $T = 8766$ hours was used. The P_{el} represents the electric power production and $f_{prob}(U)$ represents the probability of the wind speed obtained from the Weibull distribution. dU represents the size of the wind speed bins, here used in steps of $1m/s$. To calculate the annual energy production, the Weibull parameters shown in Figure A.2 were used. This results in an increase in annual energy production of the retrofitted wind turbine by roughly $+0.2\%$. This corresponds to an increase in energy production by roughly $+50$ MWh.

This power increase comes at the expense of higher structural loads as will be explained below. The figures below show the blade flapwise bending moment increase in both mean and standard deviation statistics:

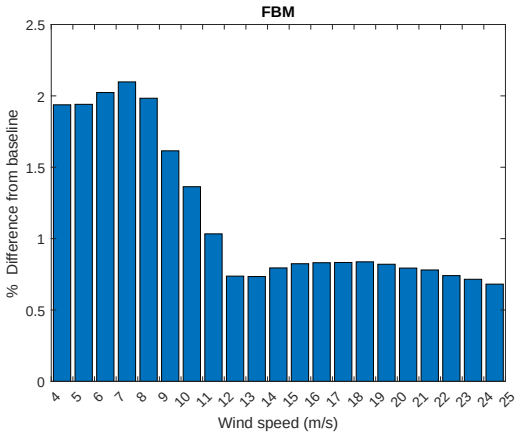

Figure 8.8: Blade flap-wise moment comparison

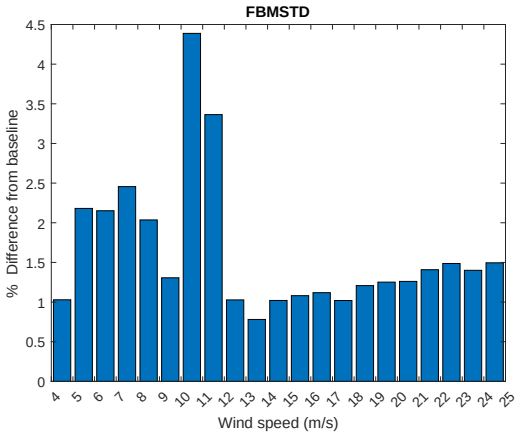

Figure 8.9: Blade flap-wise moment standard deviation comparison

In Figure 8.8 the consistent increase in blade flapwise bending moment is clear. Once again the same trend as expected from the angle of attack and lift distribution characteristics is seen. In Figure 8.9 a higher increase in the standard deviation of the flapwise bending moment is seen specially for the $10m/s - 12m/s$ wind speed range. This is because this region corresponds to the transition to the full load region of the wind turbine. So the variations are higher, and the underlying pitch variation was checked for. It was found to vary by 3% from the baseline in this wind speed range, which was maximum among all other wind speed bins. Furthermore, this was the wind speed range, where the angle of attack on the Gurney flap positions was such that the highest difference in lift coefficient was seen.

With this discussion on some of the important parameters indicating the structural effects of the tip Gurney flaps, it is clear that the structural loads will increase at all wind speeds for the retrofitted wind turbine. This was also seen in the field tests (Figure 7.15 and Figure 7.16), with the concern of limited data as mentioned previously. To assess the long term effect of this increase in structural loads a fatigue analysis was conducted. For fatigue analysis, typically there is a choice of two methods. First being using the $S - N$ or the Wöhler curve to determine the dimensionless quantity of damage done on basis of finding the number of cycles to failure at each load level. The standard $S - N$ equation is given by the following equation:

$$\log(S) = \log(S_u) - \frac{1}{m}\log(N) \tag{8.2}$$

In the above equation, S is the stress of the spectrum to be analysed, S_u as the ultimate stress value corresponding to the value at $N = 1$, where N represents the fatigue life as number of cycles and m is the Wöhler exponent. N is then found at each stress level and then the Palmgren-Miner rule is utilised as damage done, $D = \sum \frac{n_i}{N_i}$ where n_i comes from a method called Rainflow counting which provides the number of cycles for each stress level and i represents the i^{th} cycle of the stress spectrum to be analysed. The reader is referred to [171, 172, 173, 174] for background information. It should be noted that the equation above holds true for a zero mean stress level, that is, if the minimum and maximum stress are equal in a stress cycle. For the wind turbine blade the GFRP (glass fiber reinforced plastic/ polymers) material is used; and it is well known that for fiber reinforced materials the mean stress has a significant effect on the fatigue damage. So, the corresponding corrections have to be made to the above stated equation to accurately asses the cycles to failure. The values of the $S - N$ curve at different stress ratios (minimum applied stress to maximum applied stress ratio) have to be found out. Using literature values could be found for the stress ratio (R) of $R = -1$ and $R = 0.1$. Below a figure is provided to visualise the $S - N$ equation at a zero mean stress level to an empirical line derived from experimental data:

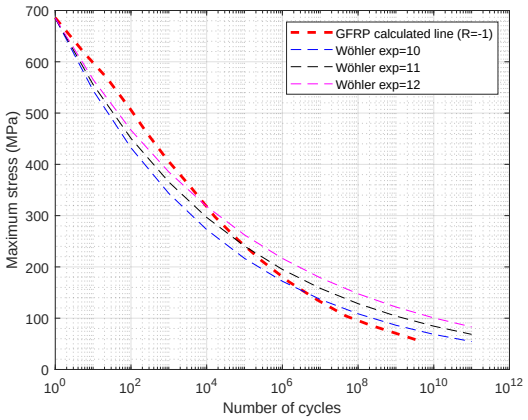

Figure 8.10: GFRP stress- cycles to failure curve (calculated line from [175])

In the above figure, the calculated line is presented from the empirical model formulated by authors of [175] based on the measurements from [174]. In Equation 8.2, S was calculated, S_u was used as the ultimate stress value corresponding to the value at $N = 1$. The tension values were used for the stresses.

The second method also utilises, m, the Wöhler exponent; but allows for comparison of a dimensional quantity which allows for a more physical understanding of the fatigue effects. The result of this method is typically called the damage equivalent load. In this study, a fatigue assessment based on the damage equivalent load formulation (corrected for mean stress) [176] was used with the input of the blade flapwise bending moment spectrum. Similar method can also be found in [173]. The following approach was used:

1. Use of flapwise bending moment spectrum (S) of $600s$ with $\Delta t = 0.005s$ with inflow conditions specified in Figure 6.1.
2. Use of MATLAB functions [177] for the following:
   (a) Converting this spectrum to peak and valley spectrum to be used for rainflow counting (function 'findTurningPts' made in line with [178]).
   (b) Rainflow counting to determine the range and mean of each load cycle and the corresponding count of cycles (function 'rainflow' made in line with [179]).
3. Assessing the damage equivalent spectrum (S_{eq}) with the following equation [176] at various S_u/S_{max} ratios and Wöhler exponents (m):

$$S_{r,eq} = \left(\frac{\sum_{i=1}^{n} \left(S_{r,i} \frac{S_u - |S_{m,eq}|}{S_u - |S_{m,i}|} \right)^m}{N_{eq}} \right)^{\frac{1}{m}} \tag{8.3}$$

With this discussion, the steps for the damage equivalent load assessment are stated. An example visualisation for the step $2a$ is provided in Figure 8.11. The output of step $2a$ was used in the Rainflow counting function. As stated earlier, the simulations were run for $660s$ at $\Delta T = 0.005s$ and the output of last $600s$ was used and the first $60s$ were assumed as transient. After step $2b$, the output of $S_{r,i}$ which is the range (difference of maximum and minimum value) of the load cycle at i^{th} cycle and $S_{m,i}$ which is the mean of the load cycle at i^{th} cycle was available. It can be shown that the ratio of two equivalent load ranges of two spectra is independent of N_{eq} and $S_{m,eq}$. So the authors of [176] state that an arbitrary choice for N_{eq} can be made. $N_{eq} = 10e6$ is used, this is also a commonly used value for damage equivalent analysis. This value is roughly the number of 10 minute periods in a 20 year span. They propose to use $S_{m,eq} = 0$, which is used in this analysis as well.

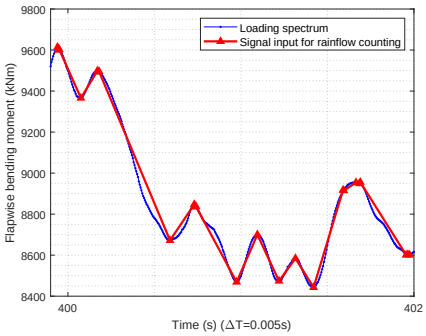

Figure 8.11: Example for peak and valley representation from the bending moment spectrum

The Wöhler exponent of $m = 10$ and $m = 12$ is analysed for. Finally, for S_u the authors propose to evaluate it at different $\frac{S_{max}}{S_u}$ ratios. When comparing the retrofitted and baseline case, it is necessary to use the same S_{max} values for both cases. So the value of S_{max} is used which corresponds to the maximum bending moment in the retrofitted case, different for each wind speed bin. With the necessary details provided on the approach used, the below figures show the results of the fatigue analysis based on damage equivalent load formulation:

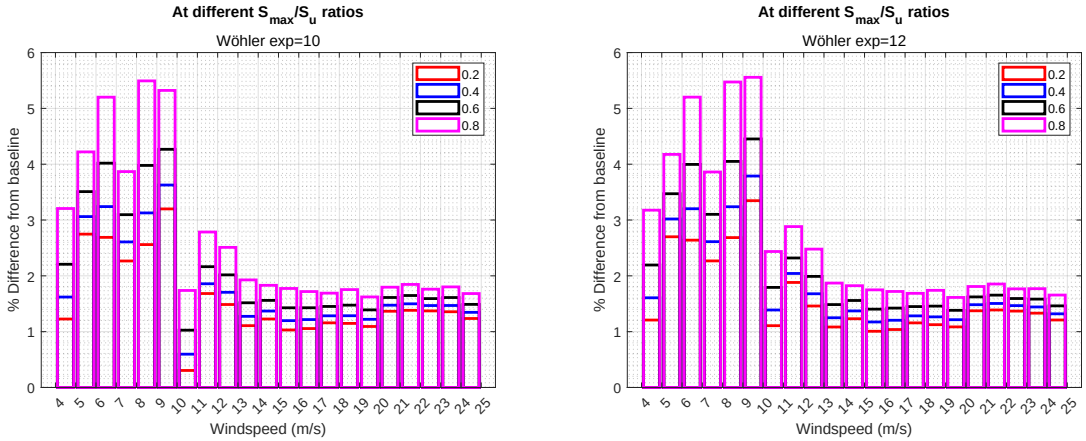

(a) Wöhler exponent 10

(b) Wöhler exponent 12

Figure 8.12: Damage equivalent load comparison

In Figure 8.12 it can be seen that the damage equivalent load for either Wöhler exponents do not differ significantly. Focusing on Figure 8.12a the trend of comparatively higher damage equivalent load upto $10m/s$ is evident. As statistically evident, the higher $\frac{S_{max}}{S_u}$ lead to higher damage equivalent loads for the Gurney flaps because the range gets closer to the maximum value utilised which was on basis of the maximum bending moment values in the retrofitted case. Up to $\approx 10m/s$ region is the partial load region and the angle of attacks were positive, as mentioned earlier by the ranges. This corresponds to regions on the lift coefficient curve where the lift curve slope of the airfoil with Gurney flap was more steep than the baseline. This leads to higher variations in lift for the retrofitted case. This was also seen in the other comparative figures provided above; as an exception to this, in Figure 8.9 there was a higher standard deviation seen for the $10 - 12m/s$, which was explained before in regards to the transition to full load region.

The wind speed Weibull distribution was incorporated to the damage equivalent flapwise bending moment differences discussed above. Like the AEP calculation, the Weibull parameters listed in Figure A.2 were used. Upon incorporating the Weibull distribution, the damage equivalent flapwise bending moment is found to increase by roughly +2% to +4%, all $\frac{S_{max}}{S_u}$ and Wöhler exponents inclusive. The former corresponds to $\frac{S_{max}}{S_u} = 0.2$ and $m = 10$ and the latter corresponds to $\frac{S_{max}}{S_u} = 0.8$ and $m = 12$.

Chapter 9

Conclusions and Recommendations

Contents

9.1 Conclusions

Aim: The aim of this thesis was to evaluate the use of segmented Gurney flaps on wind turbine blade tip to enhance the wind turbine wake recovery and assess the impact on the retrofitted wind turbine performance.

Hypothesis: The hypothesis behind the use of segmented Gurney flaps (in line with the ECN (now TNO Wind Energy) patent [2]) was to alter the lift distribution along the blade span (at tip); achieve a jagged lift and circulation distribution which causes additional stronger vortices shed from the edges of Gurney flaps to perturb the stable tip vortex (stability of which depends on the ambient turbulence and tip speed ratio of the wind turbine, among other factors). This use of segmented Gurney flaps was hypothesised to achieve a spatial disturbance to the tip vortex. Additionally, a temporal variation was hypothesised to be achieved from the inherent rotation of the wind turbine blade which alters the inflow conditions during the rotation as the large rotor is exposed to the wind speed and turbulence shear. Apart from these two effects, a higher drag from the Gurney flap was hypothesised to potentially increase turbulence in the wake which could contribute to the faster wake mixing.

Methodology: This study incorporated field tests and simulations on a 3.8 MW research wind turbine in the baseline configuration and retrofitted configuration with 4 Gurney flaps on each wind turbine blade tip. The field tests were conducted in a wind farm in Netherlands. The field tests were conduced for the wake analysis and retrofitted wind turbine performance analysis. The wake (and performance) analysis for the baseline case had 59 (and 144) days of data while for retrofitted, 23 days (see section 9.2 for explanation behind shorter testing for retrofitted configuration). For the wake analysis, the use of a Scanning LiDAR was made to scan the wind turbine wake up to $\approx 5.5D$ downstream at different downstream distances and altitudes. The scan time was ≈ 3 minutes and allowed for thorough wake visualisations. Data binning was done to quantify the effect on the wind turbine wake in various bins; the main basis of which was 10 minute averaged measurement data (at hub height) of wind direction, wind speed (shear) and turbulence intensity. Additionally, atmospheric stability conditions at the sites were assessed to ensure similar atmospheric stability regime for the comparison of wake. Gaussian process regression was used on the bin averaged data set to estimate the wind speed at missing points and enhance the wind field visualisation. Different methods to retrieve the wind speed from the LiDAR output of radial wind speed were tested. A simple method assuming the wind direction in the wake as the inflow wind direction at hub height was found to perform the best, in comparison to the commonly used non linear least square fit method and a slightly sophisticated Maximum A Posteriori method. For the performance analysis, 10 minute averaged measurement data was analysed within the undisturbed wind sector, different wind speed bins, a broad $0 - 15\%$ turbulence intensity range along with wind shear and yaw misalignment filters.

The simulations for the wind turbine wake analysis were conducted using free vortex wake modelling technique using NREL OLAF, with steady and uniform inflow at a wind speed bin corresponding to highest thrust of the 3.8 MW wind turbine rotor. The simulations for the wind turbine performance analysis were conducted using dynamic blade element momentum theory (DBEM, BEM for dynamic inflow conditions) on NREL OpenFAST from cut in to cut out wind speed using $IEC - NTM$ inflow conditions.

Wake analysis: The field tests' wake analysis provided a lot of insights into the wind turbine wake in varying atmospheric conditions. The problems associated with possibly foggy atmosphere and CNR filtering were looked into. Positive results were obtained for the effect of segmented Gurney flaps on the wake recovery. The results generally indicated a faster wake recovery for the retrofitted wind

turbine wake at all downstream distances, but with higher standard errors associated with the shorter test time. The results were most pronounced in the wind speed bin corresponding to the highest thrust of the wind turbine; during which the tip speed ratio suggests a stable helical wake vortex structure for the baseline wind turbine. Upon comparing the retrofitted wind turbine wake with baseline wind turbine wake at one TI bin higher, the faster wake recovery observations in retrofitted wind turbine wake suggest the increased turbulence in the wake causing the enhanced wake mixing upon addition of segmented Gurney flaps.

The wind speed bin corresponding to the highest thrust, which was $10m/s - 11m/s$ was tested in free vortex wake simulations. A faster (earlier by $\approx 2D$) tip vortex breakdown was seen in the results of the steady and uniform inflow free vortex wake simulations. A minimal increase in the integral of normal force (to chord) was noted, implying only 1% increase in overall rotor loading, which suggests that that the structural impacts on the retrofitted wind turbine are not very high.

Performance analysis: The dynamic blade element momentum theory simulations in $IEC - NTM$ inflow conditions revealed the operating angle of attack at the wind turbine blade tip. The angle of attack ranges from roughly 2 deg to 0 deg for $4 - 10m/s$ wind speed range and then decreasing to roughly -8 deg to -12 deg for $24 - 25m/s$ wind speed range. The range of angle of attack follows for the Gurney flap 1 to 4. The higher down wash associated with the Gurney flaps and the induced drag reduces the angle of attack in comparison to the baseline airfoil. This reduction ranges from roughly -0.5 deg to -1 deg and roughly -1.5 to -0.5 deg; in convention as mentioned above for the value of angle of attack. The resulting integral of normal force along the blade span has a maximum increase of only $\approx 2\%$ from the baseline wind turbine blade, indicating that the segmented Gurney flaps used do not significantly increase the overall blade loads.

The simulations' performance analysis indicates an increase in AEP by +0.2%, corresponding to +50 MWh. Field test measurements of retrofitted turbine data were associated with high standard errors leading to bias in results, thus, were not conclusively quantified. This increased power production comes at an expense of the structural loads. Consistent increase in blade flapwise and tower fore aft bending moment increase was seen. The standard deviation of flapwise bending moment was evaluated and a consistent increase from baseline was observed. This had implication on the fatigue, which was analysed using a damage equivalent load formulation corrected for mean stress. With the Weibull distribution of wind speed taken into account, the damage equivalent blade flapwise bending moment is expected to increase by roughly 2% to 4%, with peaks occurring in the partial load region of the wind turbine, associated with the operating angle of attack in this region.

9.2 Recommendations

In this section, the recommendations are listed on basis of two parameters: for future field tests, particularly wake and future research to further add to the results of this study are listed.

Future field tests: When conducting wake analysis for a single wind turbine in field tests, it is recommended to employ the scanning LiDAR settings such that in a 10 minute interval, 3 scans are made. The scan settings 2 of this study have made it possible to capture the wake at various downstream distances and altitudes with better resolution in comparison to other settings which were used during the measurement campaign. The results were presented only for the scan settings 2. This was in regards to the atmospheric stability regime and also because it helped reduce the standard error in the data set for better visualisation; and was set as the final scan for the field tests.

Secondly, based on the type of LiDAR used, it is recommended to employ different threshold for CNR depending on the distance and altitude in the scan. This check could be done during different whether conditions (for example, rain, snow, fog) or could be done for different back scatter coefficient (if available) ranges.

Next, when wanting to compare the wind turbine wakes of two different configurations of a wind turbine, the site conditions should be assessed beforehand to determine the prevalent atmospheric stability regime. Once that is clarified, a time span of 1.5 to 2 months should be considered for each configuration to achieve reasonable number of samples mainly for different wind speed (shear) and

turbulence intensity bins.

Lastly, it is recommended to do a thorough check on the wind turbine performance data on the wake data sets analysed. The analysis in this study revealed the necessity of the same, as outliers may be present after just the standard wind speed and turbulence intensity related filtering.

Future research: In this study, positive effects on wake recovery were seen for the retrofitted configuration. The impacts on the downstream wind turbine could not be assessed. The increased wind speed in the wake were evident, but with the limited number of scans, a conclusive quantification of this increase to the AEP increase for the downstream wind turbine was not possible. This may be made possible by longer period of field tests (so more scans in various bins) or by the means of simulations. Either blade resolved simulations or highly resolved (resolving each Gurney flap (and the neighboring region) with the required ϵ value, or using an optimal ϵ value, along with the necessary induction and wake region refinement) actuator line modelling large eddy simulations may be used in a future study. Both these approaches, require significant computational expense, the latter being less intensive than the former. The time step requirement for such a highly resolved actuator line study was found to be in the order of μs and this was deemed impractical for the scope of this study.

Such highly resolved actuator line large eddy simulations may be used to evaluate the effect of the changing (jagged) lift distribution near the blade tip, on the velocity profiles in the wake. In this thesis, the effect of changing lift distribution was validated by use of free vortex wake modelling, which indeed showed an earlier wake breakdown location. The Gurney flap geometry was not resolved and the results illustrated the effect of the different airfoil polar which was the one corresponding to the baseline airfoil with a Gurney flap. The impacts of this jagged lift distribution on the velocity profiles could not be tested in this study because of the artefacts of free vortex wake simulation results upon onset of the vortex breakdown. If the results of a highly resolved actuator line modelling large eddy simulations indicate increase in wake velocities further downstream (in accordance with the distance of downstream wind turbine), then an alternative to the use of segmented Gurney flaps would be possible. Future wind turbine blades can incorporate designs (with regards to practicality in terms of manufacturing) of the tip section such that the jagged lift and circulation distribution is achieved to achieve the vortices shed from these points along the blade span, as found in the free vortex wake simulations in this study and the underlying concept of the ECN patent.

The field test results (the lower deficits in all downstream distances for the retrofitted configuration) indicate an increased turbulence in the wake. The quantification of this seeming increase in turbulence in the wake upon addition of segmented Gurney flaps could be a potential future research topic. Consequently, it is necessary to assess the structural impact of the same on the downstream wind turbine. These can be achieved by LiDAR data for the turbulence in the wake, and measurement data for impact on the downstream wind turbine or blade resolved simulations. However, it is likely that blade resolved simulations to assess such parameters will not be practical.

A main limitation associated with the field tests was that the testing period of retrofitted configuration was shorter than the baseline configuration. This was because of increase of noise from the retrofitted wind turbine. Hence, as a precaution, the segmented Gurney flaps had to be removed earlier than desired. It was proposed to deploy a different design which involved geometrical changes to allow for a smoother design, but due to time restrictions it was not found to be feasible to incorporate this change during the field tests. So it could not be tested in this study, and an acoustic analysis by means of simulations was not considered in the scope of this study. Thus, to promulgate the further use of segmented Gurney flaps for wind turbine blades, a different design which helps reduce noise will be necessary. This need of a different design will specially be necessary for onshore wind farms and the prevailing noise regulations.

Bibliography

[1] Michael Sprague, Ganesh Vijayakumar, Shreyas Ananthan, M. Brazell, A. Sharma, and J. Sitaraman. *ExaWind: Exascale Predictive Wind Plant Flow Physics Modeling*. Tech. rep. Golden, CO, United States: National Renewable Energy Laboratory (NREL) etc., July 2021. URL: https://www.nrel.gov/news/program/2019/nrel-researchers-pursue-biggest-possible-wind-plant-model.html.

[2] Arne Van Garrel and Edwin Theodorus Gerardus Bot. *Rotor Blade For A Wind Turbine, And Wind Turbine Field*. July 2014. URL: https://worldwide.espacenet.com/patent/search/family/049261717/publication/EP3027894A1?q=pn%3DEP3027894A1.

[3] Tony Burton, Nick Jenkins, David Sharpe, and Ervin Bossanyi. "Wind Energy Handbook, Second Edition". In: *Wind Energy Handbook, Second Edition* (May 2011). DOI: 10.1002/9781119992714. URL: https://onlinelibrary.wiley.com/doi/book/10.1002/9781119992714.

[4] Manwell J. F., Mcgowan J. G., and Rogers A. L. *Wind Energy Explained: Theory, Design and Application*. Segunda. 2009. Chap. 2, pp. 23–87. ISBN: 978-0-470-01500-1. URL: https://www.wiley.com/en-us/Wind+Energy+Explained%3A+Theory%2C+Design+and+Application%2C+2nd+Edition-p-9780470015001.

[5] Charlotte Bay Hasager, Nicolai Gayle Nygaard, Patrick J.H. Volker, Ioanna Karagali, Søren Juhl Andersen, and Jake Badger. "Wind Farm Wake: The 2016 Horns Rev Photo Case". In: *Energies 2017, Vol. 10, Page 317* 10.3 (Mar. 2017), p. 317. ISSN: 1996-1073. DOI: 10.3390/EN10030317. URL: https://www.mdpi.com/1996-1073/10/3/317.

[6] Fernando Port´e-Agel, Yu Ting Wu, and Chang Hung Chen. "A Numerical Study of the Effects of Wind Direction on Turbine Wakes and Power Losses in a Large Wind Farm". In: *Energies 2013, Vol. 6, Pages 5297-5313* 6.10 (Oct. 2013), pp. 5297–5313. ISSN: 1996-1073. DOI: 10.3390/EN6105297. URL: https://www.mdpi.com/1996-1073/6/10/5297.

[7] Fernando Porté-Agel, Majid Bastankhah, and Sina Shamsoddin. "Wind-Turbine and Wind-Farm Flows: A Review". In: *Boundary-Layer Meteorology 2019 174:1* 174.1 (Sept. 2019), pp. 1–59. ISSN: 1573-1472. DOI: 10.1007/S10546-019-00473-0. URL: https://link.springer.com/article/10.1007/s10546-019-00473-0.

[8] L. J. Vermeer, J. N. Sørensen, and A. Crespo. "Wind turbine wake aerodynamics". In: *Progress in Aerospace Sciences* 39.6-7 (Aug. 2003), pp. 467–510. ISSN: 0376-0421. DOI: 10.1016/S0376-0421(03)00078-2.

[9] Lorenzo E M Lignarolo. "On the Turbulent Mixing in Horizontal Axis Wind Turbine Wakes". In: (2016). DOI: 10.4233/UUID:057FA33F-82A3-4139-BEB8-53F184CD1D57. URL: https://repository.tudelft.nl/islandora/object/uuid%3A057fa33f-82a3-4139-beb8-53f184cd1d57.

[10] J. N. Sørensen. "Instability of helical tip vortices in rotor wakes". In: *Journal of Fluid Mechanics* 682 (Sept. 2011), pp. 1–4. ISSN: 1469-7645. DOI: 10.1017/JFM.2011.277. URL: https://www.cambridge.org/core/journals/journal-of-fluid-mechanics/article/instability-of-helical-tip-vortices-in-rotor-wakes/227D37E3B9DA30FC9D423B50C16E373D.

[11] Ylva Odemark. "Wakes behind wind turbines-Studies on tip vortex evolution and stability". In: (2012).

[12] J. K. Lundquist and L. Bariteau. "Dissipation of Turbulence in the Wake of a Wind Turbine". In: *Boundary-Layer Meteorology* 154.2 (Feb. 2015), pp. 229–241. ISSN: 15731472. DOI: https://doi.org/10.1007/s10546-014-9978-3. URL: https://link.springer.com/article/10.1007/s10546-014-9978-3.

[13] Niels Troldborg. "Actuator Line Modeling of Wind Turbine Wake". PhD thesis. Lyngby: Technical University of Denmark, June 2009. ISBN: 978-87-89502-80-9. URL: https://backend.orbit.dtu.dk/ws/portalfiles/portal/5289074/Thesis.pdf.

[14] Ferhat Bingöl, Jakob Mann, and Gunner C. Larsen. "Light detection and ranging measurements of wake dynamics Part I: One-dimensional Scanning". In: *Wind Energy* 13.1 (2010), pp. 51–61. ISSN: 1095-4244. DOI: 10.1002/WE.352. URL: https://orbit.dtu.dk/en/publications/light-detection-and-ranging-measurements-of-wake-dynamics-part-i-.

[15] Davide Medici. *Experimental Studies of Wind Turbine Wakes-Power Optimisation and Meandering*. Tech. rep. Stockholm: Royal Institute of Technology, Dec. 2005. URL: https://www.diva-portal.org/smash/get/diva2:14563/FULLTEXT01.pdfPower.

[16] N Bodini, J K Lundquist, and A Kirincich. "Offshore Wind Turbines Will Encounter Very Low Atmospheric Turbulence". In: *Journal of Physics: Conference Series* 1452 (2023), p. 12023. DOI: 10.1088/1742-6596/1452/1/012023.

[17] Wolf Gerrit Fröh, Angus C.W. Creech, and A. Eoghan Maguire. "Turbulence characteristics in offshore wind farms from les simulations of Lillgrund wind farm". In: *Energy Procedia* 59 (2014), pp. 182–189. ISSN: 18766102. DOI: 10.1016/J.EGYPRO.2014.10.365.

[18] Luis A. Martínez-Tossas, Matthew J. Churchfield, Ali Emre Yilmaz, Hamid Sarlak, Perry L. Johnson, Jens N. Sørensen, Johan Meyers, and Charles Meneveau. "Comparison of four large-eddy simulation research codes and effects of model coefficient and inflow turbulence in actuator-line-based wind turbine modeling". In: *Journal of Renewable and Sustainable Energy* 10.3 (May 2018), p. 033301. ISSN: 19417012. DOI: 10.1063/1.5004710. URL: https://aip.scitation.org/doi/abs/10.1063/1.5004710.

[19] J Jonkman, S Butterfield, W Musial, and G Scott. *Definition of a 5-MW Reference Wind Turbine for Offshore System Development*. Tech. rep. 2009. URL: http://www.osti.gov/bridge.

[20] Guodan Dong, Zhaobin Li, Jianhua Qin, and Xiaolei Yang. "How far the wake of a wind farm can persist for?" In: *Theoretical and Applied Mechanics Letters* 12.1 (Jan. 2022), p. 100314. ISSN: 2095-0349. DOI: 10.1016/J.TAML.2021.100314.

[21] Johan Meyers and Charles Meneveau. "Optimal turbine spacing in fully developed wind farm boundary layers". In: *Wind Energy* 15.2 (Mar. 2012), pp. 305–317. ISSN: 1099-1824. DOI: 10.1002/WE.469. URL: https://onlinelibrary.wiley.com/doi/full/10.1002/we.469.

[22] J.G. Schepers. *Engineering models in wind energy aerodynamics: Development, implementation and analysis using dedicated aerodynamic measurements*. Tech. rep. Delft: Technische Universiteit Delft, Nov. 2012. DOI: 10.4233/UUID:92123C07-CC12-4945-973F-103BD744EC87. URL: https://repository.tudelft.nl/islandora/object/uuid%3A92123c07-cc12-4945-973f-103bd744ec87.

[23] F. González-Longatt, P. P. Wall, and V. Terzija. "Wake effect in wind farm performance: Steady-state and dynamic behavior". In: *Renewable Energy* 39.1 (Mar. 2012), pp. 329–338. ISSN: 0960-1481. DOI: 10.1016/J.RENENE.2011.08.053.

[24] P.J. Eecen and Edwin Bot. "Wind farm calculation and optimization with FarmFlow". In: Petten: ECN, 2012.

[25] Daniel R Houck. "Review of wake management techniques for wind turbines". In: *Wind Energy* 25.2 (Feb. 2022), pp. 195–220. ISSN: 1099-1824. DOI: 10.1002/WE.2668. URL: https://onlinelibrary.wiley.com/doi/full/10.1002/we.2668.

[26] Ryan Nash, Reza Nouri, and Ahmad Vasel-Be-Hagh. "Wind turbine wake control strategies: A review and concept proposal". In: *Energy Conversion and Management* 245 (Oct. 2021), p. 114581. ISSN: 0196-8904. DOI: 10.1016/J.ENCONMAN.2021.114581.

[27] Ali C. Kheirabadi and Ryozo Nagamune. "A quantitative review of wind farm control with the objective of wind farm power maximization". In: *Journal of Wind Engineering and Industrial Aerodynamics* 192 (Sept. 2019), pp. 45–73. ISSN: 0167-6105. DOI: 10.1016/J.JWEIA.2019.06.015.

[28] S. Boersma, B. M. Doekemeijer, P. M.O. Gebraad, P. A. Fleming, J. Annoni, A. K. Scholbrock, J. A. Frederik, and J. W. Van Wingerden. "A tutorial on control-oriented modeling and control of wind farms". In: *Proceedings of the American Control Conference* (June 2017), pp. 1–18. ISSN: 07431619. DOI: 10.23919/ACC.2017.7962923.

[29] S K Kanev, F J Savenije, and W P Engels. "Active wake control: An approach to optimize the lifetime operation of wind farms". In: *Wind Energy* 21.7 (2018), pp. 488–501. DOI: https://doi.org/10.1002/we.2173. URL: https://onlinelibrary.wiley.com/doi/abs/10.1002/we.2173.

[30] Evan Gaertner, Jennifer Rinker, Latha Sethuraman, Frederik Zahle, Benjamin Anderson, Garrett Barter, Nikhar Abbas, Fanzhong Meng, Pietro Bortolotti, Witold Skrzypinski, George Scott, Roland Feil, Henrik Bredmose, Katherine Dykes, Matt Shields, Christopher Allen, and Anthony Viselli. "Definition of the IEA Wind 15-Megawatt Offshore Reference Wind Turbine". In: (2020). URL: https://www.nrel.gov/docs/fy20osti/75698.pdf.

[31] Koen Boorsma. *Heat and Flux // Analysis of field measurements*. Tech. rep. Energieonderzoek Centrum Nederland (ECN), Nov. 2012. URL: https://publicaties.ecn.nl/PdfFetch.aspx?nr=ECN-E--12-048.

[32] Deepu Dilip and Fernando Porté-Agel. "Wind Turbine Wake Mitigation through Blade Pitch Offset". In: *Energies 2017, Vol. 10, Page 757* 10.6 (May 2017), p. 757. ISSN: 1996-1073. DOI: 10.3390/EN10060757. URL: https://www.mdpi.com/1996-1073/10/6/757.

[33] Paul A. Fleming, Pieter M.O. Gebraad, Sang Lee, Jan Willem van Wingerden, Kathryn Johnson, Matt Churchfield, John Michalakes, Philippe Spalart, and Patrick Moriarty. "Evaluating techniques for redirecting turbine wakes using SOWFA". In: *Renewable Energy* 70 (Oct. 2014), pp. 211–218. ISSN: 0960-1481. DOI: 10.1016/J.RENENE.2014.02.015.

[34] Jiangang Wang, Carlo L Bottasso, and Filippo Campagnolo. "Wake redirection: comparison of analytical, numerical and experimental models". In: *Journal of Physics: Conference Series* 753.3 (Sept. 2016), p. 032064. ISSN: 1742-6596. DOI: 10.1088/1742-6596/753/3/032064. URL: https://iopscience.iop.org/article/10.1088/1742-6596/753/3/032064.

[35] P. M.O. Gebraad, P. A. Fleming, and J. W. Van Wingerden. "Comparison of actuation methods for wake control in wind plants". In: *Proceedings of the American Control Conference* 2015-July (July 2015), pp. 1695–1701. ISSN: 07431619. DOI: 10.1109/ACC.2015.7170977.

[36] J. Bartl and L. Sætran. "Experimental testing of axial induction based control strategies for wake control and wind farm optimization". In: *Journal of Physics: Conference Series* 753.3 (Sept. 2016), p. 032035. ISSN: 1742-6596. DOI: 10.1088/1742-6596/753/3/032035. URL: https://iopscience.iop.org/article/10.1088/1742-6596/753/3/032035.

[37] Joeri A Frederik, Bart M Doekemeijer, Sebastiaan P Mulders, and Jan-Willem van Wingerden. "The helix approach: Using dynamic individual pitch control to enhance wake mixing in wind farms". In: *Wind Energy* 23.8 (2020), pp. 1739–1751. DOI: https://doi.org/10.1002/we.2513. URL: https://onlinelibrary.wiley.com/doi/abs/10.1002/we.2513.

[38] Carsten Hein Westergaard. *Method for improving large array wind park power performance through active wake manipulation reducing shadow effects*. Aug. 2012. URL: https://patents.google.com/patent/US9835138B2/en.

[39] Jay P. Goit and Johan Meyers. "Optimal control of energy extraction in wind-farm boundary layers". In: *Journal of Fluid Mechanics* 768 (Apr. 2015), pp. 5–50. ISSN: 0022-1120. DOI: 10.1017/jfm.2015.70. URL: https://www.cambridge.org/core/product/identifier/S0022112015000701/type/journal_article.

[40] Wim Munters and Johan Meyers. "Towards practical dynamic induction control of wind farms: Analysis of optimally controlled wind-farm boundary layers and sinusoidal induction control of first-row turbines". In: *Wind Energy Science* 3.1 (Jan. 2018), pp. 409–425. ISSN: 23667451. DOI: 10.5194/WES-3-409-2018.

[41] Joeri Frederik, Robin Weber, Stefano Cacciola, Filippo Campagnolo, Alessandro Croce, Carlo Bottasso, and Jan-Willem Van Wingerden. "Periodic dynamic induction control of wind farms: proving the potential in simulations and wind tunnel experiments". In: (). DOI: 10.5194/wes-2019-50. URL: https://doi.org/10.5194/wes-2019-50.

[42] C. Wang, F. Campagnolo, A. Sharma, and C. L. Bottasso. "Effects of dynamic induction control on power and loads, by LES-ALM simulations and wind tunnel experiments". In: *Journal of Physics: Conference Series* 1618.2 (Sept. 2020), p. 022036. ISSN: 1742-6596. DOI: 10.1088/1742-6596/1618/2/022036. URL: https://iopscience.iop.org/article/10.1088/1742-6596/1618/2/022036.

[43] Joseph Smagorinsky. "General circulation experiments with the primitive equations: I. The basic experiment". In: *Monthly weather review* 91.3 (1963), pp. 99–164. URL: https://journals.ametsoc.org/view/journals/mwre/91/3/1520-0493_1963_091_0099_gcewtp_2_3_co_2.xml?tab_body=fulltext-display.

[44] Jens Nørkær Sørensen and Wen Zhong Shen. "Numerical Modeling of Wind Turbine Wakes". In: *Journal of Fluids Engineering* 124.2 (May 2002), pp. 393–399. ISSN: 0098-2202. DOI: 10.1115/1.1471361. URL: https://doi.org/10.1115/1.1471361.

[45] Louis Huang. *Enhancing Wake Mixing in Wind Farms by Multi-Sine Signals in the Helix Approach*. Tech. rep. Delft: Delft University of Technology, July 2022. URL: https://repository.tudelft.nl/islandora/object/uuid%3A80a5ffcd-a32a-4a0f-bbae-b91659f168d6.

[46] Robert H. Liebeck. "On the Design of Subsonic Airfoils for High Lift". In: *Journal of Aircraft* (May 1976). ISSN: 00218669. DOI: 10.2514/3.58406. URL: arc.aiaa.org/doi/10.2514/3.58406.

[47] Jorg Alber, Rodrigo Soto-Valle, Marinos Manolesos, Sirko Bartholomay, Christian Navid Nayeri, Marvin Schönlau, Christian Menzel, Christian Oliver Paschereit, Joachim Twele, and Jens Fortmann. "Aerodynamic effects of Gurney flaps on the rotor blades of a research wind turbine". In: *Wind Energy Science* 5.4 (Nov. 2020), pp. 1645–1662. ISSN: 23667451. DOI: 10.5194/WES-5-1645-2020.

[48] X. Huang, S. M. Alavi Moghadam, P. S. Meysonnat, M. Meinke, and W. Schröder. "Numerical analysis of the effect of flaps on the tip vortex of a wind turbine blade". In: *International Journal of Heat and Fluid Flow* 77 (June 2019), pp. 336–351. ISSN: 0142-727X. DOI: 10.1016/J.IJHEATFLUIDFLOW.2019.05.004.

[49] Wenguang Zhang, Yuanyuan Wang, Yangzhi Shen, Yang Wang, Yue Xu, and Xinyu Zhang. "CFD studies of wake characteristics and power capture of wind turbines with trailing edge flaps". In: *IEEE Access* 8 (2020), pp. 7349–7361. ISSN: 21693536. DOI: 10.1109/ACCESS.2020.2964620.

[50] A. Gomez Gonzalez, P. B. Enevoldsen, B. Akay, T. K. Barlas, A. Fischer, and H. Aa Madsen. "Experimental and numerical validation of active flaps for wind turbine blades". In: *Journal of Physics: Conference Series* 1037.2 (June 2018), p. 022039. ISSN: 1742-6596. DOI: 10.1088/1742-6596/1037/2/022039. URL: https://iopscience.iop.org/article/10.1088/1742-6596/1037/2/022039.

[51] Anton Werner Hulskamp. "The Smart Rotor Concept on Wind Turbines - Actuators and Structures". PhD thesis. Delft: Technische Universiteit Delft, Nov. 2011. ISBN: 978-90-8891-341-9. URL: https://repository.tudelft.nl/islandora/object/uuid%3A1e34c0f4-1f84-4728-8665-e5a9b901b271.

[52] Thijs Gillebaart. "Towards Efficient Fluid-Structure-Control Interaction for Smart Rotors". PhD thesis. Delft: Delft University of Technology, May 2016. DOI: 10.4233/UUID:C078909A-A39C-47B5-8CA6-2CBC9E04486E. URL: https://repository.tudelft.nl/islandora/object/uuid%3Ac078909a-a39c-47b5-8ca6-2cbc9e04486e.

[53] Jan-Willem VAN Wingerden. "Control of Wind Turbines with 'Smart' Rotors: Proof of Concept & LPV Subspace Identification". PhD thesis. Delft: Technische Universiteit Delft, Nov. 2008. URL: https://repository.tudelft.nl/islandora/object/uuid%3A21573afa-f9b2-4cb2-96d3-3902328ebe9c.

[54] Markus Schatz and Bert Günther. *Computational Modeling of the Unsteady Wake behind Gurney-Flaps*. July 2004. URL: https://www.cfd.tu-berlin.de/research/flowcontrol/gurneys_en/.

[55] J. J. Wang, Y. C. Li, and K. S. Choi. "Gurney flap—Lift enhancement, mechanisms and applications". In: *Progress in Aerospace Sciences* 44.1 (Jan. 2008), pp. 22–47. ISSN: 0376-0421. DOI: 10.1016/J.PAEROSCI.2007.10.001. URL: https://www.sciencedirect.com/science/article/pii/S0376042107000784.

[56] Junwei Yang, Hua Yang, Weijun Zhu, Nailu Li, and Yiping Yuan. "Experimental Study on Aerodynamic Characteristics of a Gurney Flap on a Wind Turbine Airfoil under High Turbulent Flow Condition". In: *Applied Sciences 2020, Vol. 10, Page 7258* 10.20 (Oct. 2020), p. 7258. ISSN: 2076-3417. DOI: 10.3390/APP10207258. URL: https://www.mdpi.com/2076-3417/10/20/7258/htm.

[57] David Robert Michael Jeffrey. "An Investigation Into The Aerodynamics Of Gurney Flaps". PhD thesis. University Of Southampton, July 1998. URL: https://eprints.soton.ac.uk/463695/1/674555.pdf.

[58] A. Scarabino, J. Marañón Di Leo, J. S. Delnero, and F. Bacchi. "Drag coefficients and Strouhal numbers of a port crane boom girder section". In: *Journal of Wind Engineering and Industrial Aerodynamics* 93.6 (June 2005), pp. 451–460. ISSN: 0167-6105. DOI: 10.1016/J.JWEIA.2005.03.004.

[59] Peter Sachs. *Wind forces in engineering*. Pergamon Press, 1978, p. 400. ISBN: 9781483148359. URL: https://www.elsevier.com/books/wind-forces-in-engineering/sachs/978-0-08-021299-9.

[60] John D. Holmes. "Wind Loading of Structures: Third Edition". In: *Wind Loading of Structures: Third Edition* (Jan. 2018), pp. 1–682. DOI: 10.1201/B18029/WIND-LOADING-STRUCTURES-JOHN-HOLMES. URL: https://www.taylorfrancis.com/books/mono/10.1201/b18029/wind-loading-structures-john-holmes.

[61] K. Boorsma and J. G. Schepers. "Rotor experiments in controlled conditions continued: New Mexico". In: *Journal of Physics: Conference Series* 753.2 (Sept. 2016), p. 022004. ISSN: 1742-6596. DOI: 10.1088/1742-6596/753/2/022004. URL: https://iopscience.iop.org/article/10.1088/1742-6596/753/2/022004.

[62] J A C Kentfield. "Theoretically and Experimentally Obtained Performances of Gurney-Flap Equipped Wind Turbines". In: *Wind Engineering* 18.2 (1994), pp. 63–74. ISSN: 0309524X, 2048402X. URL: http://www.jstor.org/stable/43749530.

[63] Ye Zhang, Varun Ramdoss, Zohaib Saleem, Xiaofang Wang, Gerard Schepers, and Carlos Ferreira. "Effects of root Gurney flaps on the aerodynamic performance of a horizontal axis wind turbine". In: *Energy* 187 (Nov. 2019), p. 115955. ISSN: 0360-5442. DOI: 10.1016/J.ENERGY.2019.115955. URL: https://research.tudelft.nl/en/publications/effects-of-root-gurney-flaps-on-the-aerodynamic-performance-of-a-.

[64] Vestas. *Vestas aerodynamic upgrades*. 2015. URL: https://nozebra.ipapercms.dk/Vestas/Communication/Productbrochure/ProductImprovements/AerodynamicUpgrades/.

[65] Claude G Matalanis and John K Eaton. *Wake vortex alleviation using rapidly acuated segmented Gurney flaps*. Tech. rep. California: Flow Physics and Computation Division; Department of Mechanical Engineering; Stanford University, Jan. 2007. URL: https://web.stanford.edu/group/fpc/Publications/TF/Claude.pdf.

[66] Claude G Matalanis and John K Eaton. "Wake Vortex Control Using Static Segmented Gurney Flaps". In: *AIAA* 45.2 (Feb. 2006), pp. 321–328. DOI: 10.2514/1.25956. URL: https://arc.aiaa.org/doi/10.2514/1.25956.

[67] Juan Sebastián Delnero, Julio Marañón Di Leo, and Mariano García Saínz. "Experimental study of near and far wake generated by a gurney mini flap in turbulent flow". In: *34th Wind Energy Symposium* (2016). DOI: 10.2514/6.2016-0522. URL: https://arc.aiaa.org/doi/10.2514/6.2016-0522.

[68] D. Holst, A. B. Bach, C. N. Nayeri, C. O. Paschereit, and G. Pechlivanoglou. "Wake Analysis of a Finite Width Gurney Flap". In: *Journal of Engineering for Gas Turbines and Power* 138.6 (June 2016). ISSN: 15288919. DOI: 10.1115/1.4031709/374189.

[69] D. R. Troolin, E. K. Longmire, and W. T. Lai. "Time resolved PIV analysis of flow over a NACA 0015 airfoil with Gurney flap". In: *Experiments in Fluids* 41.2 (Aug. 2006), pp. 241–254. ISSN: 07234864. DOI: 10.1007/S00348-006-0143-8/FIGURES/17. URL: https://link.springer.com/article/10.1007/s00348-006-0143-8.

[70] Jeppe ; Johansen and Niels N Sørensen. "Aerodynamic investigation of winglets on wind turbine blades using CFD". In: (2006). URL: https://backend.orbit.dtu.dk/ws/portalfiles/portal/7703268/ris_r_1543.pdf.

[71] Franz Mühle, Jan Bartl, Thomas Hansen, Muyiwa Samuel Adaramola, and Lars Sætran. "An experimental study on the effects of winglets on the tip vortex interaction in the near wake of a model wind turbine". In: *Wind Energy* 23.5 (May 2020), pp. 1286–1300. ISSN: 10991824. DOI: 10.1002/WE.2486.

[72] Drew Gertz, David A. Johnson, and Nigel Swytink-Binnema. "Comparative Measurements of the Effect of a Winglet on a Wind Turbine". In: (2014), pp. 121–126. URL: https://www.researchgate.net/publication/312825472_Comparative_Measurements_of_the_Effect_of_a_Winglet_on_a_Wind_Turbine.

[73] Mac Gaunaa and Jeppe Johansen. "Determination of the Maximum Aerodynamic Efficiency of Wind Turbine Rotors with Winglets". In: *Journal of Physics: Conference Series* 75.1 (July 2007), p. 012006. ISSN: 1742-6596. DOI: 10.1088/1742-6596/75/1/012006. URL: https://iopscience.iop.org/article/10.1088/1742-6596/75/1/012006.

[74] David C. Maniaci and Mark D. Maughmer. "Winglet design for wind turbines using a free-wake vortex analysis method". In: *50th AIAA Aerospace Sciences Meeting Including the New Horizons Forum and Aerospace Exposition* (Jan. 2012). DOI: 10.2514/6.2012-1158. URL: https://www.researchgate.net/publication/268471962_Winglet_Design_for_Wind_Turbines_Using_a_Free-Wake_Vortex_Analysis_Method.

[75] Ozlem Ceyhan-Yilmaz (ECN) and Jordy H.N. van Kalken (LM Wind Power). *InnoTIP end report*. Tech. rep. ECN & LM Wind Power, Sept. 2017. URL: https://repository.tno.nl/islandora/object/uuid%3A49fede24-dce4-4329-abe2-e87aa082537d.

[76] Jason Jonkman, Mike Sprague, and et. al. *OpenFAST | Wind Research | NREL*. 2022. URL: https://www.nrel.gov/wind/nwtc/openfast.html.

[77] Matthew Churchfield, Sang Lee, and Patrick Moriarty. *SOWFA: Simulator fOr Wind Farm Applications*. Tech. rep. Wind Research | NREL | U.S. Department of Energy, Office of Energy Efficiency and Renewable Energy, operated by the Alliance for Sustainable Energy, LLC, May 2012. URL: https://www.nrel.gov/wind/nwtc/sowfa.html.

[78] H. G. Weller, G. Tabor, H. Jasak, and C. Fureby. "A tensorial approach to computational continuum mechanics using object-oriented techniques". In: *Computers in Physics* 12.6 (Dec. 1998), p. 620. ISSN: 0894-1866. DOI: 10.1063/1.168744. URL: https://aip.scitation.org/doi/abs/10.1063/1.168744.

[79] Kelsey Shaler, Emmanuel Branlard, and Andy Platt. *OLAF User's Guide and Theory Manual*. Tech. rep. National Renewable Energy Laboratory, June 2020. URL: https://www.nrel.gov/docs/fy20osti/75959.pdf.

[80] Roland Stull. *Practical Meteorology: An Algebra-based Survey of Atmospheric Science*. 1.02b. Vancouver: University of British Columbia, 2017. Chap. 2. ISBN: 978-0-88865-283-6. URL: https://www.eoas.ubc.ca/books/Practical_Meteorology/.

[81] Cristina L. Archer, Sina Mirzaeisefat, and Sang Lee. "Quantifying the sensitivity of wind farm performance to array layout options using large-eddy simulations". In: *Geophysical Research Letters* 40.18 (Sept. 2013), pp. 4963–4970. ISSN: 1944-8007. DOI: 10.1002/GRL.50911. URL: https://onlinelibrary.wiley.com/doi/full/10.1002/grl.50911.

[82] M J Churchfield, P J Moriarty, G Vijayakumar, J G Brasseur, Matthew J Churchfield, Ganesh Vijayakumar, James G Brasseur, and Patrick J Moriarty. "Wind energy-related atmospheric boundary layer large-eddy simulation using openfoam". In: (2010). URL: https://www.nrel.gov/docs/fy10osti/48905.pdf.

[83] Mahdi Abkar and Fernando Porté-Agel. "Influence of atmospheric stability on wind-turbine wakes: A large-eddy simulation study". In: *Physics of Fluids* 27.3 (Mar. 2015), p. 035104. ISSN: 1070-6631. DOI: 10.1063/1.4913695. URL: https://aip.scitation.org/doi/abs/10.1063/1.4913695.

[84] H. Glauert. "Airplane Propellers". In: *Aerodynamic Theory* (1935), pp. 169–360. URL: https://link.springer.com/chapter/10.1007/978-3-642-91487-4_3.

[85] Ziying Yu, Xing Zheng, and Qingwei Ma. "Study on Actuator Line Modeling of Two NREL 5-MW Wind Turbine Wakes". In: *Applied Sciences 2018, Vol. 8, Page 434* 8.3 (Mar. 2018), p. 434. ISSN: 2076-3417. DOI: 10.3390/APP8030434. URL: https://www.mdpi.com/2076-3417/8/3/434.

[86] Ludwig Prandtl and Albert Betz. "Vier Abhandlungen zur Hydrodynamik und Aerodynamik". In: (1927). ISSN: 1863-1088.

[87] H. Glauert. "The Elements of Aerofoil and Airscrew Theory". In: *The Elements of Aerofoil and Airscrew Theory* (June 1983). DOI: 10.1017/CBO9780511574481. URL: https://doi.org/10.1017/CBO9780511574481.

[88] Pankaj K. Jha, Matthew J. Churchfield, Patrick J. Moriarty, and Sven Schmitz. "Guidelines for volume force distributions within actuator line modeling of wind turbines on large-eddy simulation-type grids". In: *Journal of Solar Energy Engineering, Transactions of the ASME* 136.3 (Aug. 2014). ISSN: 01996231. DOI: 10.1115/1.4026252/379616. URL: https://asmedigitalcollection.asme.org/solarenergyengineering/article/136/3/031003/379616/Guidelines-for-Volume-Force-Distributions-Within.

[89] Luis A. Martínez, Stefano Leonardi, Matthew J. Churchfield, and Patrick J. Moriarty. "A Comparison of Actuator Disk and Actuator Line Wind Turbine Models and Best Practices for Their Use". In: *50th AIAA Aerospace Sciences Meeting Including the New Horizons Forum and Aerospace Exposition* (2012). DOI: 10.2514/6.2012-900.

[90] Michael Shives and Curran Crawford. "Mesh and load distribution requirements for actuator line CFD simulations". In: *Wind Energy* 16.8 (2013), pp. 1183–1196. ISSN: 10991824. DOI: 10.1002/WE.1546.

[91] L A Martínez-Tossas, M J Churchfield, and C Meneveau. "Optimal smoothing length scale for actuator line models of wind turbine blades based on Gaussian body force distribution". In: *Wind Energy* (2015), pp. 1–15. DOI: 10.1002/we. URL: https://onlinelibrary.wiley.com/doi/10.1002/we.2081.

[92] Mohsen Boojari, Esmail Mahmoodi, and Ali Khanjari. "Wake modelling via actuator-line method for exergy analysis in openFOAM". In: *International Journal of Green Energy* 16.11 (Sept. 2019), pp. 797–810. ISSN: 15435083. DOI: 10.1080/15435075.2019.1641101. URL: https://www.tandfonline.com/doi/abs/10.1080/15435075.2019.1641101.

[93] R. Courant, K. Friedrichs, and H. Lewy. "Über die partiellen Differenzengleichungen der mathematischen Physik". In: *Mathematische Annalen* 100.1 (Dec. 1928), pp. 32–74. ISSN: 00255831. DOI: 10.1007/BF01448839/METRICS. URL: https://link.springer.com/article/10.1007/BF01448839.

[94] Kaya Dağ and Jens Sørensen. "A new tip correction for actuator line computations". In: *Wind Energy* 23 (Feb. 2020). DOI: 10.1002/we.2419.

[95] Luis A. Martinez-Tossas and Charles Meneveau. "Filtered lifting line theory and application to the actuator line model". In: *Journal of Fluid Mechanics* 863 (Jan. 2019), pp. 269–292. ISSN: 0022-1120. DOI: 10.1017/JFM.2018.994.

[96] Alexander R. Meyer Forsting, Georg Raimund Pirrung, and Néstor Ramos-García. "A vortex-based tip/smearing correction for the actuator line". In: *Wind Energy Science* 4.2 (2019), pp. 369–383. ISSN: 23667451. DOI: 10.5194/WES-4-369-2019.

[97] Vitor Gabriel Kleine. "On stability of vortices and vorticity generated by actuator lines". PhD thesis. Stockholm, Sweden: KTH Royal Institute of Technology, 2022. ISBN: 978-91-8040-348-1.

[98] Luca GAJONI. "A modified actuator line model for the optimization of wind farm simulations". PhD thesis. Milan, Itay: Politecnico di Milano, 2021.

[99] J.A. Michelsen and Sørensen N.N. *EllipSys2D/3D - The Numerical Wind Tunnel*. 1992. URL: https://the-numerical-wind-tunnel.dtu.dk/ellipsys.

[100] Emmanuel Branlard. *Wind Turbine Aerodynamics and Vorticity-Based Methods*. Springer International Publishing, 2017. ISBN: 9783319551630. DOI: 10.1007/978-3-319-55164-7. URL: http://www.springer.com/gp/book/9783319551630.

[101] A Van Garrel. *Development of a wind turbine aerodynamics simulation module*. Tech. rep. Petten: Energy research Centre of the Netherlands (ECN), Aug. 2003. URL: http://www.ecn.nl/docs/library/report/2003/c03079.pdf.

[102] Sandeep Gupta and J Gordon Leishman. "Development of a Time-Accurate Viscous Lagrangian Vortex Wake Model for Wind Turbine Applications". In: (July 2006). URL: https://drum.lib.umd.edu/handle/1903/3783.

[103] J. Gordon Leishman, Mahendra J. Bhagwat, and Ashish Bagai. "Free-Vortex Filament Methods for the Analysis of Helicopter Rotor Wakes". In: *https://doi.org/10.2514/2.3022* 39.5 (May 2012), pp. 759–775. ISSN: 15333868. DOI: 10.2514/2.3022. URL: https://arc.aiaa.org/doi/10.2514/2.3022.

[104] Ashish Bagai and J. Gordon Leishman. "Flow visualization of compressible vortex structures using density gradient techniques". In: *ExFl* 15.6 (Oct. 1993), pp. 431–442. ISSN: 0723-4864. DOI: 10.1007/BF00191786. URL: https://ui.adsabs.harvard.edu/abs/1993ExFl...15..431B/abstract.

[105] Maria Ribera and Roberto Celi. "Helicopter Flight Dynamics Simulation with a Time-Accurate Free-Vortex Wake Model". In: (Apr. 2007). URL: https://drum.lib.umd.edu/handle/1903/6876.

[106] G. H. Vatistas, V. Kozel, and W. C. Mih. "A simpler model for concentrated vortices". In: *Experiments in Fluids* 11.1 (Apr. 1991), pp. 73–76. ISSN: 07234864. DOI: 10.1007/BF00198434/METRICS. URL: https://link.springer.com/article/10.1007/BF00198434.

[107] Shreyas Ananthan and J Leishman. "Role of Filament Strain in the Free-Vortex Modeling of Rotor Wakes". In: *Journal of The American Helicopter Society - J AMER HELICOPTER SOC* 49 (Apr. 2004). DOI: 10.4050/JAHS.49.176.

[108] TNO. *Innovation windturbine blade | TNO*. 2022. URL: https://www.tno.nl/en/sustainable/renewable-electricity/offshore-wind-farms/innovations-large-wind-turbines-future/new-research-blade-tip-improvements/.

[109] Sika Germany GmbH. *SikaBlock M940*. URL: http://www.sks-gmbh.com/jdownloads/Sika/SikaBlock%20M940.pdf.

[110] Matthew L. Aitken, Michael E. Rhodes, and Julie K. Lundquist. "Performance of a Wind-Profiling Lidar in the Region of Wind Turbine Rotor Disks". In: *Journal of Atmospheric and Oceanic Technology* 29.3 (Mar. 2012), pp. 347–355. ISSN: 0739-0572. DOI: 10.1175/JTECH-D-11-00033.1. URL: https://journals.ametsoc.org/view/journals/atot/29/3/jtech-d-11-00033_1.xml.

[111] E Simley and L Y Pao. "LIDAR Wind Speed Measurements of Evolving Wind Fields". In: (2012). URL: https://www.nrel.gov/docs/fy12osti/55516.pdf.

[112] S Davoust, A Jehu, M Bouillet, M Bardon, B Vercherin, Avent Lidar, Technology A Scholbrock, P Fleming, A Wright, Samuel Davoust, Alban Jehu, Michael Bouillet, Mathieu Bardon, Benoist Vercherin, Andrew Scholbrock, Paul Fleming, and Alan Wright. "Assessment and Optimization of Lidar Measurement Availability for Wind Turbine Control Preprint Assessment and Optimization of Lidar Measurement Availability for Wind Turbine Control". In: *NREL/CP-5000-61332*. 2014. URL: http://www.osti.gov/scitechonlineordering:http://www.ntis.gov/help/ordermethods.aspx.

[113] Alfredo Peña and Charlotte Bay Hasager. *Remote Sensing for Wind Energy*. Tech. rep. Risø National Laboratory for Sustainable Energy, Technical University of Denmark, 2011. URL: https://orbit.dtu.dk/en/publications/remote-sensing-for-wind-energy-2.

[114] N Cassamo, M Turrini, D A J Wouters, P A van der Werff, W A Castricum, and J W Wagenaar. *Application of Gaussian Processes to Dual-Doppler LiDAR scanning measurements for high frequency wind field reconstruction | TNO Publications*. Tech. rep. Petten, 2021. URL: https://repository.tno.nl//islandora/object/uuid:cdd003da-e6c8-48c1-acdc-04d5e4d4e1f8.

[115] Sven Erik Gryning and Rogier Floors. "Carrier-to-Noise-Threshold Filtering on Off-Shore Wind Lidar Measurements". In: *Sensors 2019, Vol. 19, Page 592* 19.3 (Jan. 2019), p. 592. ISSN: 1424-8220. DOI: 10.3390/S19030592. URL: https://www.mdpi.com/1424-8220/19/3/592/htm%20https://www.mdpi.com/1424-8220/19/3/592.

[116] Clym Stock-Williams, Paul Mazoyer, and Sébastien Combrexelle. "Wind field reconstruction from lidar measurements at high-frequency using machine learning". In: *Journal of Physics: Conference Series* 1102.1 (Oct. 2018), p. 012003. ISSN: 1742-6596. DOI: 10.1088/1742-6596/1102/1/012003. URL: https://iopscience.iop.org/article/10.1088/1742-6596/1102/1/012003.

[117] Inc. The Mathworks. *MATLAB:R2021a*. URL: https://nl.mathworks.com/products/matlab.html.

[118] C E Rasmussen and C K I Williams. "Gaussian Processes for Machine Learning". In: (). URL: www.GaussianProcess.org/gpml.

[119] Mathworks || MATLAB. *Kernel (Covariance) Function Options - MATLAB & Simulink - MathWorks Benelux*. 2022. URL: https://nl.mathworks.com/help/stats/kernel-covariance-function-options.html.

[120] Mathworks || MATLAB. *Fit a Gaussian process regression (GPR) model - MATLAB fitrgp - MathWorks*. 2022. URL: https://nl.mathworks.com/help/stats/fitrgp.html.

[121] Florian M. Heckmeier and Christian Breitsamter. "Aerodynamic probe calibration using gaussian process regression". In: *Measurement Science and Technology* 31.12 (Dec. 2020). ISSN: 13616501. DOI: 10.1088/1361-6501/ABA37D.

[122] Jie Wang. "An Intuitive Tutorial to Gaussian Processes Regression". In: (Apr. 2022). URL: https://github.com/jwangjie/.

[123] Lu Zhan, Stefano Letizia, and Giacomo Valerio Iungo. "LiDAR measurements for an onshore wind farm: Wake variability for different incoming wind speeds and atmospheric stability regimes". In: *Wind Energy* 23.3 (Mar. 2020), pp. 501–527. ISSN: 10991824. DOI: 10.1002/WE.2430.

[124] Nicola Bodini, Dino Zardi, and Julie K. Lundquist. "Three-dimensional structure of wind turbine wakes as measured by scanning lidar". In: *Atmospheric Measurement Techniques* 10.8 (Aug. 2017), pp. 2881–2896. ISSN: 18678548. DOI: 10.5194/AMT-10-2881-2017. URL: https://www.researchgate.net/publication/319110804_Three-dimensional_structure_of_wind_turbine_wakes_as_measured_by_scanning_lidar.

[125] Alfredo Peña, Jakob Mann, and Gunhild Rolighed Thorsen. *SpinnerLidar measurements for the CCAV52*. DTU Wind Energy, 2019. ISBN: 978-87-93549-45-6. URL: https://orbit.dtu.dk/en/publications/spinnerlidar-measurements-for-the-ccav52.

[126] P A van Dorp. *Quantifi cation of wind turbine wake characteristics from scanning LiDAR measurements*. Tech. rep. Petten: ECN, Aug. 2016.

[127] Lisa Yan and Chris Piech. *Maximum A Posteriori*. Tech. rep. Stanford University, Nov. 2019. URL: https://web.stanford.edu/class/archive/cs/cs109/cs109.1202/lectureNotes/LN23_map.pdf.

[128] Alex Tsun. *Statistical Estimation: Maximum A Posteriori Estimation*. Tech. rep. University of Washington Computer Science & Engineering, 2020. URL: https://courses.cs.washington.edu/courses/cse312/20su/files/student_drive/7.5.pdf.

[129] A.F. George Seber and C.J. Wild. *Nonlinear Regression*. Ed. by John Wiley & Sons. Auckland, New Zealand: Wiley, Sept. 2003, p. 792. ISBN: 978-0-471-47135-6. URL: https://www.wiley.com/en-mx/Nonlinear+Regression-p-9780471471356.

[130] William M. Bolstad. *Introduction to Bayesian Statistics*. 2nd ed. Published by John Wiley & Sons, Inc., Hoboken, New Jersey. Published simultaneously in Canada.: A John Wiley & Sons, Inc., Publication, 2007. ISBN: 978-0-470-141 15-1.

[131] Stefano Marelli and Bruno Sudret. "UQLab: A Framework for Uncertainty Quantification in Matlab". In: *Vulnerability, Uncertainty, and Risk*, pp. 2554–2563. DOI: 10.1061/9780784413609.257. URL: https://ascelibrary.org/doi/abs/10.1061/9780784413609.257.

[132] M C Holtslag, W A A M Bierbooms, and G J W Van Bussel. "Estimating atmospheric stability from observations and correcting wind shear models accordingly". In: *Journal of Physics: Conference Series* (2012). DOI: 10.1088/1742-6596/555/1/012052. URL: https://repository.tudelft.nl/islandora/object/uuid:ae654160-7984-4667-aeba-29ec46b4d181/datastream/OBJ.

[133] Geon Hwa Ryu, Dongjin Kim, Dae Young Kim, Young Gon Kim, Sung Jo Kwak, Man Soo Choi, Wonbae Jeon, Bum Suk Kim, and Chae Joo Moon. "Analysis of Vertical Wind Shear Effects on Offshore Wind Energy Prediction Accuracy Applying Rotor Equivalent Wind Speed and the Relationship with Atmospheric Stability". In: *Applied Sciences (Switzerland)* 12.14 (July 2022). ISSN: 20763417. DOI: 10.3390/APP12146949.

[134] Ameya Sathe, Sven Erik Gryning, and Alfredo Peña. "Comparison of the atmospheric stability and wind profiles at two wind farm sites over a long marine fetch in the North Sea". In: *Wind Energy* 14.6 (2011), pp. 767–780. ISSN: 10991824. DOI: 10.1002/WE.456.

[135] Sven Erik Gryning, Ekaterina Batchvarova, Burghard Brümmer, Hans Jørgensen, and Søren Larsen. "On the extension of the wind profile over homogeneous terrain beyond the surface boundary layer". In: *Boundary-Layer Meteorology* 124.2 (2007), pp. 251–268. ISSN: 00068314. DOI: 10.1007/S10546-007-9166-9. URL: https://www.researchgate.net/publication/227021596_On_the_extension_of_the_wind_profile_over_homogeneous_terrain_beyond_the_surface_layer.

[136] A S Monin and A M Obukhov. "Basic laws of turbulent mixing in the surface layer of the atmosphere". In: *Tr. Akad. Nauk SSSR Geophi* 24.151 (1954), pp. 163–187. URL: https://gibbs.science/efd/handouts/monin_obukhov_1954.pdf.

[137] M. De Franceschi and D. Zardi. "Evaluation of cut-off frequency and correction of filter-induced phase lag and attenuation in eddy covariance analysis of turbulence data". In: *Boundary-Layer Meteorology* 108.2 (Aug. 2003), pp. 289–303. ISSN: 00068314. DOI: 10.1023/A:1024157310388. URL: https://www.researchgate.net/publication/226051732_Evaluation_of_Cut-Off_Frequency_and_Correction_of_Filter-Induced_Phase_Lag_and_Attenuation_in_Eddy_Covariance_Analysis_of_Turbulence_Data.

[138] Karmen Babić, Zvjezdana Bencetić Klaić, and Željko Večenaj. "Determining a turbulence averaging time scale by Fourier analysis for the nocturnal boundary layer". In: 29 (), p. 2012. URL: http://geofizika-journal.gfz.hr/vol_29/No1/29_1_babic1_et_al.pdf.

[139] M. de Franceschi, D. Zardi, M. Tagliazucca, and F. Tampieri. "Analysis of second-order moments in surface layer turbulence in an Alpine valley". In: *Quarterly Journal of the Royal Meteorological Society* 135.644 (Oct. 2009), pp. 1750–1765. ISSN: 1477-870X. DOI: 10.1002/QJ.506. URL: https://onlinelibrary.wiley.com/doi/full/10.1002/qj.506.

[140] Bernhard Lange, Søren Larsen, Jørgen Højstrup, and Rebecca Barthelmie. "Importance of thermal effects and sea surface roughness for offshore wind resource assessment". In: *Journal of Wind Engineering & Industrial Aerodynamics* 92.11 (2004), pp. 959–988. ISSN: 0167-6105. DOI: 10.1016/J.JWEIA.2004.05.005. URL: https://orbit.dtu.dk/en/publications/importance-of-thermal-effects-and-sea-surface-roughness-for-offsh-2.

[141] April L. Hiscox. *Conceptual Boundary Layer Meteorology: The Air Near Here*. Elsevier, Jan. 2022, pp. 1–302. ISBN: 9780128170922. DOI: 10.1016/C2018-0-01664-3.

[142] A. A. Grachev and C. W. Fairall. "Dependence of the Monin–Obukhov Stability Parameter on the Bulk Richardson Number over the Ocean". In: *Journal of Applied Meteorology and Climatology* 36.4 (Apr. 1997), pp. 406–414. ISSN: 1520-0450. DOI: 10.1175/1520-0450(1997)036. URL: https://journals.ametsoc.org/view/journals/apme/36/4/1520-0450_1997_036_0406_dotmos_2.0.co_2.xml.

[143] Alfredo Peña and Sven Erik Gryning. "Charnock's Roughness Length Model and Non-dimensional Wind Profiles Over the Sea". In: *Boundary-Layer Meteorology* 128.2 (Aug. 2008), pp. 191–203. ISSN: 0006-8314. DOI: 10.1007/S10546-008-9285-Y. URL: https://orbit.dtu.dk/en/publications/charnocks-roughness-length-model-and-non-dimensional-wind-profile.

[144] Alfredo Peña, Sven Erik Gryning, and Charlotte B. Hasager. "Measurements and modelling of the wind speed profile in the marine atmospheric boundary layer". In: *Boundary-Layer Meteorology* 129.3 (2008), pp. 479–495. ISSN: 0006-8314. DOI: 10.1007/S10546-008-9323-9. URL: https://orbit.dtu.dk/en/publications/measurements-and-modelling-of-the-wind-speed-profile-in-the-marin.

[145] O.A. Alduchov and R.E. Eskridge. *Improved Magnus' form approximation of saturation vapor pressure*. Tech. rep. United States: Department of Commerce, Asheville, NC (United States), Nov. 1997. DOI: 10.2172/548871. URL: http://www.osti.gov/servlets/purl/548871-PjpxAP/webviewable/.

[146] Charles A. Doswell III and Erik N. Rasmussen. "The Effect of Neglecting the Virtual Temperature Correction on CAPE Calculations". In: *Weather and forecasting* (Dec. 1994), pp. 625–629. URL: https://journals.ametsoc.org/view/journals/wefo/9/4/1520-0434_1994_009_0625_teontv_2_0_co_2.xml.

[147] R J Barthelmie, M J Churchfield, P J Moriarty, J K Lundquist, G S Oxley, S Hahn, and S C Pryor. "The role of atmospheric stability/turbulence on wakes at the Egmond aan Zee offshore wind farm". In: *Journal of Physics: Conference Series* 625.1 (2015), p. 012002. ISSN: 1742-6596. DOI: 10.1088/1742-6596/625/1/012002. URL: https://dx.doi.org/10.1088/1742-6596/625/1/012002.

[148] D. Marten, C. O. Paschereit, X. Huang, M. Meinke, W. Schröder, J. Müller, and K. Oberleithner. "Predicting wind turbine wake breakdown using a free vortex wake code". In: *AIAA Journal* 58.11 (Sept. 2020), pp. 4672–4685. ISSN: 1533385X. DOI: 10.2514/1.J058308. URL: https://arc.aiaa.org/doi/10.2514/1.J058308.

[149] K Shaler, B Anderson, L A Martinez-Tossas, E Branlard, and N Johnson. "Comparison of free vortex wake and blade element momentum results against large-eddy simulation results for highly flexible turbines under challenging inflow conditions". In: *Wind Energy Science* 8.3 (2023), pp. 383–399. DOI: 10.5194/wes-8-383-2023. URL: https://wes.copernicus.org/articles/8/383/2023/.

[150] S. P. Mulders and J. W. Van Wingerden. "Delft Research Controller: an open-source and community-driven wind turbine baseline controller". In: *Journal of Physics: Conference Series* 1037.3 (June 2018), p. 032009. ISSN: 1742-6596. DOI: 10.1088/1742-6596/1037/3/032009. URL: https://iopscience.iop.org/article/10.1088/1742-6596/1037/3/032009.

[151] IEC. *Wind energy generation systems - Part 1: Design requirements (IEC 61400-1:2019,IDT)*. Tech. rep. International Electrotechnical Commission, 2019. URL: https://webstore.iec.ch/publication/26423.

[152] B J Jonkman and L Kilcher. *TurbSim User's Guide*. Tech. rep. Golden, Colorado: National Renewable Energy Laboratory, U.S. Department of Energy, 2012. URL: http://www.osti.gov/bridge.

[153] A. González, S. Gomez-Iradi, X. Munduate, A. González, S. Gomez-Iradi, and X. Munduate. "Validation of DYSTOOL for unsteady aerodynamic modeling of 2D airfoils". In: *JPhCS* 524.1 (2014), p. 012130. ISSN: 1742-6596. DOI: 10.1088/1742-6596/524/1/012130. URL: https://ui.adsabs.harvard.edu/abs/2014JPhCS.524a2130G/abstract.

[154] Rick Damiani and Greg Hayman. *The Unsteady Aerodynamics Module for FAST 8*. Tech. rep. Golden, CO: National Renewable Energy Laboratory, Nov. 2019. URL: https://www.nrel.gov/docs/fy20osti/66347.pdf.

[155] Martin Otto Laver Hansen. *Aerodynamics of Wind Turbines: second edition*. English. 2nd ed. Earthscan, 2008. ISBN: 978-1-84407-438-9.

[156] J G Holierhoek, J B de Vaal, A H van Zuijlen, and H Bijl. "Comparing different dynamic stall models". In: *Wind Energy* 16.1 (2013), pp. 139–158. DOI: https://doi.org/10.1002/we.548. URL: https://onlinelibrary.wiley.com/doi/abs/10.1002/we.548.

[157] H. Snel and J.G. Schepers. *Joint investigation of dynamic inflow effects and implementation of an engineering method*. Tech. rep. Petten: Energy research Centre of the Netherlands (ECN), 1995. URL: https://publications.ecn.nl/ECN-C--94-107.

[158] S Mancini, K Boorsma, G Schepers, and F Savenije. "A comparison of dynamic inflow models for the blade element momentum method". In: *Wind Energy Science* 8.2 (2023), pp. 193–210. DOI: 10.5194/wes-8-193-2023. URL: https://wes.copernicus.org/articles/8/193/2023/.

[159] J C Kaimal, J C Wyngaard, Y Izumi, and R Cote. "Spectral characteristics of surface-layer turbulence". In: 98 (May 1972), pp. 563–589. URL: https://apps.dtic.mil/sti/citations/AD0748543.

[160] Matthew L. Aitken, Robert M. Banta, Yelena L. Pichugina, and Julie K. Lundquist. "Quantifying Wind Turbine Wake Characteristics from Scanning Remote Sensor Data". In: *Journal of Atmospheric and Oceanic Technology* 31.4 (Apr. 2014), pp. 765–787. ISSN: 0739-0572. DOI: 10.1175/JTECH-D-13-00104.1. URL: https://journals.ametsoc.org/view/journals/atot/31/4/jtech-d-13-00104_1.xml.

[161] Julie K Lundquist. "Wind Shear and Wind Veer Effects on Wind Turbines". In: (2021). URL: https://link.springer.com/content/pdf/10.1007/978-3-030-05455-7_44-1.pdf.

[162] Mikael Magnusson and Ann-Sofi Smedman. "Influence of Atmospheric Stability on Wind Turbine Wakes". In: *Wind Engineering* 18.3 (1994), pp. 139–152. ISSN: 0309524X, 2048402X. URL: http://www.jstor.org/stable/43749538.

[163] M. Magnusson. "Near-wake behaviour of wind turbines". In: *J. Wind Eng. Ind. Aerodyn.* 80 (1999), pp. 147–167. URL: https://www.sciencedirect.com/science/article/pii/S0167610598001251.

[164] Robert W. Baker and Stel N. Walker. "Wake measurements behind a large horizontal axis wind turbine generator". In: *Solar Energy* 33.1 (Jan. 1984), pp. 5–12. ISSN: 0038-092X. DOI: 10.1016/0038-092X(84)90110-5.

[165] Mahdi Abkar and Fernando Porté-Agel. "The effect of atmospheric stability on wind-turbine wakes: A large-eddy simulation study". In: *Journal of Physics: Conference Series* 524.1 (2014), p. 012138. ISSN: 1742-6596. DOI: 10.1088/1742-6596/524/1/012138. URL: https://dx.doi.org/10.1088/1742-6596/524/1/012138.

[166] J. F. Ainslie. "Calculating the flowfield in the wake of wind turbines". In: *Journal of Wind Engineering and Industrial Aerodynamics* 27.1-3 (1988), pp. 213–224. ISSN: 01676105. DOI: 10.1016/0167-6105(88)90037-2.

[167] B. Sanderse. *Aerodynamics of wind turbine wakes Literature review*. Tech. rep. Petten: ECN, 2009. URL: https://www.semanticscholar.org/paper/Aerodynamics-of-wind-turbine-wakes-Literature-Sanderse/25d768ff87346b263be5a9523264de9ab00f606c.

[168] D. L. Elliott and J C Barnard. "Observations of wind turbine wakes and surface roughness effects on wind flow variability". In: *Solar Energy* 45 (1990), pp. 265–283. URL: https://www.sciencedirect.com/science/article/abs/pii/0038092X90900122.

[169] Sasan Sarmast, Reza Dadfar, Robert F. Mikkelsen, Philipp Schlatter, Stefan Ivanell, Jens N. Sørensen, and Dan S. Henningson. "Mutual inductance instability of the tip vortices behind a wind turbine". In: *Journal of Fluid Mechanics* 755 (Sept. 2014), pp. 705–731. ISSN: 0022-1120. DOI: 10.1017/jfm.2014.326. URL: https://www.cambridge.org/core/product/identifier/S0022112014003267/type/journal_article.

[170] Jens N Sørensen, Robert Mikkelsen, Sasan Sarmast, Stefan Ivanell, and Dan Henningson. "Determination of Wind Turbine Near-Wake Length Based on Stability Analysis". In: *Journal of Physics: Conference Series* 524.1 (June 2014), p. 12155. DOI: 10.1088/1742-6596/524/1/012155. URL: https://dx.doi.org/10.1088/1742-6596/524/1/012155.

[171] Herbert J. Sutherland. "On the Fatigue Analysis of Wind Turbines". In: (June 1999). DOI: 10.2172/9460. URL: https://www.osti.gov/biblio/9460.

[172] Herbert J Sutherland. *A Summary of the Fatigue Properties of Wind Turbine Materials*. Tech. rep. Sandia National Lab. (SNL-NM), Oct. 1990. URL: https://www.osti.gov/biblio/12694.

[173] K Thomsen. *The statistical variation of wind turbine fatigue loads*. English. Denmark. Forskningscenter Risoe. Risoe-R 1063(EN). 1998. ISBN: 87-550-2410-6. URL: https://orbit.dtu.dk/en/publications/the-statistical-variation-of-wind-turbine-fatigue-loads-3.

[174] P W Bach. *Fatigue properties of glass-and glass/carbon-polyester composites for wind turbines*. Tech. rep. Petten: Energy Research Centre of the Netherlands (ECN), Nov. 1992. URL: https://publicaties.ecn.nl/PdfFetch.aspx?nr=ECN-C--92-072.

[175] Jayantha A. Epaarachchi and Philip D. Clausen. "An empirical model for fatigue behavior prediction of glass fibre-reinforced plastic composites for various stress ratios and test frequencies". In: *Composites Part A: Applied Science and Manufacturing* 34.4 (Apr. 2003), pp. 313–326. ISSN: 1359-835X. DOI: 10.1016/S1359-835X(03)00052-6.

[176] H B Hendriks and B H Bulder. *Fatigue Equivalent Load Cycle Method*. Tech. rep. Petten: Energy Research Centre of the Netherlands (ECN), Oct. 1995. URL: https://publicaties.ecn.nl/PdfFetch.aspx?nr=ECN-C--95-074.

[177] MATLAB & Simulink - MathWorks Benelux. *Practical Introduction to Fatigue Analysis Using Rainflow Counting*. 2023. URL: https://nl.mathworks.com/help/signal/ug/practical-introduction-to-fatigue-analysis-using-rainflow-counting.html.

[178] I. Rychlik. "Simulation of load sequences from rainflow matrices: Markov method". In: *International Journal of Fatigue* 18.7 (Oct. 1996), pp. 429–438. ISSN: 0142-1123. DOI: 10.1016/0142-1123(96)80001-Z.

[179] ASTM. *Standard Practices for Cycle Counting in Fatigue Analysis*. URL: https://www.astm.org/e1049-85r17.html.

[180] Daniel Pereira. *Wind Rose*. 2023. URL: https://nl.mathworks.com/matlabcentral/fileexchange/47248-wind-rose.

[181] Victor Martínez-Cagigal. *Custom Colormap*. 2023. URL: https://nl.mathworks.com/matlabcentral/fileexchange/69470-custom-colormap.

Appendix A

Measurement Campaign

In this chapter, the site conditions as prevalent during the measurement campaign are shown with statistics of different parameters with 10 minute averaged data set, at hub height $110m$. The wind sector (undisturbed) is shown on the plots, the statistics are obtained by means of the ground- based profiling LiDAR. Additionally, a filter to ensure turbulence intensity (TI) is $\leq 50\%$ is applied.

A.1 Baseline Configuration

The figures below show the normalised values, normalised for probability. The total count of the 10 minute samples used to make these plots was 12592.

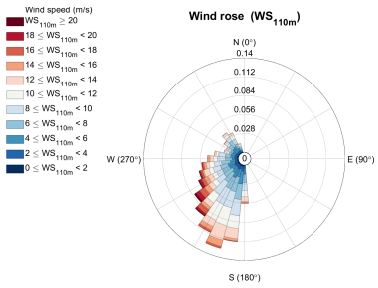

Figure A.1: Wind rose (All TI bins) (MATLAB Code from [180, 181])

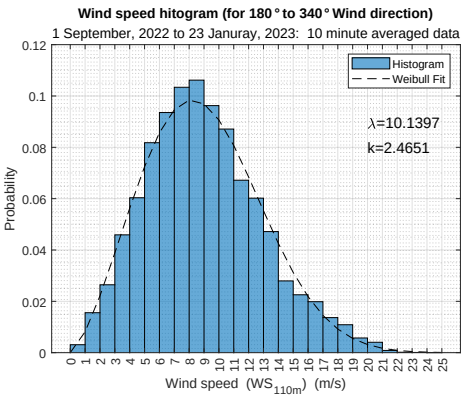

Figure A.2: Wind speed histogram (All TI bins)

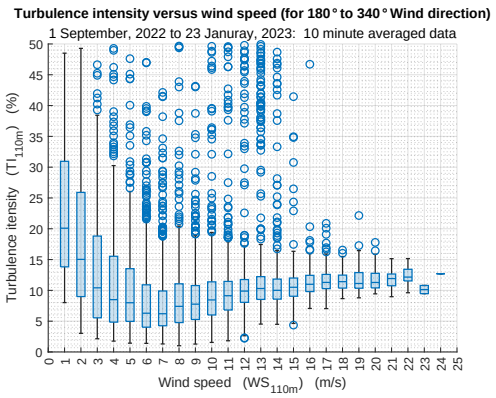

Figure A.3: Turbulence intensity compared against wind speed

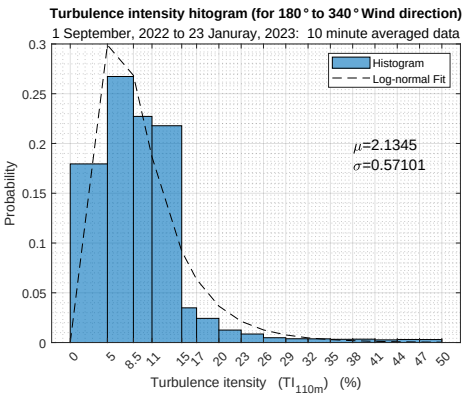

Figure A.4: Turbulence intensity histogram (All WS bins)

A.2 Retrofitted Configuration

The figures below show the normalised values, normalised for probability. The total count of the 10 minute samples used to make these plots was 1810.

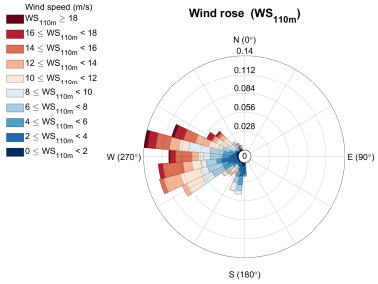

Figure A.5: Wind rose (All TI bins) (MATLAB Code from [180, 181])

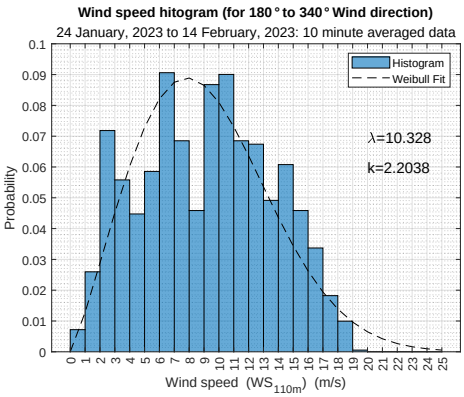

Figure A.6: Wind speed histogram (All TI bins)

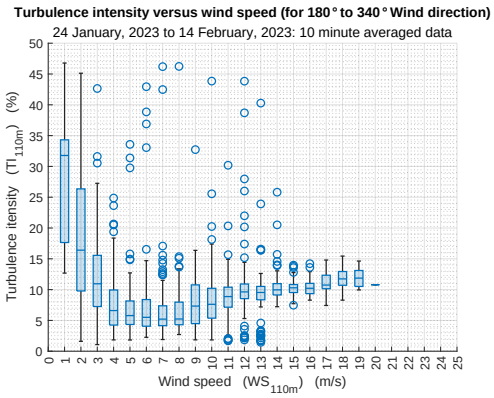

Figure A.7: Turbulence intensity compared against wind speed

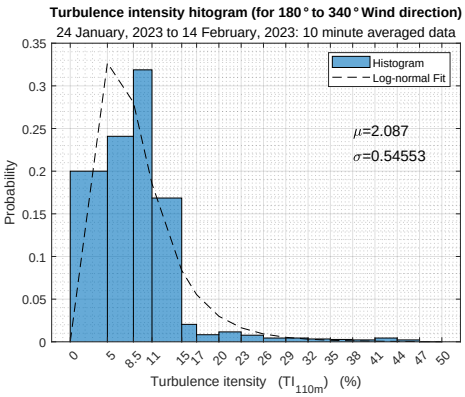

Figure A.8: Turbulence intensity histogram (All WS bins)

A.3 Wind Components during both configurations

The figures below show the normalised values, normalised for probability. The total count of the 10 minute samples used to make these plots was 7588.

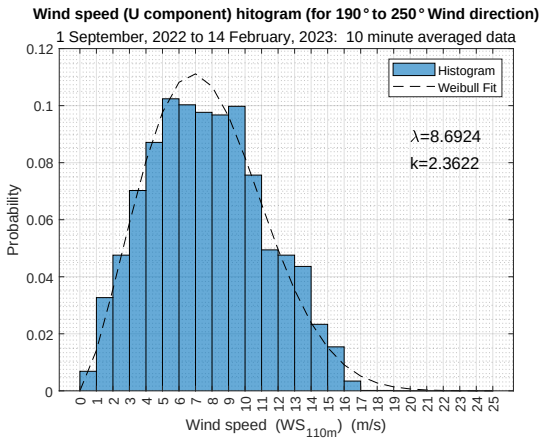

Figure A.9: U component (sign reversed)

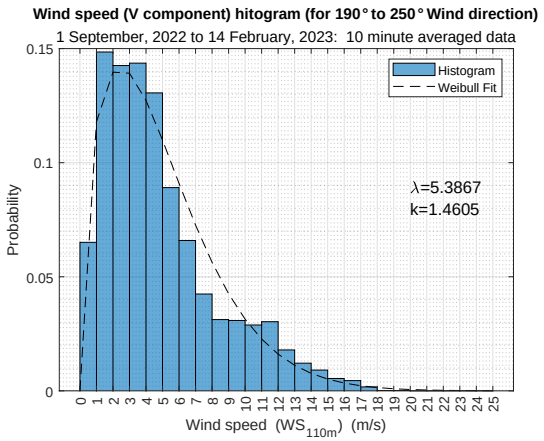

Figure A.10: V component (sign reversed)

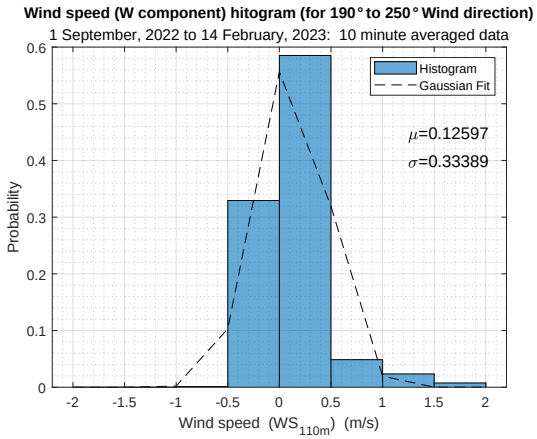

Figure A.11: W component

Appendix B

Results of Field tests

B.1 Fog check for $6m/s < U_{\infty,hub} < 7m/s$

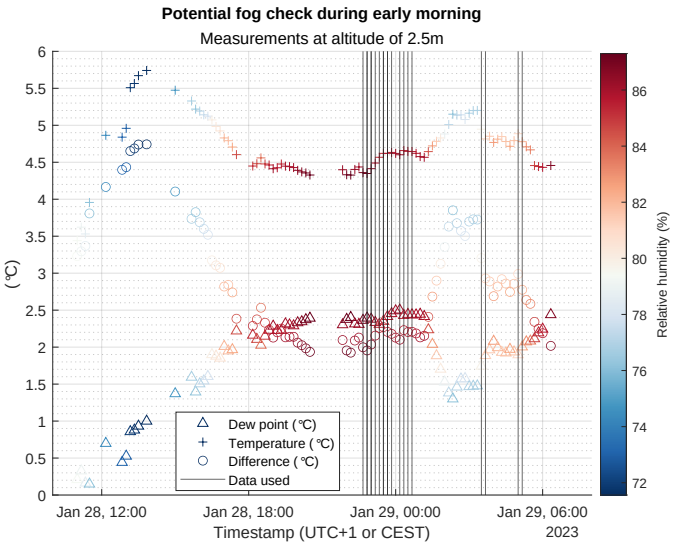

(a) Comparison of temperature and dew point

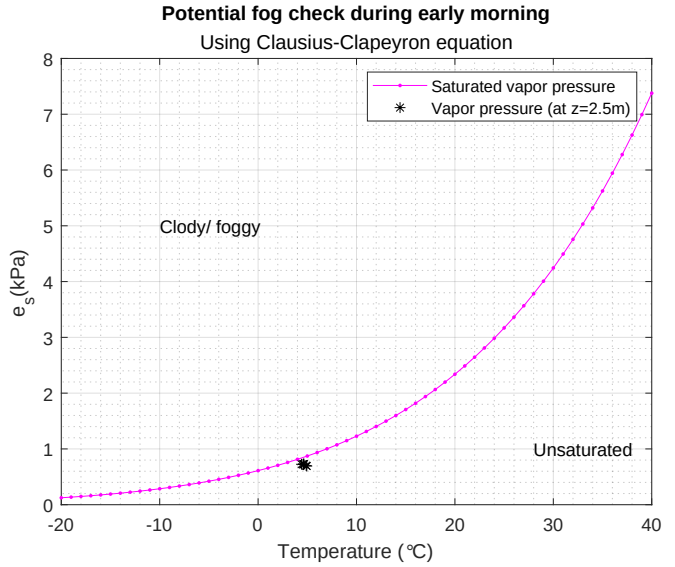

(b) Comparison of vapour pressure with saturated vapour pressure

Figure B.1: Potential fog check ($6m/s < U_{\infty,hub} < 7m/s$)

B.2 Wake analysis for $7m/s < U_{\infty,hub} < 8m/s$

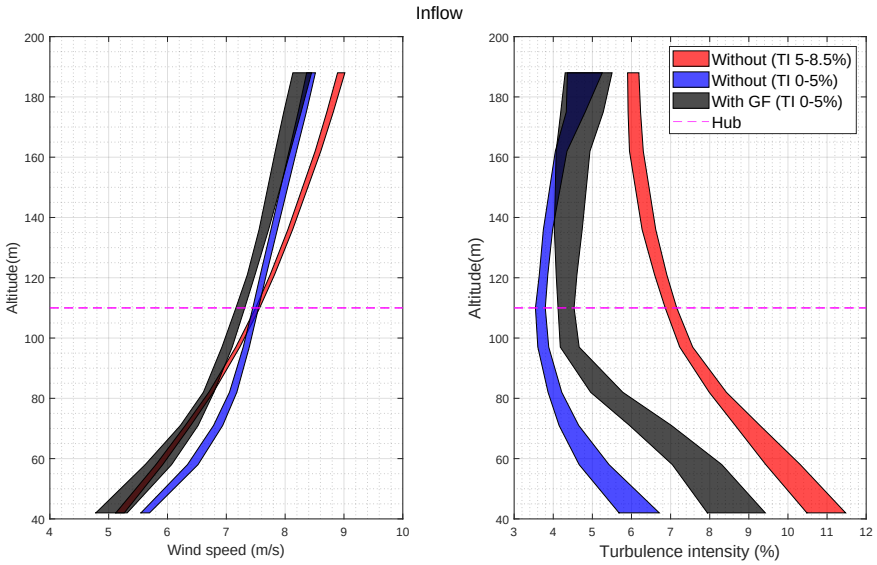

Figure B.2: Inflow profile ($7m/s < U_{\infty,hub} < 8m/s$)

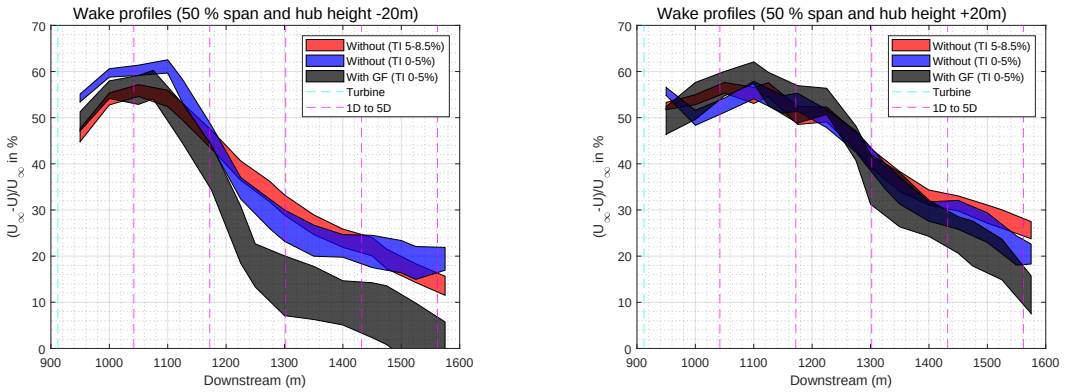

(a) Below hub height

(b) Above hub height

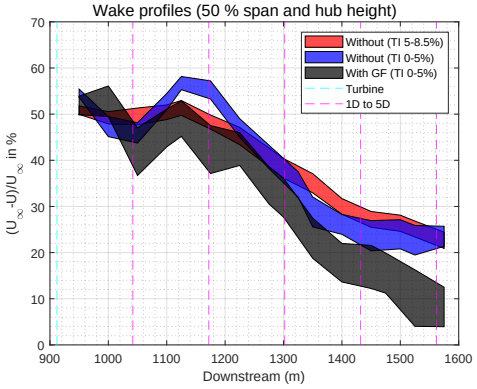

(c) hub height

Figure B.3: Axial wake profile (Normalised with U_∞ at the respective altitudes) ($7m/s < U_{\infty,hub} < 8m/s$)

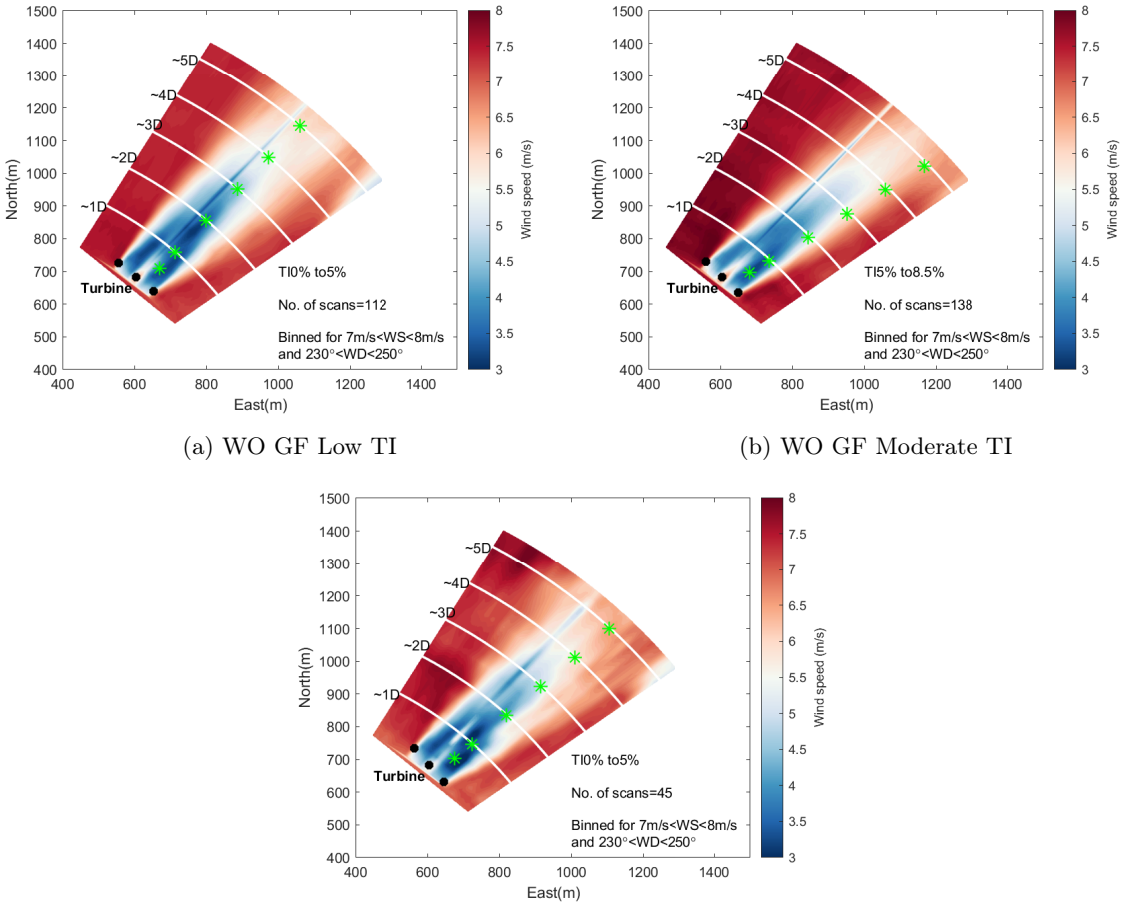

(a) WO GF Low TI

(b) WO GF Moderate TI

(c) W GF Low TI

Figure B.4: Wake visualisation ($7m/s < U_{\infty,hub} < 8m/s$)

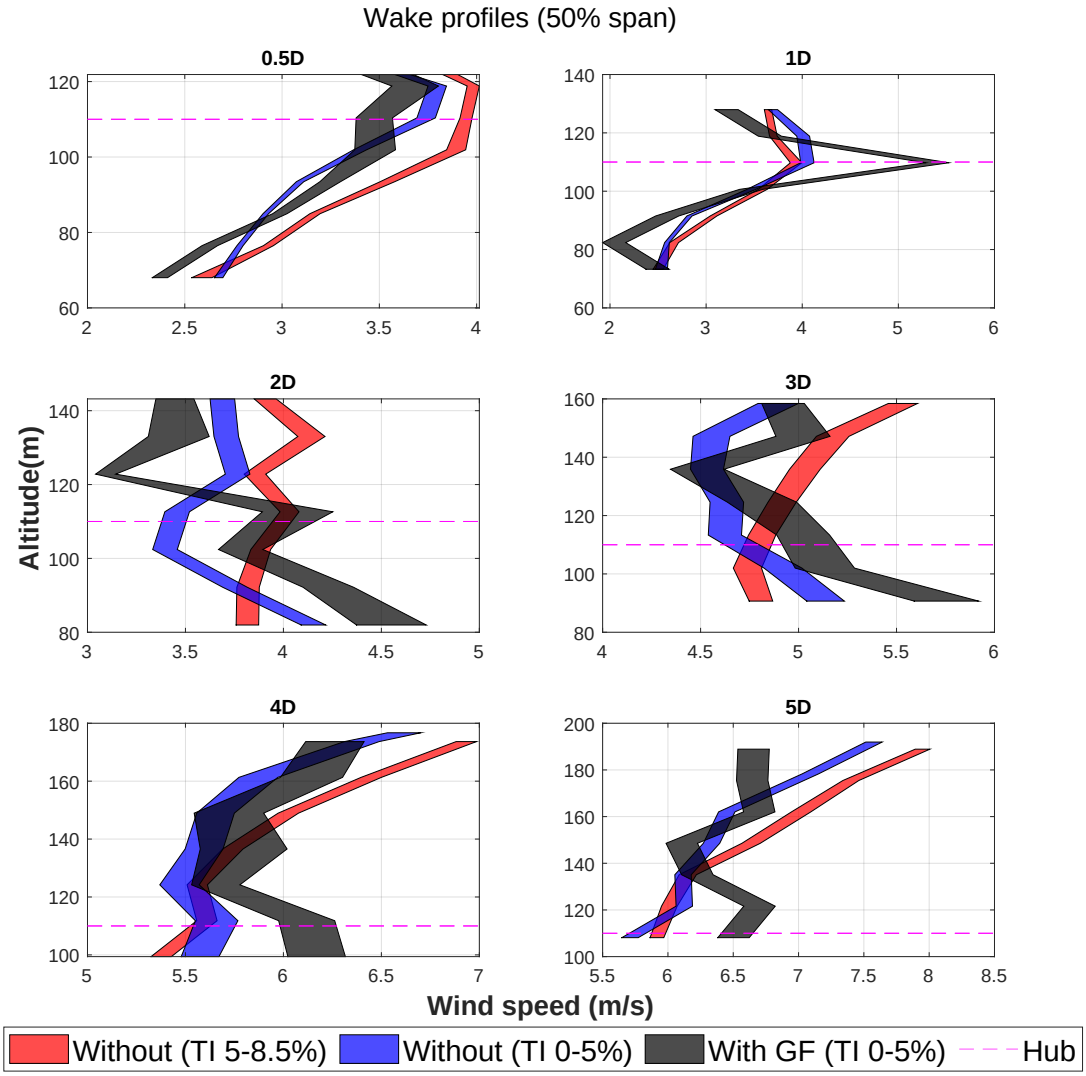

Figure B.5: Vertical profile ($7m/s < U_{\infty,hub} < 8m/s$)

B.3 Anomaly in $8m/s < U_{\infty,hub} < 9m/s$ bin

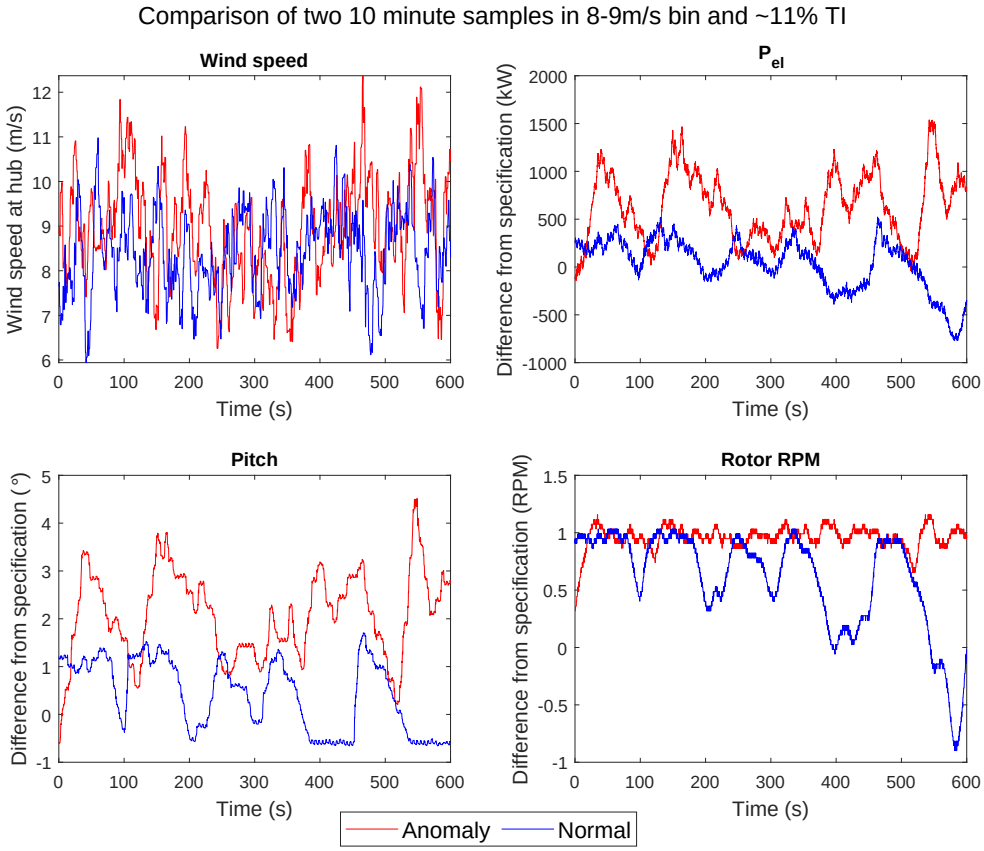

Figure B.6: Example for anomaly in data ($8m/s < U_{\infty,hub} < 9m/s$)

B.4 Wake analysis for $9m/s < U_{\infty,hub} < 10m/s$

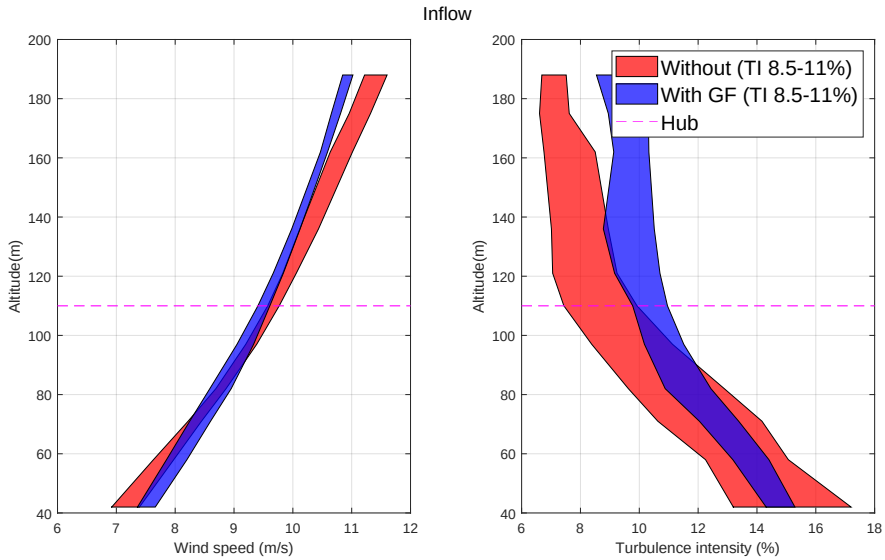

Figure B.7: Inflow profile ($9m/s < U_{\infty,hub} < 10m/s$)

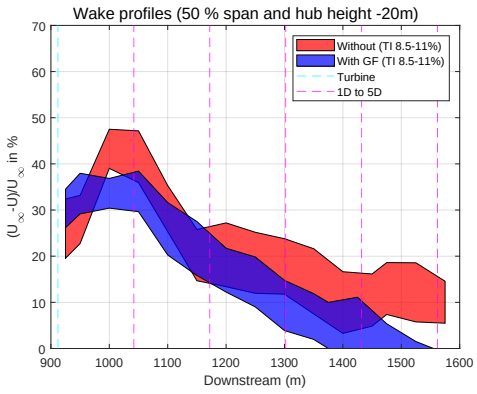

(a) Below hub height

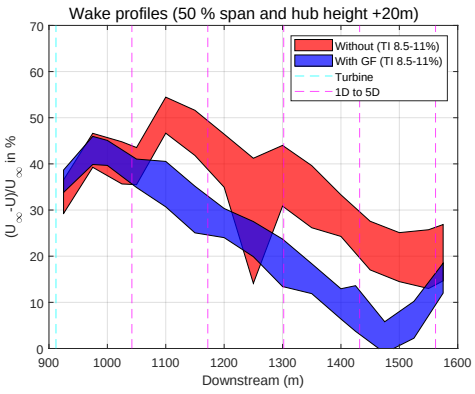

(b) Above hub height

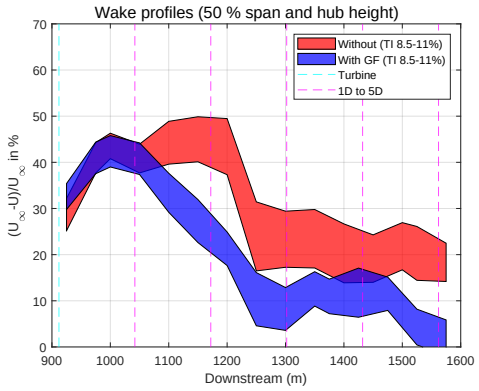

(c) Hub height

Figure B.8: Axial wake profile (Normalised with U_∞ at the respective altitudes) ($9m/s < U_{\infty,hub} < 10m/s$)

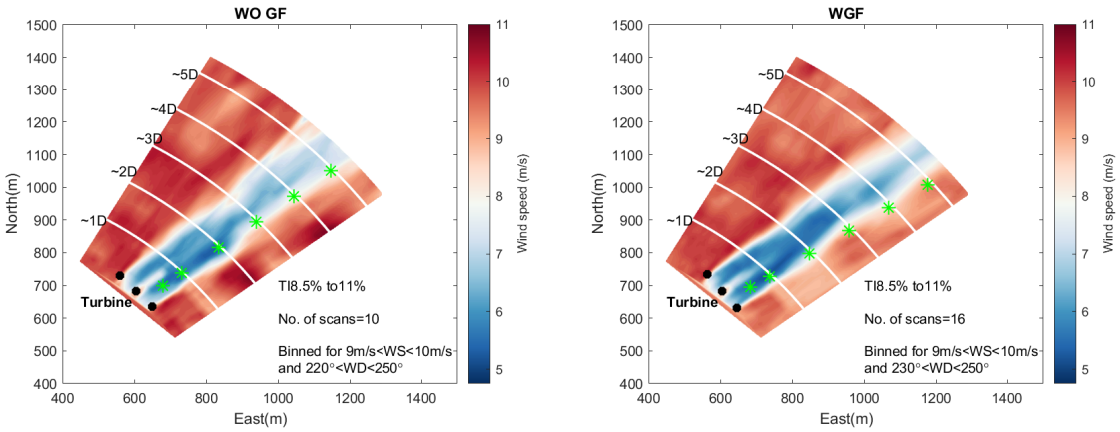

(a) WO GF High TI

(b) W GF High TI

Figure B.9: Wake visualisation ($9m/s < U_{\infty,hub} < 10m/s$)

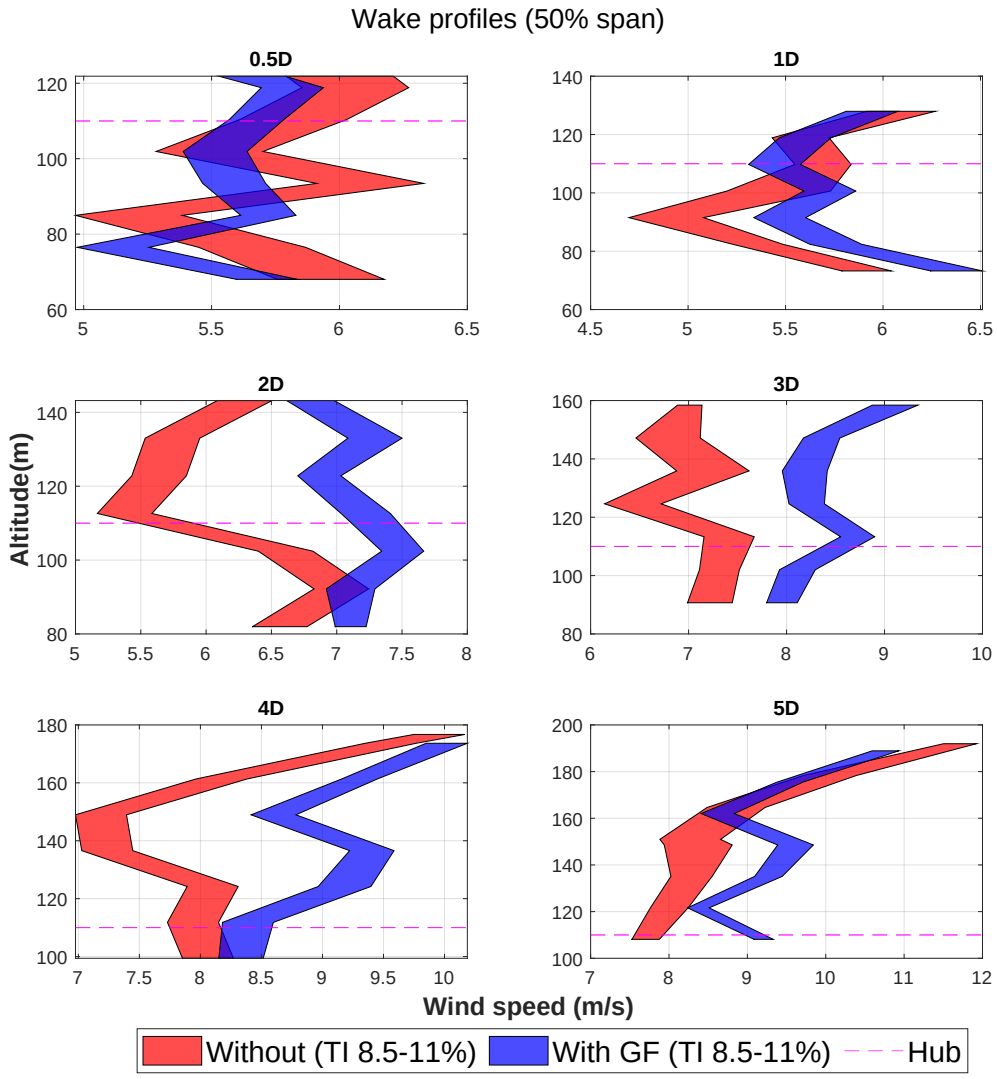

Figure B.10: Vertical profile